

**NPS ARCHIVE**  
**1969**  
**SPURGEON, D.**

PRELIMINARY DESIGN STUDIES FOR A  
HIGH FLUX MIT REACTOR

by

Dennis Ray Spurgeon



DUDLEY KNOX LIBRARY  
NAVAL POSTGRADUATE SCHOOL  
MONTEREY, CA 93943-5101

DUDLEY KNOX LIBRARY  
NAVAL POSTGRADUATE SCHOOL  
MONTEREY, CALIFORNIA 93943-5002

PRELIMINARY DESIGN STUDIES FOR A HIGH FLUX MIT REACTOR

by

Dennis Ray Spurgeon  
Lieutenant, United States Navy  
S.B., United States Naval Academy  
(1965)

Submitted in Partial Fulfillment of the  
Requirements for the Degrees of  
Master of Science in Nuclear Engineering  
and Nuclear Engineer at the  
Massachusetts Institute of Technology

June, 1969





## PRELIMINARY DESIGN STUDIES FOR A HIGH FLUX MIT REACTOR

by

Dennis R. Spurgeon

Submitted to the Department of Nuclear Engineering on May 15, 1969 in partial fulfillment of the requirement for the degrees of Master of Science in Nuclear Engineering and Nuclear Engineer.

### ABSTRACT

Design studies are performed and problem areas analyzed with respect to the redesign of the MIT Reactor in order to accommodate a compact core configuration.

Mechanical design studies are performed for a D<sub>2</sub>O moderated, cooled, and reflected compact core design. Designs are proposed for the core tank and reactor top shielding configuration, the core support mechanism, the control rod drive mechanisms, and the refueling mechanism.

The necessary composition and thickness of reactor top shielding are determined and shielding calculations performed for both a D<sub>2</sub>O cooled core and an H<sub>2</sub>O cooled core. Shielding above the D<sub>2</sub>O core consists of an 8 ft. column of D<sub>2</sub>O plus a shielding enclosure consisting of 6 in. of masonry, 1/2 in. of boral, and 1 ft. of lead, through which a maximum dose rate of 0.2 mrem/hr is calculated. Shielding above the H<sub>2</sub>O cooled core consists of 11 ft. of H<sub>2</sub>O topped by a 10 in. lead cover, through which a maximum dose rate of 0.9 mrem/hr is calculated.

The fluid flow and heat transfer problems associated with the design of a compact core configuration are analyzed and it is determined that the currently installed MITR process system is not capable of providing adequate heat removal from the compact core, if smooth flat plate fuel elements are utilized. An experimental investigation is undertaken to determine the effectiveness of using fins as a means of augmenting fuel plate heat transfer. Heat transfer from a smooth rectangular channel 2.5" x 0.090" x 25-1/2" is first investigated and experimental results confirm the validity of using the modified Colburn correlation,  $Nu_f = 0.023 Re_f^{0.8} Pr_f^{0.3}$ , to predict smooth



channel heat transfer values. Two finned channel test sections are investigated, one with fins cut into the channel transverse to the coolant flow direction, and a second with fins milled parallel to the coolant flow direction. In each case the fins are milled to be 20 mils high, 20 mils wide, and spread 40 mils apart. The transverse fins are found to augment heat transfer by a factor of 2.2, while a factor increase of 1.6 is obtained from the longitudinal fins. However, due to safety, pressure drop and cost considerations, longitudinally finned fuel plates are recommended for use in the High Flux MIT Reactor.

Supervisor: Dr. Theos J. Thompson

Title: Professor of Nuclear Engineering



## ACKNOWLEDGEMENTS

It is with sincere gratitude that I thank Professor Theos J. Thompson for his guidance, both technical and philosophical, during the course of this thesis. Of all the appreciative remarks which could be made concerning Dr. Thompson's guidance, the two qualities which I have appreciated most are that it was possible to be completely honest and forthright with Dr. Thompson, and that I was allowed to "chart my own course."

The heat transfer experimental work was aided immeasurably by the assistance and advice provided by Professor Arthur E. Bergles of the Department of Mechanical Engineering. The fabricational difficulty of the experimental test section cannot be overestimated, and were it not for the skill, ingenuity, and persistence of reactor machine shop personnel Francis Woodworth and Kenneth Butler, the test section could never have been constructed.

I would like to express by gratitude to the members of the MITR redesign team, and in particular to Ed Barnett for his many suggestions and bits of wisdom concerning mechanical design, to Dan Kennedy for his assistance with the computer code, to Bob Sanders and Andrews Addae for their many suggestions concerning heat transfer,



to Don Uhl for his assistance with the heat transfer experiment, and to Dave Gwinn for the benefit of his electrical know-how.

I would like to give special thanks to Miss Rita Falco, not only for her fine work in typing the final manuscript, but for her constant willingness to lend a helping hand in any way possible. Drawings for the final manuscript were reproduced by Lenny Andexler, whose assistance was certainly appreciated. My studies at MIT were financed by the United States Navy under the Junior Line Officer Advanced Scientific Education Program (Burke Program).

Lastly, I would like to thank my wife Carrol, whose understanding and encouragement have helped to lessen the burden.





## TABLE OF CONTENTS

	PAGE
Title Page	1
Abstract	2
Acknowledgements	4
Table of Contents	6
List of Figures	11
Introduction	14
1. <u>Description of Existing MITR Components</u>	19
1.1 General	19
1.2 Reactor Coolant Tank	19
1.3 Shielding Above the Core	22
1.3.1 Lower Annular Ring	22
1.3.2 Lower Shield Plug	23
1.3.3 Upper Annular Ring	23
1.3.4 Rotary Plug	23
1.4 Fuel Element Assembly	24
1.5 Control Rod Mechanisms	27
2. <u>Preliminary Mechanical Design Studies Done for Phase I</u>	31
2.1 General	31
2.2 Core Tank and Reactor Top Shielding Configuration	31
2.3 Core Support Mechanism	37
2.3.1 General	37
2.3.2 Grid Support	38
2.3.3 Sliding Bar Support	40
2.3.4 Safety Supports	45
2.4 Control Rod Drive Mechanisms	45
2.4.1 General	45
2.4.2 Absorber and Drive Mechanisms Outside Inner Core Tank	46



	PAGE
2.4.3 Drive Mechanism Through Annular Ring	47
2.4.4 Drive Mechanisms Above D <sub>2</sub> O Level	50
2.4.5 Drive Mechanisms for Inner Control Elements	56
2.5 Refueling Mechanism	58
2.5.1 General	58
2.5.2 Fuel Flipper Above Core Tank	59
2.5.3 Fuel Flipper Away from Core Tank Top	62
2.6 Underwater Periscope	64
3. <u>Shielding Calculations</u>	67
3.1 General	67
3.2 Computational Methods	70
3.2.1 General	70
3.2.2 Gamma Ray Attenuation	71
3.2.3 Neutron Attenuation	76
3.3 Shielding Calculations, Normal Operation (Phase I)	77
3.3.1 Fission Gamma Rays	77
3.3.2 Material Activation	84
3.3.2.1 General	84
3.3.2.2 Al <sup>27</sup> (n,γ) Al <sup>28</sup>	85
3.3.2.3 O <sup>16</sup> (n,p) N <sup>16</sup>	91
3.3.2.4 H <sup>2</sup> (n,γ) H <sup>3</sup>	94
3.3.3 Fission Product Decay	98
3.3.4 Neutron Attenuation	98
3.3.4.1 Fast Fission Neutrons	98
3.3.4.2 Thermal Neutrons	101
3.3.5 Photodisintegration of Deuterium	102
3.4 Shielding Calculations, Reactor Shutdown (Phase I)	107
3.4.1 General	107



3.4.2	Reactor Top Shield Plug Removed	107
3.4.3	Coolant Lost From Necked Tank	111
3.5	Dose Rate Through Concrete Shielding (Phase I)	112
3.6	Shielding Calculations Summary (Phase I)	116
3.6.1	Dose Through Shielding Directly Above the Core	116
3.6.2	Dose Through Reactor Top Concrete	117
3.6.3	Shielding Conclusions	117
3.7	Shielding Calculations, Normal Operation (Phase II)	117
3.7.1	General	117
3.7.2	Fission Gamma Rays	118
3.7.3	Material Activation	118
3.7.3.1	$Al^{27} (n, \gamma) Al^{28}$	118
3.7.3.2	$H^1 (n, \gamma) H^2$	119
3.7.3.3	$O^{16} (n, p) N^{16}$	121
3.7.4	Neutrons	121
3.8	Shielding Calculations, Reactor Shutdown (Phase II)	122
3.9	Shielding Calculations Summary (Phase II)	123
3.9.1	Dose Through Reactor Top Shield Plug	123
3.9.2	Dose Through Reactor Top Concrete	124
3.9.3	Shielding Conclusions	124
4.	<u>Heat Transfer, Preliminary Calculations</u>	125
4.1	General	125
4.2	Distribution of Reactor Heat Load	127
4.3	Hot Channel Factors	130
4.4	Power Distribution in the Core	137
4.5	Wall Temperature Along Hottest Channel	144
4.5.1	General	144
4.5.2	Formulation of Applicable Equation	145
4.5.3	Heat Transfer Coefficient	147





4.5.4	Limiting Parameters	152
4.5.4.1	Reactor Outlet Temperatures	152
4.5.4.2	Maximum Allowable Wall Temperature	152
4.5.4.3	Coolant Flow Rate	153
4.5.5	Calculations	153
4.5.6	Revised Data	161
4.6	Phase I vs Phase II	162
5.	<u>Augmentation of Fuel Plate Heat Removal</u>	163
5.1	General	163
5.2	Methods of Increasing the Product "hA"	163
5.2.1	Decreased Fuel Plate Spacing	163
5.2.2	Increased Mass Flow Rate	164
5.2.3	Modifications to Fuel Plates	166
5.3	Literature Search	167
5.3.1	General	167
5.3.2	Brouillette, Mifflin, and Myers	167
5.3.3	Nunner	170
5.3.4	Kolar	172
5.3.5	Lancet	173
5.3.6	Conclusions	173
5.4	Experimental Program	176
5.4.1	General	176
5.4.2	Coolant Channels	176
5.4.3	Description of Apparatus	181
5.4.3.1	Hydraulic System	181
5.4.3.2	Power Supply	184
5.4.3.3	Instrumentation	184
5.4.3.4	Test Section	185
5.4.4	Operating Procedure	193



	PAGE
5.4.5 Assumptions for Data Analysis	194
5.4.6 Experimental Results	196
5.4.7 Analysis of Results	206
5.4.8 Further Investigations	209
6. Conclusions	214
References	217
Appendix A: Heat Transfer Experimental Data	220



## LIST OF FIGURES

FIGURE		PAGE
1.2.1	Vertical Section of Reactor	20
1.2.2	Reactor Core Tank Support	21
1.4.1	Fuel Element Assembly	25
1.4.2	Horizontal Section	26
1.5.1	Modified Shim-Safety Rod Assembly	28
1.5.2	Mechanical Arrangement of Control Mechanisms	30
2.2.1	Double Rotating Shield Plug	33
2.3.2.1	Grid Support	39
2.3.3.1	Sliding Bar Support	41
2.3.3.2	Sliding Bar Support - Upper Adapter	42
2.3.3.3	Sliding Bar Support - Bars Withdrawn	44
2.4.3.1	L-Shaped Drive Mechanism	48
2.4.4.1	Cable Withdrawal Mechanism	51
2.4.4.2	Withdrawal Mechanisms Above Shielding	53
2.4.4.3	Magnetic Clutch Withdrawal Mechanism	55
2.4.5.1	Inner Control Element Drive Mechanism	57
2.5.2.1	Fuel Flipper Mechanism	60
2.5.3.1	Fuel Flipper Mechanism - Alternate Approach	63
3.1.1	Reactor Top Shielding Enclosure	68
3.2.2.1	Buildup Factors for Water	73
3.2.2.2	Buildup Factors for Iron	74
3.2.2.3	Buildup Factors for Lead	75
3.3.1.1	Relative Number of Gamma Rays (Fission) vs. Energy	80



FIGURE	PAGE
3.3.2.2.1 Regions for Al <sup>27</sup> (n,γ) Al <sup>28</sup> Calculations	87
3.3.2.4.1 Regions for H <sup>2</sup> (n,γ) H <sup>3</sup> Calculations	96
3.4.2.1 Regions for Photo-Neutron Calculations	110
4.4.1 Layout of Regions for Twenty Grand Calculation	138
4.4.2 Core Power Distribution	141
4.4.3 Flux Map	143
4.5.3.1 Viscosity and Thermal Conductivity of Heavy Water as a Function of Temperature	149
4.5.3.2 Density and Specific Heat of Heavy Water as a Function of Temperature	150
4.5.3.3 Heat Transfer Coefficient vs. Film Temperature for Flow Rate of 1850 gpm	151
4.5.5.1 Core Volume Element	155
4.5.5.2 Hot Channel Wall Temperature vs. Distance Above the Core Bottom	159
5.4.2.1 Finned Channel	180
5.4.3.1.1 Schematic Layout of Experimental Facility	182
5.4.3.4.1 Experimental Test Section	187
5.4.3.4.2 Experimental Test Section	188
5.4.3.4.3 Experimental Test Section	189
5.4.3.4.4 Thermocouple Arrangement on the Surface of the Coolant Channels	191
5.4.6.1 Smooth Channel Data	197
5.4.6.2 Average Values	199
5.4.6.3 Heat Transfer Coefficient vs. Position in the Coolant Channel	200
5.4.6.4 Transverse Finned Channel Average Values (Channel Inverted)	201





FIGURE		PAGE
5.4.6.5	Heat Transfer Coefficient vs. Position in the Coolant Channel (Channel Inverted)	202
5.4.6.6	Pressure Drop vs. Flow Rate	205
5.4.8.1	Longitudinally Finned Channel, Average Values	211
5.4.8.2	Heat Transfer Coefficient vs. Position in the Coolant Channel	212
5.4.8.3	Longitudinally Finned Channel	213
A-1	Conversion of Thermocouple Readings in Millivolts to °F	245
A-2	Thermal Conductivity (K) and $Pr^{0.3}$ as a Function of Temperature for Light Water	246
A-3	Viscosity ( $\mu$ ) as a Function of Temperature for Light Water	247



## INTRODUCTION

Since its completion in the Spring of 1958, the MIT Reactor has served as a vital research tool for the MIT and surrounding scientific community. At the time the MIT Reactor was designed, little was known of compact, heavy water moderated cores. Consequently, the MIT Reactor was designed with fuel element spacing sufficient to provide for a high percentage of neutron moderation to take place within the core area. Results published in 1964 upon the completion of the Brookhaven High Flux Beam Research Reactor provided the experimental information needed on compact, undermoderated core configurations in order to accomplish an exaggerated thermal flux peak in the reflector. By incorporating a similar compact core design into the MIT Reactor, it is reasonable to assume that the thermal flux coming out of the beam ports could be increased by at least a factor of three, and possibly as much as a factor of four or five. Such an increase would markedly increase the value of the MIT Reactor to research. In addition, if the beam ports were to be located below the base of the core, the core gamma ray and fast neutron background would be markedly reduced in intensity due to the fact that any core gammas and fast neutrons which leak out must have been scattered at



least once previous to escaping. Such a design would markedly increase the quality of the thermal neutron beam emitted from the beam ports.

It is primarily for the above reasons that a MITR redesign group was formed under the direction of Dr. T.J. Thompson. The design group is composed of both graduate students and MITR staff personnel. Besides Dr. Thompson and the author of this thesis, the members of the design group who have been active throughout the redesign process are graduate students: Andrews Addae working on core physics, Dan Kennedy working on beam port optimization, and Bob Sanders working on a cold neutron facility for the thermal column. Mr. Ed Barnett, working on all engineering phases of the redesign, represents the MITR staff.

Although never stated formally in writing, the design criteria outlined orally by Dr. Thompson at the outset of the design were the following:

- 1) The thermal neutron flux at the beam ports must be increased by a factor of 3-5.
- 2) The redesigned reactor must be as safe, or safer, than the existing reactor.
- 3) Simplicity of design must be a prerequisite for the design of any component.





4) There must be no buried mechanisms.

5) There must always be a means for retreat. To quote Dr. Thompson, "We have a going reactor, we don't want to replace it with a monument."

6) The redesigned reactor must be reliable.

7) The cost of the redesign project must be within \$500,000.

The redesign project has actually been divided into two distinct design phases. The first phase began in earnest in the Fall of 1967 and was centered around the design of a  $D_2O$  moderated, cooled and reflected reactor. Phase I concluded in the Fall of 1968 and was succeeded by an intermediate phase in which a mixture of  $H_2O$  and  $D_2O$  was considered as the moderator and coolant for the core, with pure  $D_2O$  as the reflector. In December of 1968 phase II began. Phase II is centered around the design of a light water cooled and moderated core surrounded by a heavy water reflector.

At the outset of phase I, it was apparent that there would be many challenges in the area of mechanical design. The incorporation of a compact core configuration dictated that new methods be devised to support not only the fuel elements, but the control elements as well. A change in core tank design seemed to be required. This author's first responsibility as a member of the redesign team was, then, to attempt to find solutions to some of the many



design problems confronting the redesign project. The work done toward this objective is summarized in Chapter 2 of this thesis.

As the redesign project continued and a necked coolant tank was adopted, concern for the requirements of reactor top shielding emerged. This author's second area of responsibility became, therefore, that of designing the shielding to be required for the reactor top, and that of performing shielding calculations to justify the proposed shield composition. The results of work done in this area are presented in Chapter 3 of this thesis.

As stated at the beginning of this introduction, one of the primary purposes for redesigning the MITR was to accommodate a compact core configuration in order to obtain a large thermal flux peak in the reflector. However, almost by definition the achievement of a pronounced thermal flux peak in the reflector will be accompanied by a sharply increasing thermal flux gradient across the outermost fuel plates. The outermost fuel plates will consequently generate a much higher power density than the inner fuel plates in the core. From the results presented in reference (1), it is reasonable to suspect that due to the sharply rising thermal flux gradient in the area of the outermost fuel plates, the reactivity coefficient due to coolant voiding in the channels adjacent to these fuel



plates may be positive. It, therefore, becomes imperative that boiling not be allowed to occur in the area of the outermost fuel plates, which is equivalent to saying that boiling must not occur anywhere in the core since the outermost fuel plates generate the most power. The maximum rate at which heat can be removed from the outermost fuel plates without allowing nucleate boiling to occur thereby sets an upper limit to the power density allowable in the outermost fuel plates, which in turn influence the maximum thermal flux peak which can be obtained in the reflector. It is this critical area of core heat removal which became this author's third and final area of responsibility. The results of work done in this area are presented in Chapters 4 and 5 of this thesis.



## Chapter 1

## DESCRIPTION OF EXISTING MITR COMPONENTS

1.1 General

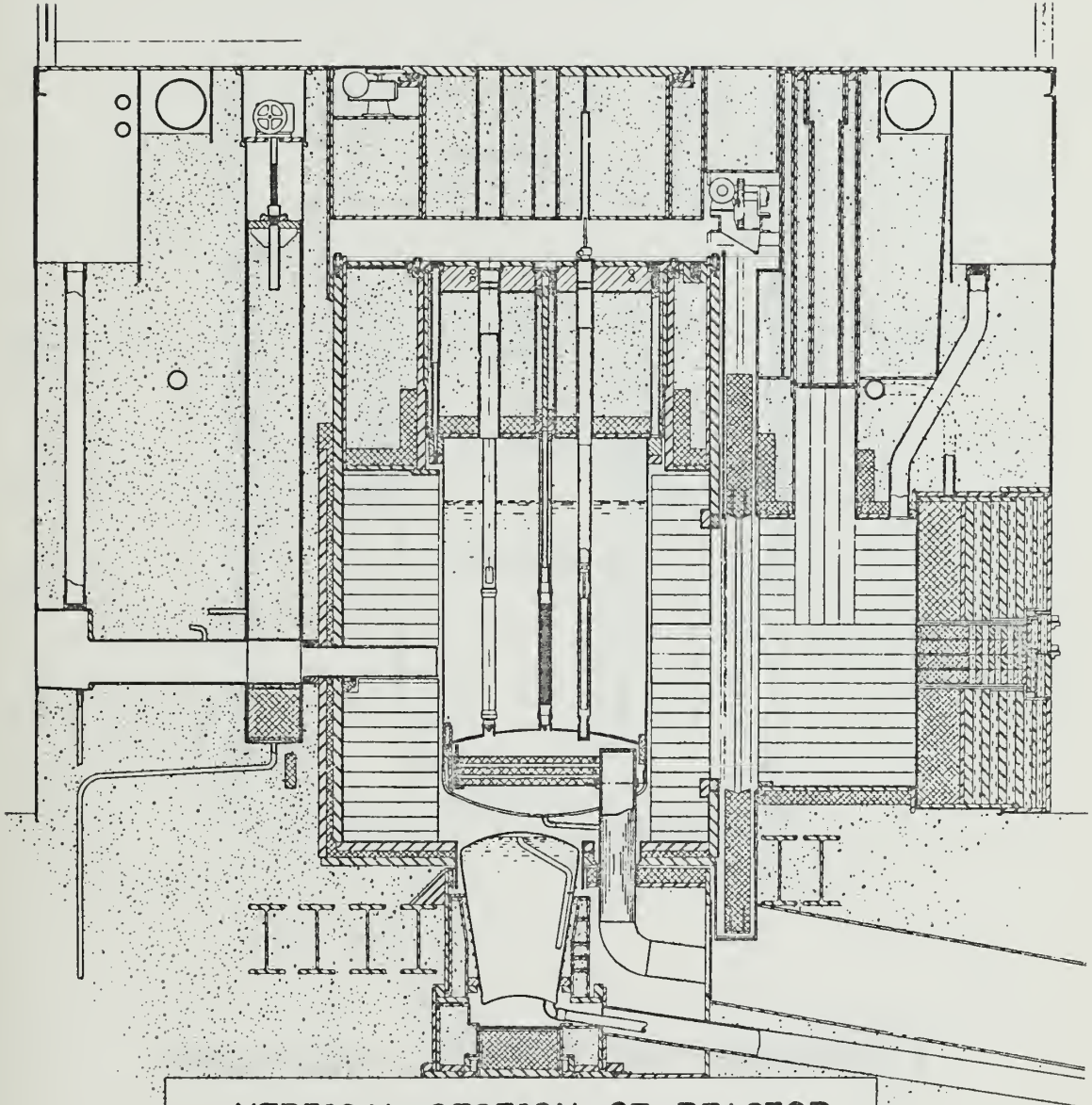
Before proceeding with a description of the design and calculational work which was performed as a part of the High Flux MITR Project, it seems appropriate to first present a brief description of those existing MITR components and systems which are the subject of redesign work presented in this thesis. The following information was taken from the operating manual for the MIT Reactor (2). The operating manual should be consulted if more detailed descriptions are desired.

1.2 Reactor Coolant Tank

The reactor tank is 48 inches in inside diameter and has a wall thickness of 1/4 inch, except at the bottom where it is 3/8 inch thick. The overall height from the dished bottom shell to the top flange is 7 feet 5-3/8 inches. The reactor tank is made of special high purity aluminum and has a design pressure of 40 psig. During normal operation, however, the pressure in the tank above the coolant is only 1 inch of H<sub>2</sub>O above atmospheric pressure. The tank is shown in the vertical section through the reactor of Figure 1.2.1, and is also shown in Figure 1.2.2.

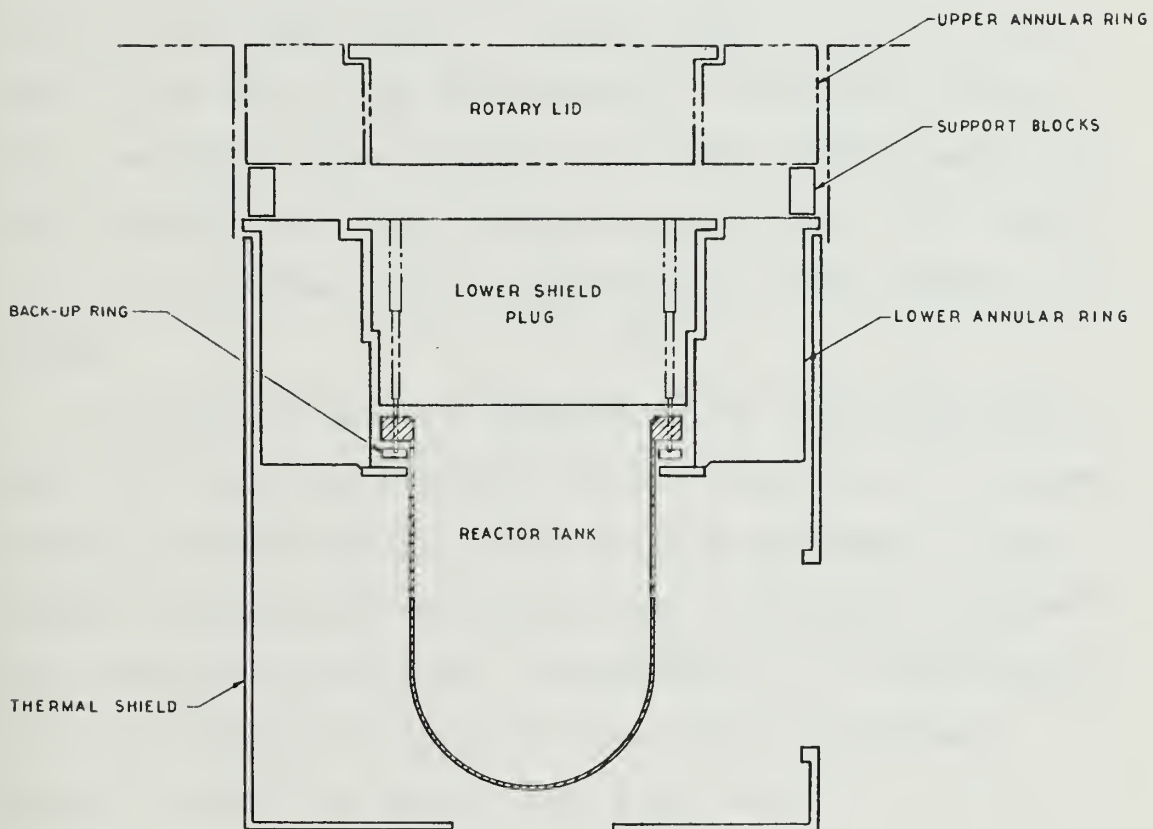






VERTICAL SECTION OF REACTOR  
FIGURE 1.2.1





REACTOR CORE TANK SUPPORT  
FIGURE 1.2.2



Heavy water flows into the reactor tank through an 8 inch diameter aluminum pipe, through the holes in the side of the inlet pipe cap and out into the entrance plenum. It then flows up through the fuel elements and out into the tank itself. The  $D_2O$  from all the fuel elements flows out of the tank through a transition section which extends a short distance above the plenum head, and then through the 8 inch aluminum outlet pipe. The normal total coolant flow rate is approximately 2000 gallons per minute.

The reactor tank is attached to the lower shielding plug by 24 one inch stainless steel socket head cap screws. The cap screws compress a hollow stainless steel O ring between the tank and the shield plug to provide a helium seal designed for 80 psig. Consequently, if a high pressure is developed in the tank, the tank will rupture downward before the shield plug gives way.

### 1.3 Shielding Above the Core

#### 1.3.1 Lower Annular Ring

The lower annular ring (shown in Figures 1.2.1 and 1.2.2) is a concrete-filled steel structure which is 56 in. in inside diameter, approximately 8 ft. in outside diameter, and 4 ft. high. Its lower surfaces are covered with 1/4 in. of boral. A 4 in. thick, water-cooled lead thermal shield lines the inner surface over the lower 18 in. There are conduits for thermocouple leads and helium



gas pipes, and 6 sleeves are provided for thimbles which slant into the graphite reflector.

### 1.3.2 Lower Shield Plug

The lower shield plug is a large cylindrical structure, the bottom of which is lined with a 1/4 in. sheet of boral. Above the boral is a 1-1/8 in. steel plate, 4 in. of lead provided with cooling coils, 29 in. of concrete, a steel cover plate, a 6 in. space filled with paraffin and steel shot, and a 1-1/8 in. stainless steel top plate. The plug is penetrated by numerous sleeves for the concrete-filled steel shielding plugs which are part of the fuel element and control rod assemblies.

### 1.3.3 Upper Annular Ring

The upper annular ring, together with the rotary plug, complete the biological shielding above the core tank. The three foot thick annulus is made of dense concrete encased in steel. Plugged holes are provided for access to the vertical thimbals which protrude through the lower annular ring and into the graphite region. The upper annulus is spaced 9-1/4 in. from the lower annulus by several supporting blocks bolted to the lower annular ring flanges.

### 1.3.4 Rotary Plug

The heavy concrete rotary plug fits into the center of the upper annular ring and rests on a ball-bearing thrust ring. It is rotated by a drive motor and friction belt. When the plug is latched in its operating position,







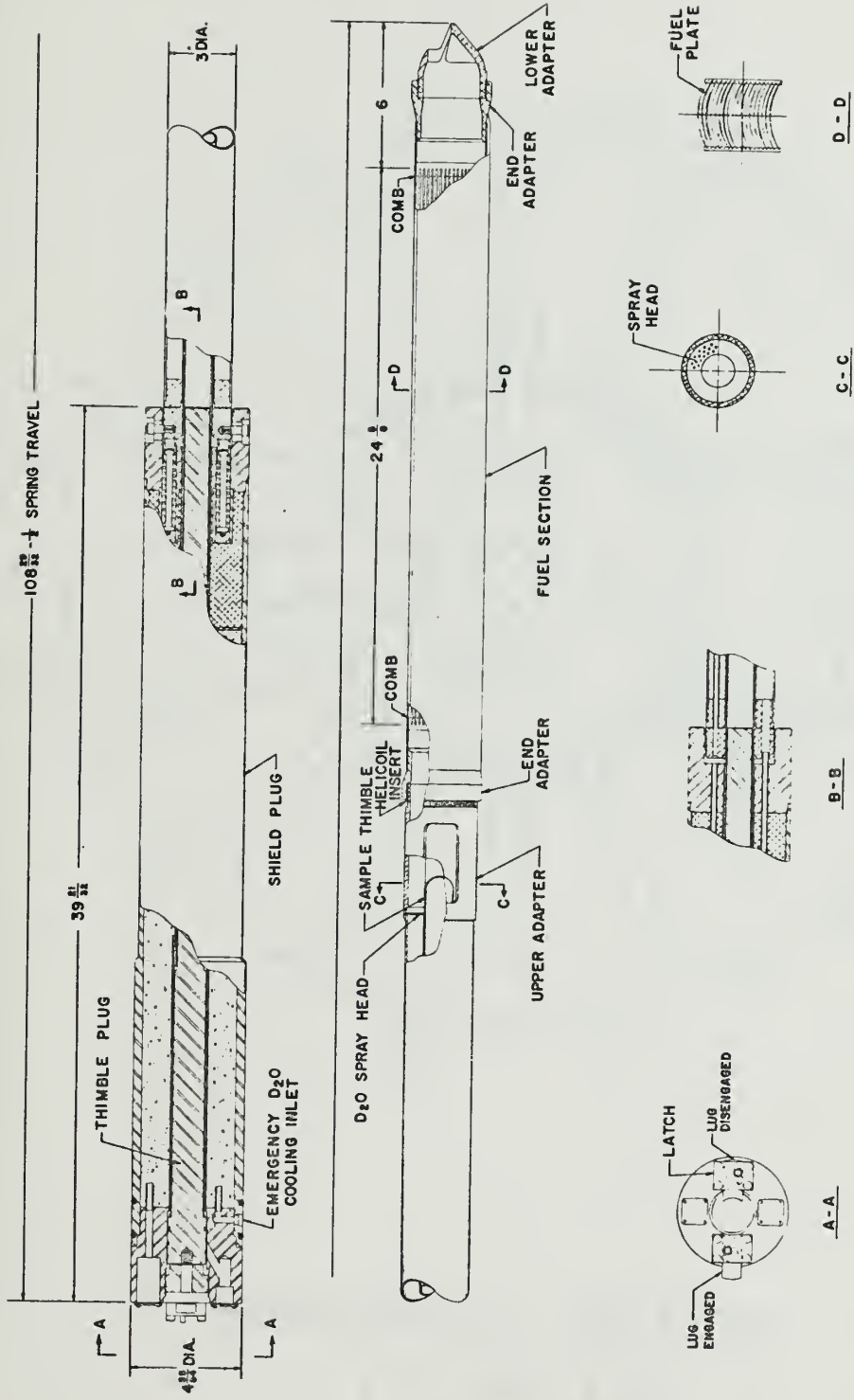
the control rod racks can move upward into cylindrical slots in the bottom of the plug. To remove a fuel element, the control rods must be fully inserted and the plug unlatched and rotated to the appropriate indexed position. The shielding plug directly over the fuel element position can then be removed. The entire rotary plug must be removed for access to the control rod drives.

#### 1.4 Fuel Element Assembly

A fuel element assembly is shown in Figure 1.4.1 and consists of a fuel section supported by a lower adapter, an upper adapter and a shield plug. The 30 positions into which fuel assemblies can be inserted are indicated by numbers 1 through 30 in Figure 1.4.2. There is a central element position surrounded by an inner circle of 6 positions, all spaced 6.375 in. center-to-center. These in turn are surrounded by an outer circle of 12 positions spaced 6.858 in. center-to-center. The 11 additional positions are located around the outside edge of the reactor tank.

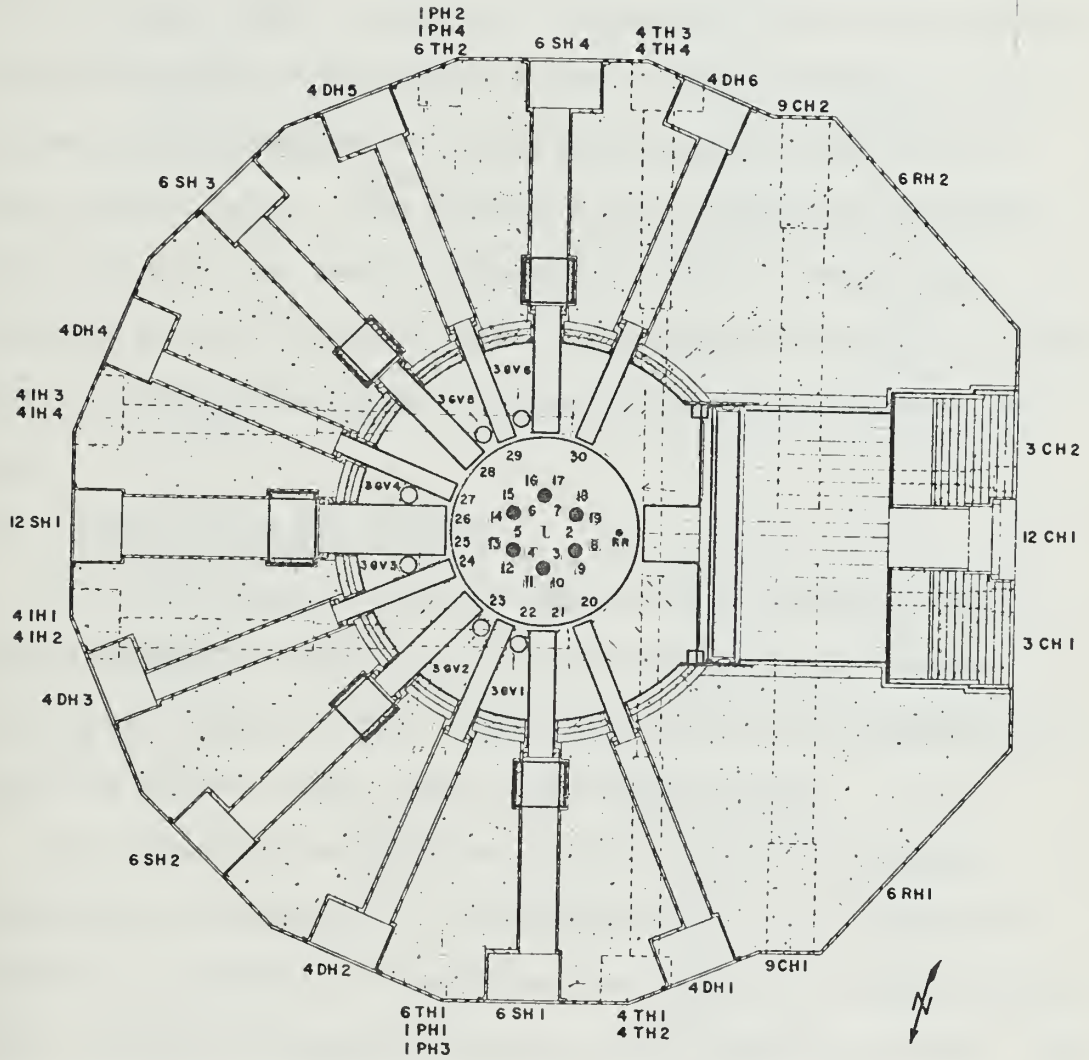
The fuel section consists of 18 curved plates assembled between two grooved side plates which are 0.187 in. thick and 3.168 in. wide. Two nonfuel-bearing outer plates are 0.060 in. thick and are curved to a 5-1/2 in. radius. They are spaced 0.117 in. apart to form 17 cooling water passages.





FUEL ELEMENT ASSEMBLY  
 FIGURE 1.4.1





HORIZONTAL SECTION  
FIGURE 1.4.2



The fuel assembly shielding plug fits into a stepped steel sleeve embedded in the lower shield plug. The weight of the assembly rests on the step in the lower shield plug. This provides a convenient means of removing the fuel assembly through the tank top, and when in place the shielding properties are equivalent to that of the lower shield plug. The shield plug is securely latched into place by two small lugs which slide outward and engage a groove in the sleeve. The lugs are moved by turning a square projection on a cam which bears against the lug.

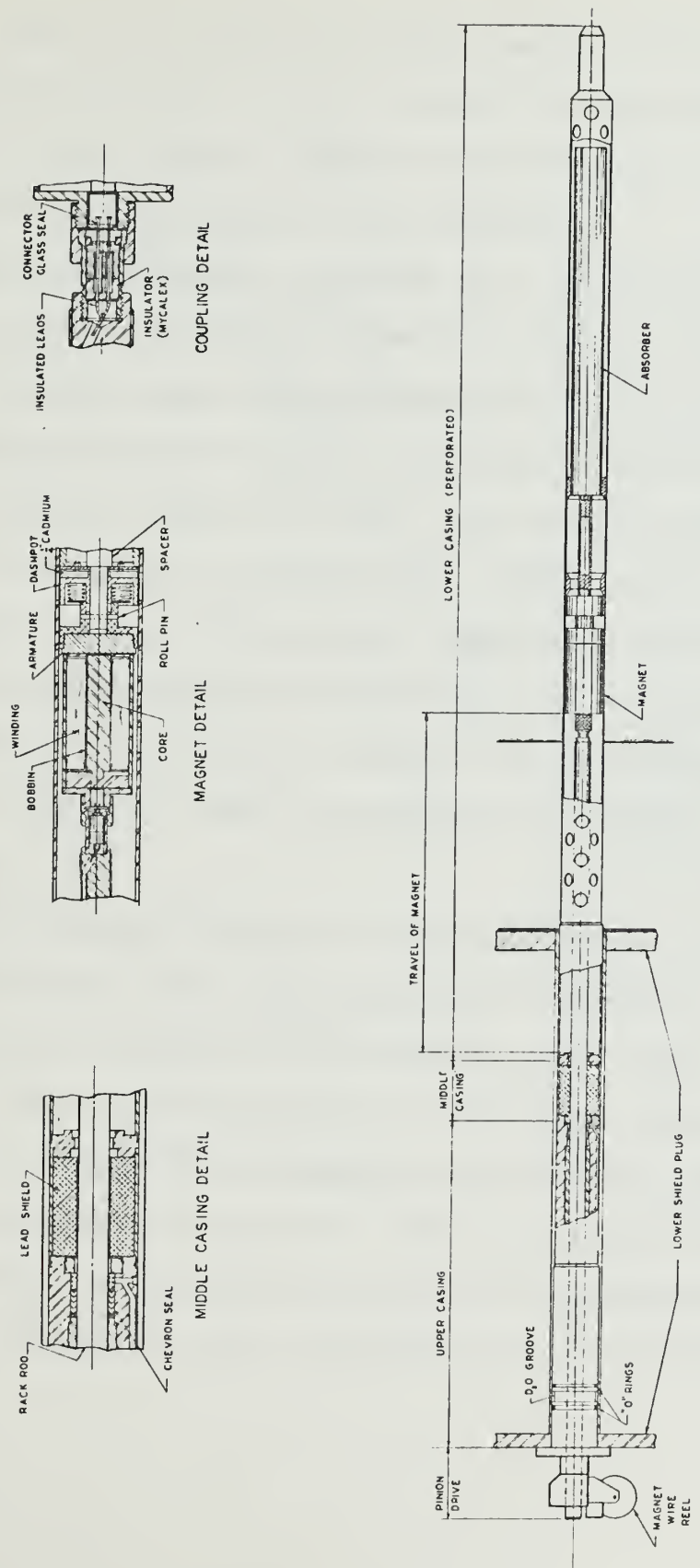
#### 1.5 Control Rod Mechanisms

The MITR has one regulating rod and six shim safety rods arranged in the core as shown by the solid black circles in Figure 1.4.2. The shim safety rod assembly is shown in Figure 1.5.1 and is described below.

The absorber section is a hollow, double-walled, aluminum cylinder, 28 in. long and 2-1/4 in. in outside diameter, in which is sandwiched a 0.040 in. thick cadmium tube 2.15 in. in outside diameter and 26-1/8 in long. The absorber cylinder is connected to the magnet armature (a nickel-plated soft iron disk) and dashpot by means of a spider-like section, thus permitting  $D_2O$  to flow freely through the top of the cylinder as it drops. During a reactor scram as the absorber nears its fully inserted position, it is decelerated by a cushion of heavy water







MODIFIED SHIM-SAFETY ROD ASSEMBLY  
FIGURE 1.5.1

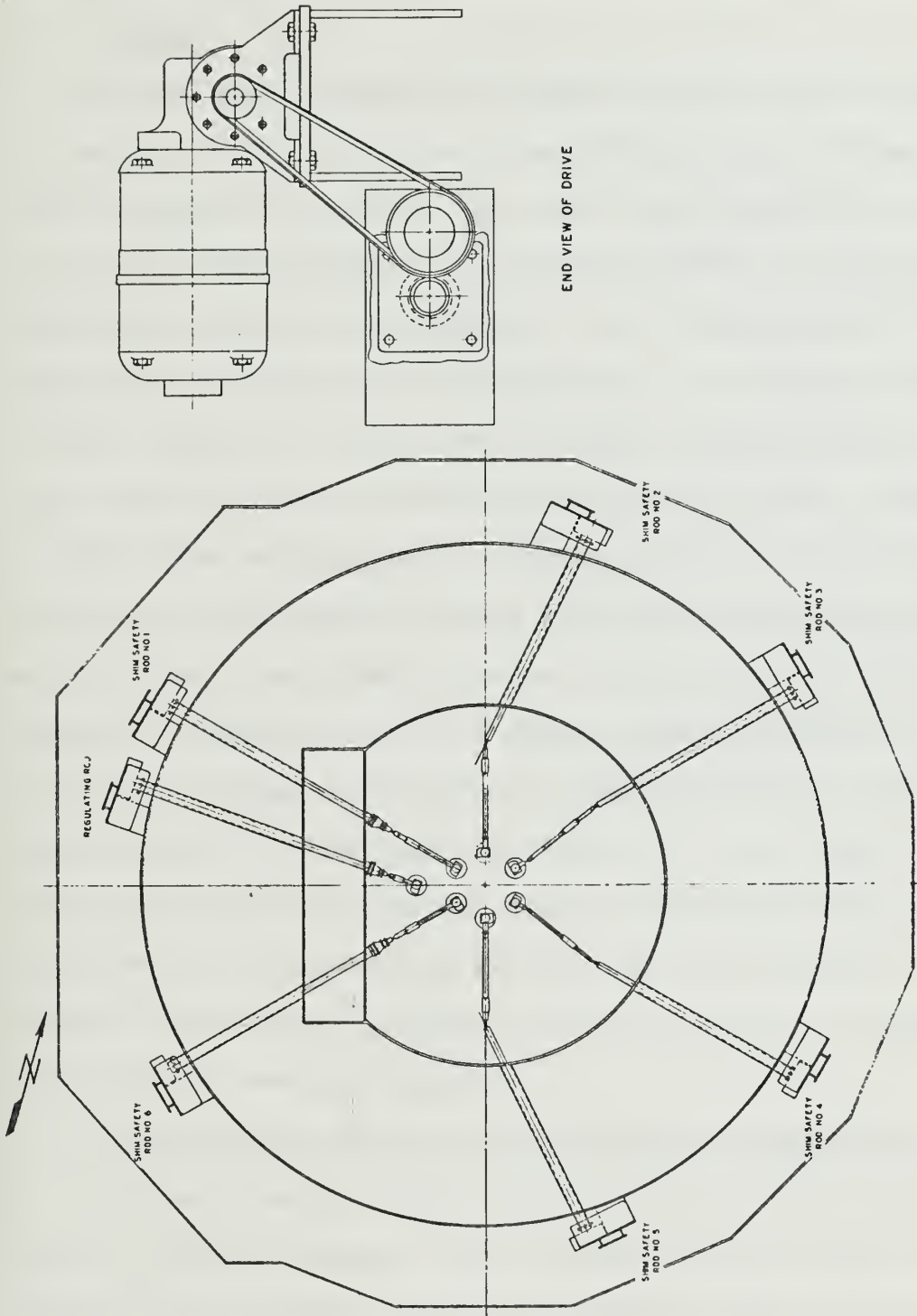


which leaks off between a washer and the dashpot case with the assistance of coil springs in the dashpot. A 1/4 in. thick disk of cadmium on the bottom of the dashpot shields the iron armature from neutrons.

The electromagnet consists of a silicon-insulated copper wire, wound onto a transite bobbin. It is fitted into an Armco magnet-iron housing which is enclosed by two stainless steel end plates. The magnet wires are connected to a threaded connector, which, when coupled with the racks forms a hermetically sealed unit. Magnet wires are led through a tube in the rack rod, then down the outside to a take-up reel mounted at the top of the casing assembly. The rack is guided by the casing, and the escape of helium or  $D_2O$  around the shaft is prevented by Styrene chevron packing.

The rods are driven by a rack and pinion arrangement. The drive shaft from the pinion gear extends to the motor and gear box assembly at the utility shelf (see Figure 1.5.2). The six drive shafts are arranged radially but differ in length and arrangement in order to clear shutters and experimental facilities. All drive shafts are enclosed in sleeves from the utility shelf to the between-plug space, and are sealed to limit the amount of  $A^{41}$  entering the air stream.





MECHANICAL ARRANGEMENT OF CONTROL MECHANISMS  
FIGURE 1.5.2



## Chapter 2

## PRELIMINARY MECHANICAL DESIGN STUDIES DONE FOR PHASE I

2.1 General

In the early stages of the MIT reactor design project it was this author's primary responsibility to attempt to find solutions to some of the many design problems critical to the construction of a High Flux MITR. In so doing many design ideas were proposed, few of which gained acceptance by the entire design group. It is the purpose of this chapter to relate some of the design proposals which can be primarily attributed to this author, though at times when working with a design group it is admittedly difficult to distinguish which ideas are completely one's own from those which may have had their roots in, for example, a comment made at a design group meeting. It is felt that although a particular design scheme may not have appeared best for the MITR redesign, it may at some future date prove useful to another reactor design project, and therefore is worthy of description in this chapter. In addition, the design proposals serve as a kind of chronology of mechanical design progress.

2.2 Core Tank and Reactor Top Shielding Configuration

The basic necked core tank design as finally adopted evolved from the compact core concept and short tank proposed in the original redesign sketches of Prof. T.J. Thompson

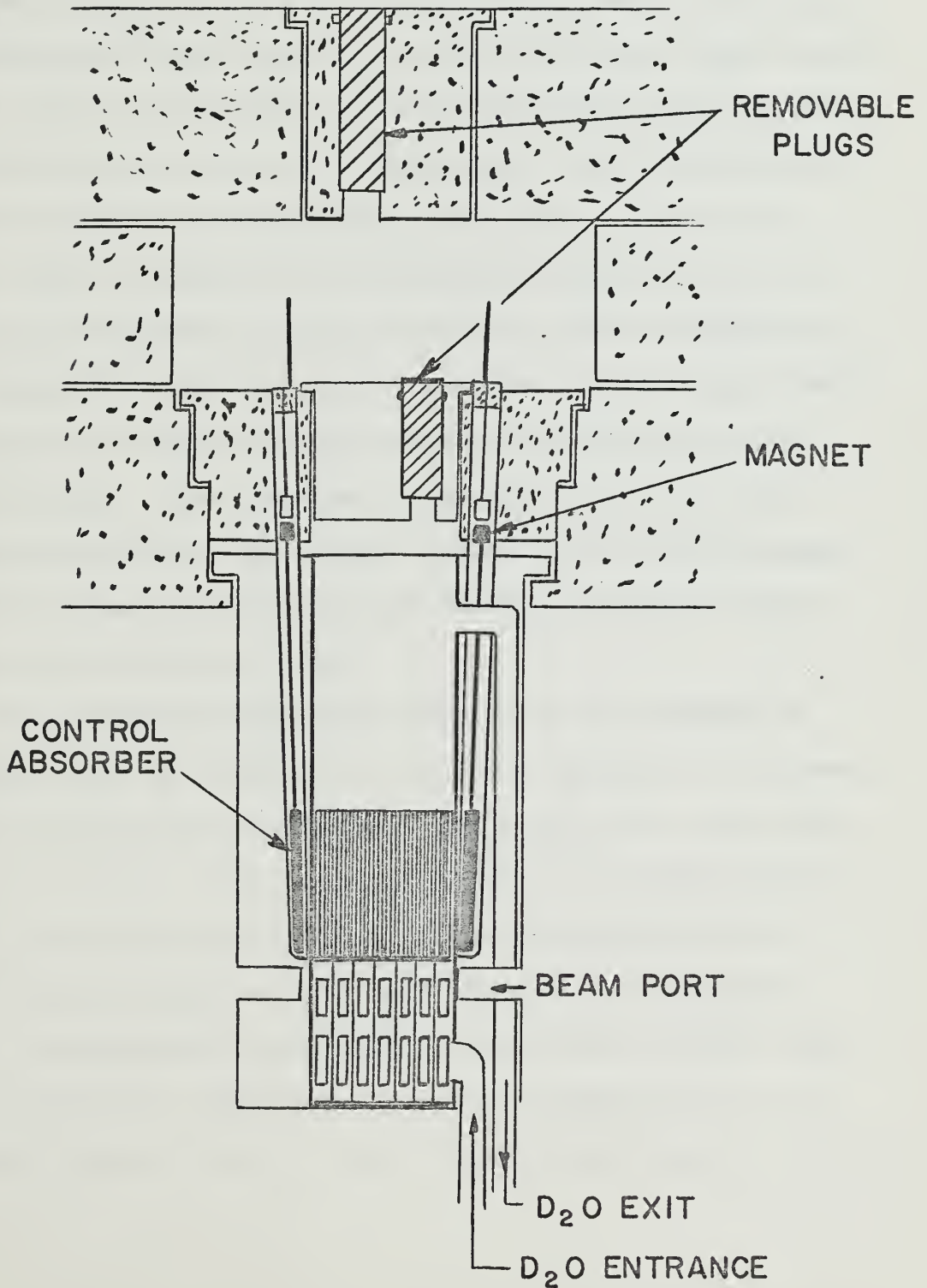




and first formally reported in August 1966 in a 22.90 project report by D.M. Goebel (3). The original purpose in designing a necked core tank was to provide for adequate shielding of the core during refueling operations. (Prior to the introduction of an enclosed refueling structure atop the reactor, it was proposed that there be a single refueling plug which would be removed during refueling operations. Without approximately 11.5 feet of  $D_2O$  separating the core from the reactor top, the radiation level would be prohibitive to workers in the area of the open refueling plug.) In order to accomplish the objective of providing adequate shielding during refueling operations, but at the same time to minimize the required  $D_2O$  inventory, the concept of two rotating shield plugs was conceived and originally proposed by this author. This design concept, outlined in Figure 2.2.1 would utilize a 1-1/2 ft. thick lower shield plug fabricated of lead which would rotate around a track of aluminum rollers. Releasable latches would prevent the shield plug from being "shot" upward by a sudden increase in reactor pressure. Inserted in the lower shield plug would be three 6 in. diameter removable lead plugs, so situated that by rotating the lower shield plug one of the smaller plugs would be caused to line up atop any desired fuel element. A tool inserted from the reactor top through the upper shield plug could be used to



DOUBLE ROTATING SHIELD PLUG





unlatch a 6 in. diameter lead plug, lift it out of its slot, and set it aside. The upper rotating shield plug would consist of 3 ft. of dense concrete, and would rotate on stainless steel rollers and contain three 6 in. diameter removable plugs similar to those of the lower shield plug. An inflatable boot would be located around the upper shield which could be deflated to allow the shield plug to rotate and inflated to act as a helium seal. (An inflatable boot could be installed around the lower shield plug if the upper shield plug should be entirely removed in order to perform maintenance on the control rod drive mechanisms, for example.) Both the upper and lower shield plugs would be cooled by duplicate  $D_2O$  cooling coils cast into the shield plugs. When rotated to an indexed position for reactor operation, the coolant lines in the shield plugs would be caused to line up with their respective supply lines in the annular rings.

The refueling operation would proceed somewhat as follows: One of three 6 in. diameter inserts in the lower shield plug would be unlatched and raised by a tool inserted from above. The lower shield plug would then be rotated to an indexed position aligning the opening in the lower shield plug over the fuel element to be removed. The 6 in. diameter plug could then be rested on the lower shield plug for convenience. Next the appropriate 6 in. diameter insert from the upper shield plug would be removed.



At this time, the insert would not be aligned with the opening in the lower shield plug. The refueling flask would be brought into position on the reactor top, the upper shield plug rotated to an indexed position so as to align its opening above the fuel element to be removed, and the designated fuel element raised up into the refueling flask. Once in the refueling flask, the fuel element could either be flipped end for end and reinserted into the reactor, or set aside while a new fuel element is placed into the core. The above procedure would be accomplished in reverse to complete the refueling operation.

By utilizing the concept of a double, rotating shield plug, the reactor  $D_2O$  tank would remain shaped similar to the present  $D_2O$  tank (see Figure 1.4). Two important differences would be apparent, however. Although 4 ft. in diameter, the  $D_2O$  tank would be shortened from 7-1/2 ft. to 6-1/2 ft. in height. The volume of  $D_2O$  in the system would thereby be decreased by 14%. Contained within the 4 ft. diameter outer tank would be an inner tank of diameter just sufficient to contain the core. This inner tank would extend the full length of the outer  $D_2O$  tank and would be constructed of sufficient thickness of aluminum to be able to contain a sudden  $D_2O$  vaporization resulting in 40 psi overpressure in the core. As a consequence, the 4 ft. diameter  $D_2O$  tank need only be of sufficient strength







to support the coolant contained within it. There are two major reasons for utilizing an inner tank to separate the core region from the reflector region. First is the possibility of maintaining the reflector  $D_2O$  at a lower temperature than the coolant  $D_2O$ , and thus make the reflector  $D_2O$  a better moderator. Second is that by separating the reflector from the core, the entire reflector region could be rapidly dumped of its  $D_2O$ , thus creating a very important mechanism for reactor safety.

Both the upper and lower annular rings would remain the same as in the present MITR, and the core tank likewise would be supported as it is now. Such mechanical similarities with the existing reactor would tend to reduce the cost of converting to the high flux MITR core configuration.

The control rod mechanisms for the above described reactor tank configuration would extend through the lower annular ring in a manner similar to the present MITR design. The absorber section would protrude into the reflector region adjacent to, but outside of the inner tank wall. The control rod drive motors and connecting shaft work could remain and be used in their current positions. Maintenance could be performed on the control rod mechanisms by removing the upper shield plug, thus allowing a man to enter the area between the upper and lower annular rings.



From the above description it would appear as if the above described core tank design with a double, rotating shield plug mechanism has no drawbacks and should have been adopted. Where the above design fails is that it does not sufficiently conform to two of the design criteria mentioned in the thesis introduction which have played a major role in the selection of final mechanical designs for the High Flux MITR. These criteria are that the design selected should be the ultimate in simplicity, and should have no hidden mechanisms. The mechanics involved in the concept of a double rotating shield plug with an inflatable helium seal are not what could be described as simple, and the mechanisms associated with the lower rotating shield plug could be considered as hidden.

## 2.3 Core Support Mechanism

### 2.3.1 General

Of major concern to the redesign of the MITR core area was the method by which the core is to be supported. It is possible that the core receive its primary support either from below or by being hung from above. The core support mechanism selected for use in the phase I High Flux MITR (designed by Mr. E. Barnett) supports the core from below. The overwhelming reason for the choice of this mechanism to support the core from below was safety. In the design of a reactor in which the sudden removal of a fuel element from



its core position would cause a reactivity addition on the order of 3% in  $\Delta K/K$ , as is the case for the High Flux MITR, it is imperative that each fuel element be supported in an absolutely foolproof manner (4).

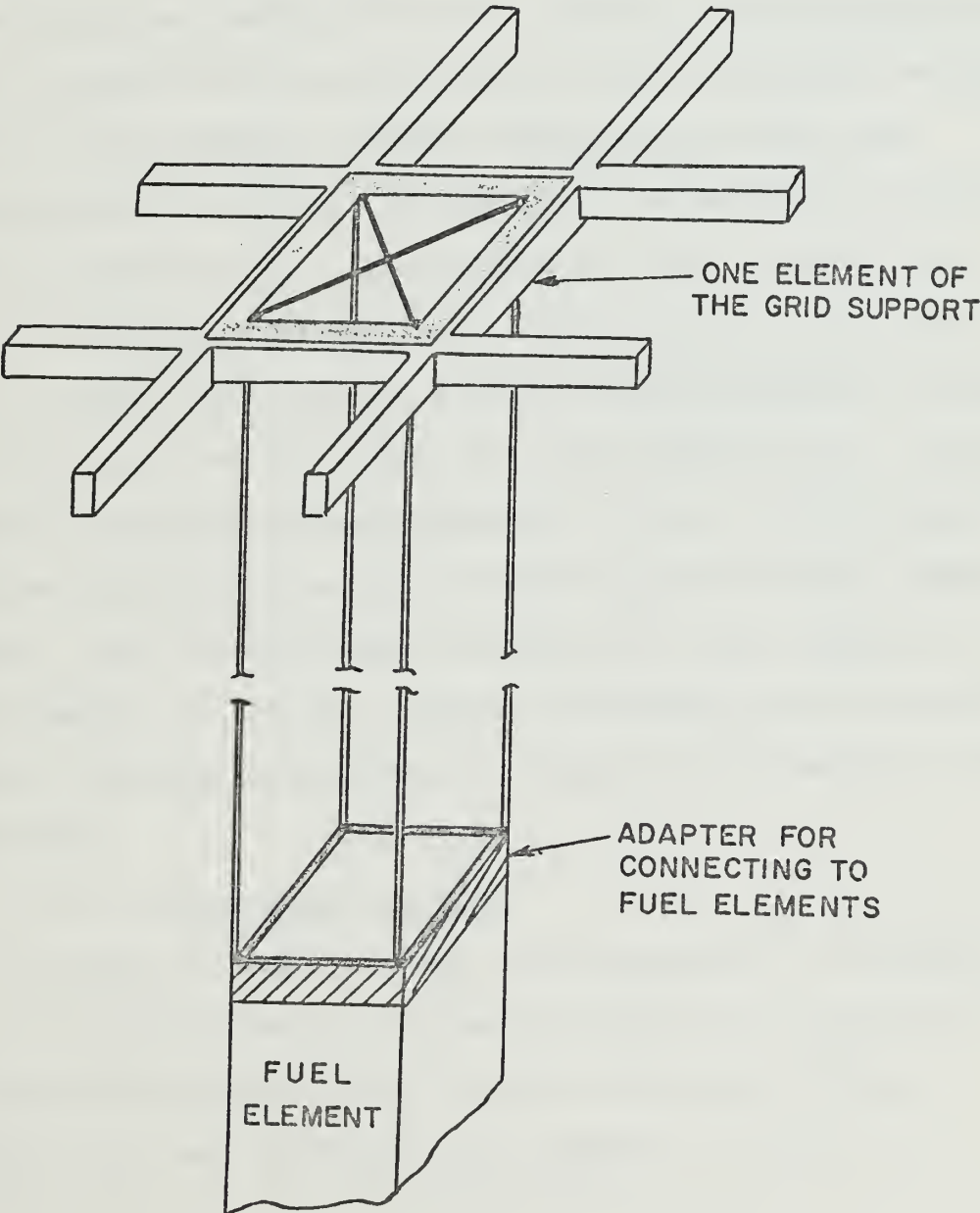
There is, however, one very compelling reason for wanting to support the core from above. The aluminum structure necessary to support the core from below results in a loss on the order of 20% in thermal neutron flux in the area below the core (5). It is this area just below the core at which the beam ports "look". In addition, having the aluminum structure below the core results in an increased gamma flux seen by the beam ports due to the thermal neutron activation of  $Al^{27}$ .

### 2.3.2 Grid Support

The first design proposed as a means of supporting the core from above is shown in Figure 2.3.2.1. In this design the core is hung from a grid-like structure, the grid being supported either directly by the lower annular ring in the case of the double shield plug design, or from the base of the necked region of the core tank in the case of the necked core tank design. An adaptor which is capable of being attached to either end of the fuel element would be connected by four aluminum rods to the corners of a rectangular plate. The plate would rest on top of the grid support bars when the fuel element is inserted into the core. A hinged cover would be lowered over the grid structure and latched



FIGURE 2.3.2.1  
GRID SUPPORT







in order to hold the fuel element support plates down. There is both a major design concept advantage and a major disadvantage in this method of core support. The advantage is that with such a method both the core and the control elements are supported from the same structure, the lower annular ring. Therefore, should a major catastrophe (such as an airplane crashing into the reactor or an earthquake) occur in which the reactor structure was disturbed, having the core and control elements supported from the same structure would markedly increase the probability of their staying together; i.e., one should not fall without the other. The disadvantage to the above method of core support is that there must be a space between each fuel element of width equal to the width of a grid support bar. The grid support bars must be approximately 1/4 in. wide in order to provide a sufficient area on which to rest the fuel support plates. This spacing would increase the core diameter by approximately 1-1/2 in., thereby decreasing the core power density, thereby decreasing the thermal flux peaking in the reflector.

### 2.3.3 Sliding Bar Support

In order to support the core from above, but without the spacing between fuel elements required by the method of the preceding section, a design utilizing sliding support bars was developed (see Figure 2.3.3.1). (A



SLIDING BAR SUPPORT

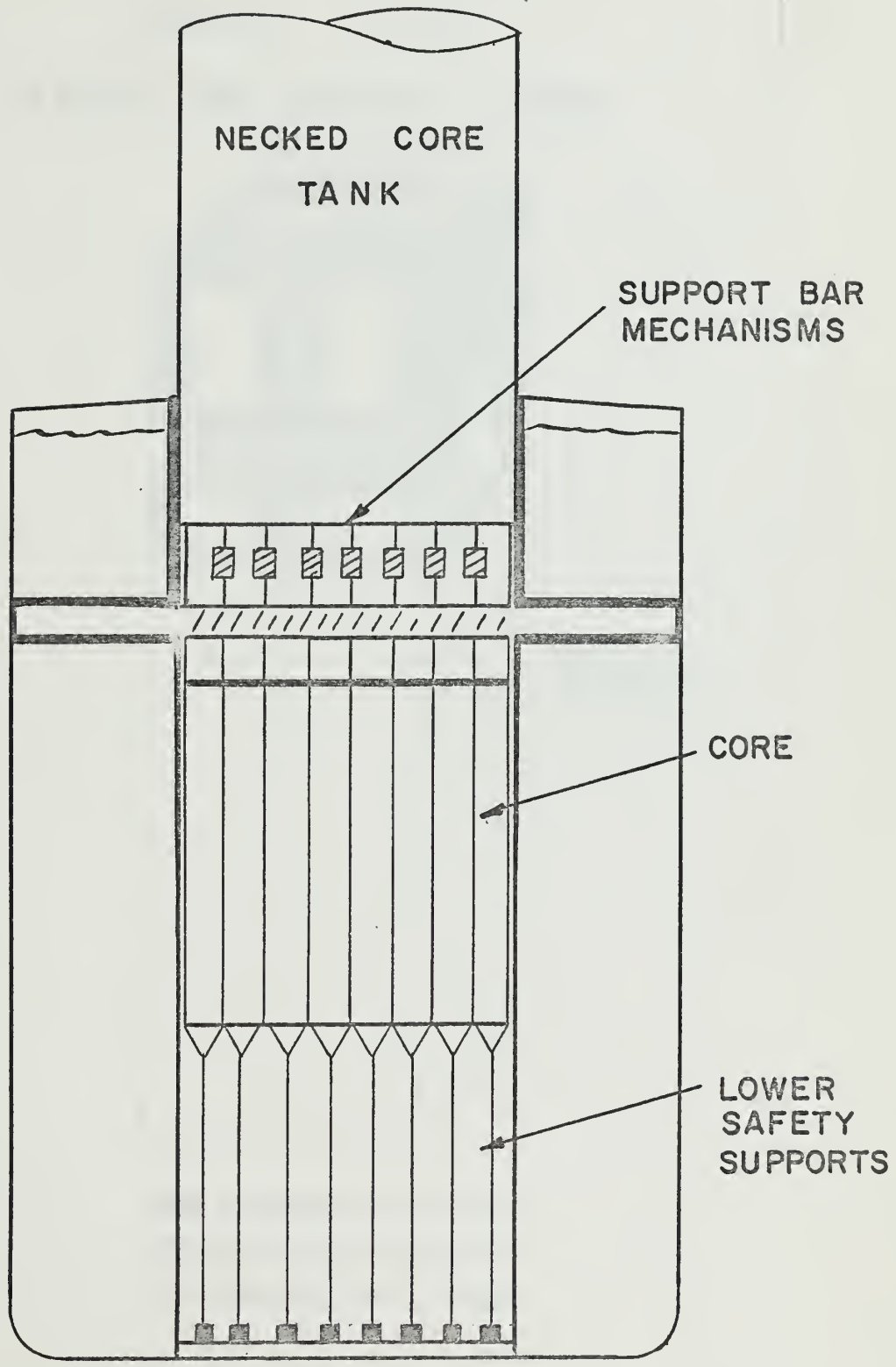
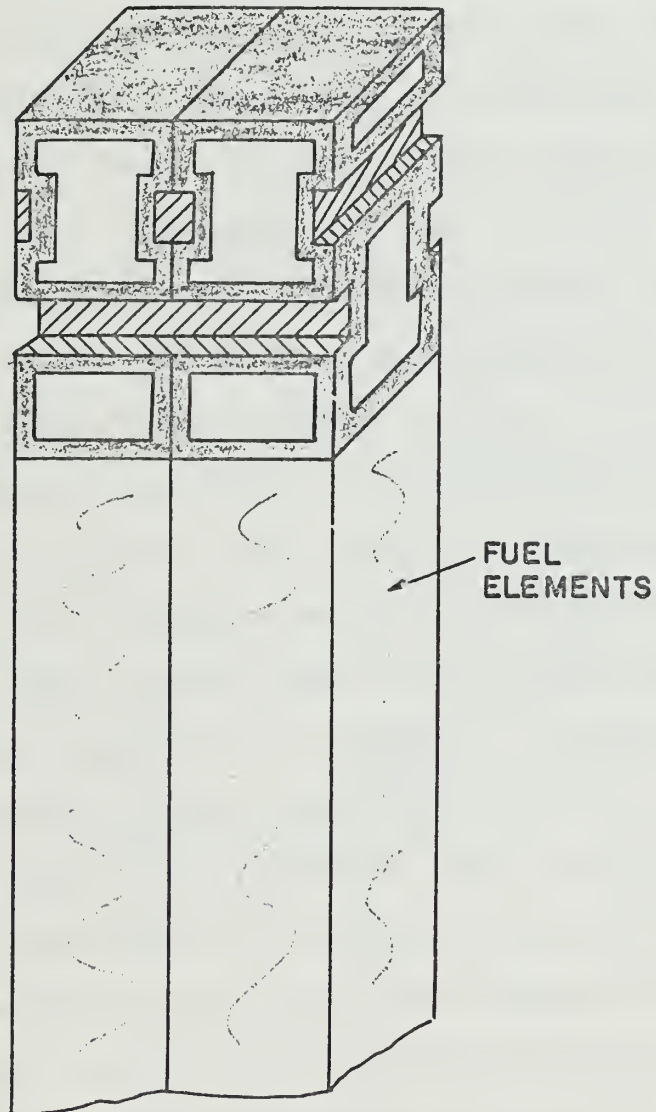







FIGURE 2.3.3.2  
SLIDING BAR SUPPORT-UPPER  
ADAPTER



-  ALUMINUM STRUCTURE
-  SUPPORT BAR SLOTS
-  COOLANT EXIT AREAS

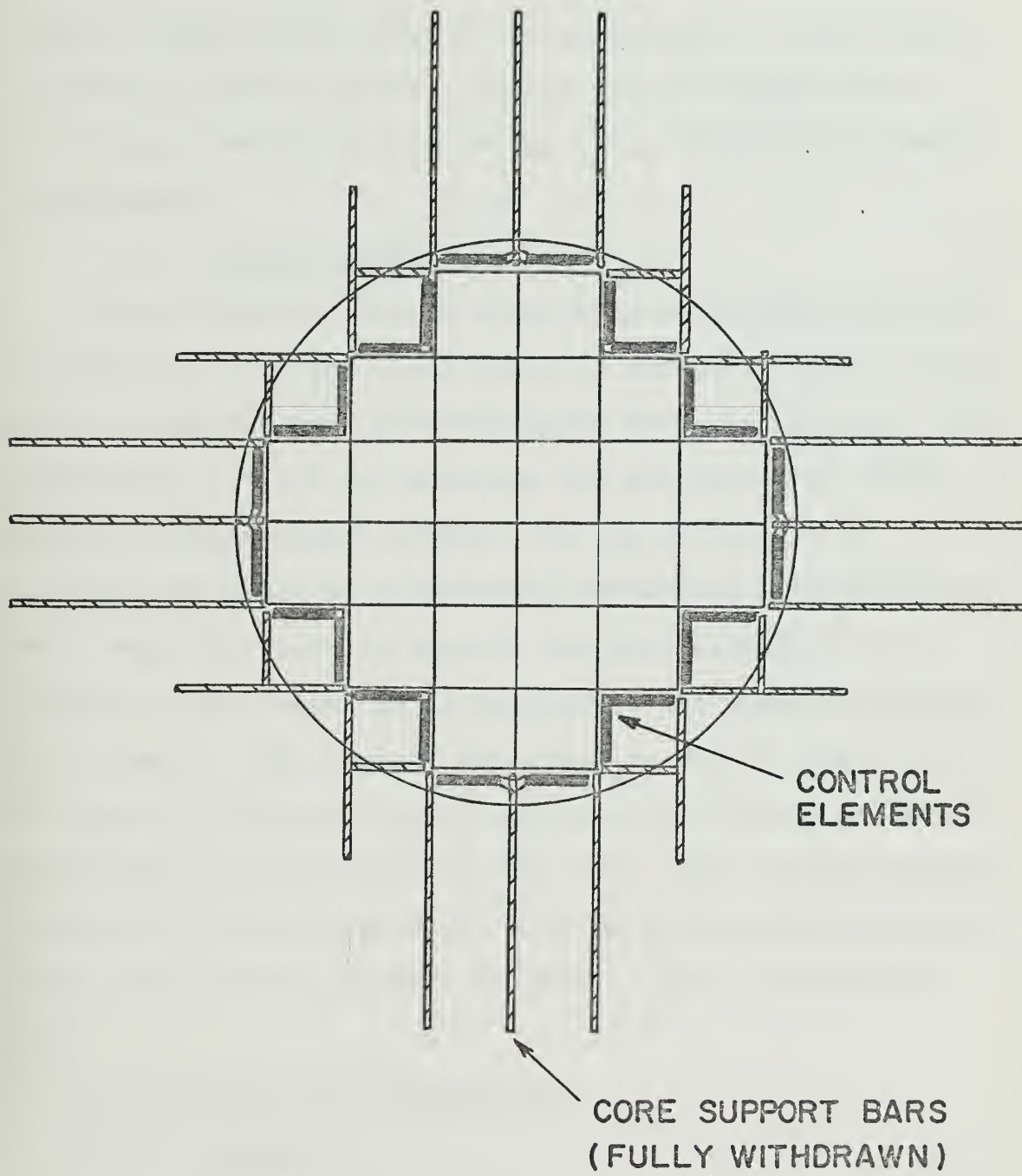


design of this general type was proposed earlier by Dr. Thompson and Mr. Barnett.) Assuming for the sake of illustration, a 24 element core configuration, a system of 14 east-west and 14 north-south tracks would be constructed around the core. The tracks would be attached at one end to the outer tank wall and supported at the inner end by the inner tank wall plus a brace hung from the necked region of the reactor tank. On these tracks would slide the core support bars, seven bars for each quadrant of the core. Special frame type structures with keyhole indentations would lock either end of the fuel elements and accept the sliding core support bars (figure 2.3.3.2). In order to refuel the support bars would be withdrawn in such a manner as to allow only one fuel element to be released at a time. An interlock mechanism would prevent the withdrawal of support bars in any manner which would cause more than one fuel element to be released. The fuel element support structures being frame-type structures with openings on all sides, the  $D_2O$  coolant would flow up through the core and out the sides of the support structure. Although not a necessity, the top of the support structure could be made solid in order to help prevent the  $D_2O$  coolant (with its  $N^{16}$  activity) from being circulated into the upper portion of the core tank after leaving the core. As shown in Figure 2.3.3.3, the sliding support bar design





FIGURE 2.3.3.3  
SLIDING BAR SUPPORT-  
BARS WITHDRAWN





would require that the control elements be angular shaped to conform to the outline of the core.

The major shortcoming of the sliding bar support mechanism is the necessity to design an interlock which would be absolutely foolproof in preventing the accidental release of a fuel element. It can also be argued that this design certainly does not meet the "simplicity" design requirement.

#### 2.3.4 Safety Supports

From a safety point of view, both the designs proposed in Sections 2.3.2 and 2.3.3 would be enhanced if some backup means of support were provided below each fuel element. For this purpose, a 1/4 in. aluminum rod set into the coolant entrance plenum would suffice. On top of the 1/4 in. aluminum rod would be a structure resembling a crow's foot which would act both to support the fuel element and to turbulate the coolant as it approaches the entrance to the fuel element. The support bar could be removed and replaced by a bar of different length should it be desired to change the height of any element in the core. The aluminum support bars serve only one function, that of acting as a backup to ensure that no fuel element is able to fall through the core.

### 2.4 Control Rod Drive Mechanisms

#### 2.4.1 General

One of the most difficult design problems encountered in the redesign of the MIT Reactor was the location of the



control rod drive mechanisms. Since it was desired to retain the present concept of a magnetic coupling between the control absorber and withdrawal shaft, it became a design premise that the control rod drive mechanism be designed in such a manner as to allow the magnet to be located as far from the core as possible, and if possible outside the  $D_2O$  tank. By doing so, it was hoped that magnet failures due to radiation damage and moisture corrosion could be eliminated, or at least reduced markedly in comparison with the rate of failures in the present MITR. The magnetic coupling between the control rod drive motor and the control absorber was envisioned to be either the general type used in the present MITR or a magnetic clutch arrangement. Some of the proposed designs and locations for the control rod drive mechanisms are discussed in the paragraphs which follow:

#### 2.4.2 Absorber and Drive Mechanisms Outside Inner Core Tank

The first control rod drive mechanism considered was merely a modification of the present mechanisms (see Figures 1.2.1 and 1.5.1). In this design (shown in Figure 2.2.1), the absorber would be located in the reflector region just outside the inner core tank. The absorber would be connected by a shaft to the electromagnet coupling in such a manner that the magnet is always located inside the concrete



shielding of the annular ring and therefore also above the level of the reflector  $D_2O$ . By locating the magnets away from the core in a shielded area above the  $D_2O$  level, the only weakness in the present control rod design has been virtually eliminated. What remains is a control rod mechanism which has proven very reliable over the past eight years of reactor operation. The control rods could be removed for repair, or replacement of the absorber section by unlocking and pulling the entire control rod assembly up through the annular ring and out through the top of the reactor (after first removing the upper shield plug). Approximately ten control rods would be required to surround the core. For a description of the present control rod assembly, see Section 1.5 of this thesis.

### 2.4.3 Drive Mechanism Through Annular Ring

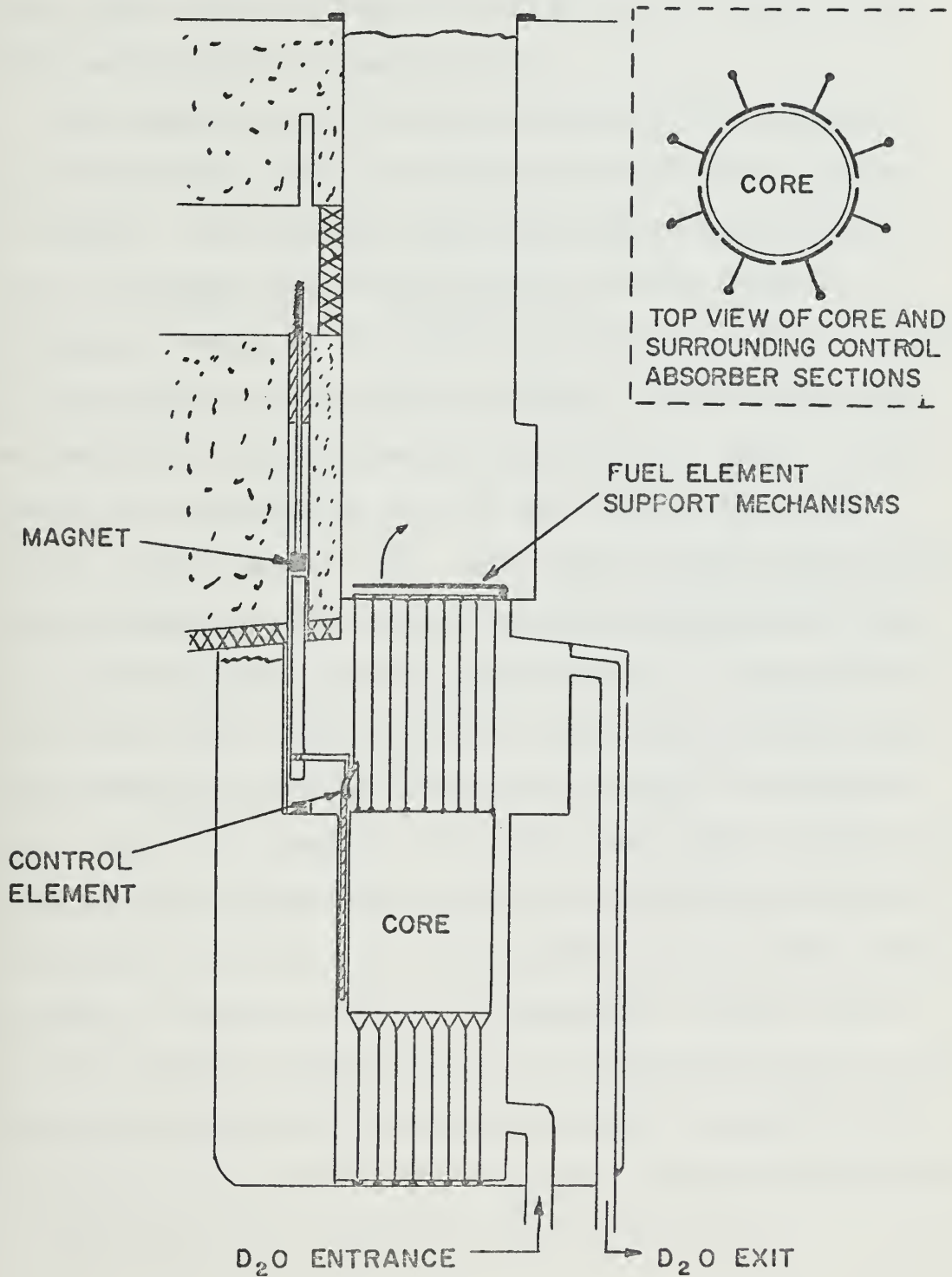
A modification of the control rod mechanism described in Section 2.4.2 was designed in order that the control absorber could be made to completely surround the core in the area immediately adjacent to the fuel elements, inside the inner core tank (see Figure 2.4.3.1). As with the design of the preceding section, the control rod magnet is located up within the shielding area of the annular ring. However, unlike the preceding design, it is necessary to provide a seal in order to prevent  $D_2O$  from leaking up into the magnet area. This seal could take the form of a helium







FIGURE 2.4.3.1  
L-SHAPED DRIVE MECHANISM





pressure in and above the magnet area equal to the water head below the magnet area. It would be necessary to circulate the helium in the magnet area to remove the  $D_2O$  vapor which would otherwise build up in the helium atmosphere surrounding the magnet area.

The control rod drive mechanism would be identical to the mechanism used in the present MITR as far down as the magnet. The assembly below the magnet would consist of an "L"-shaped arm connecting the control absorber to the magnet armature. The absorber section would be pinned to the L-shaped arm so that in order to replace the absorber section it would be merely necessary to unpin the absorber from the arm and lift it out through the necked region of the reactor tank. The elbow of the L-shaped arm would be hinged and contain a dual gear arrangement capable of raising and lowering the "forearm". With the forearm in the fully raised position, the entire control rod drive assembly could be removed out through the reactor top. It can be noted at this point that should either the elbow of the L-shaped arm or the pin connecting the arm to the absorber section fail, the reactor would be shut down. As shown in Figure 2.4.3.1, a spring-type dashpot would slow the absorber support arm as it neared the base of its travel, and aluminum shields would guide the control absorbers as they descend into the core. Eight arced sections of absorber would be used to surround the core.



#### 2.4.4 Drive Mechanisms Above D<sub>2</sub>O Level

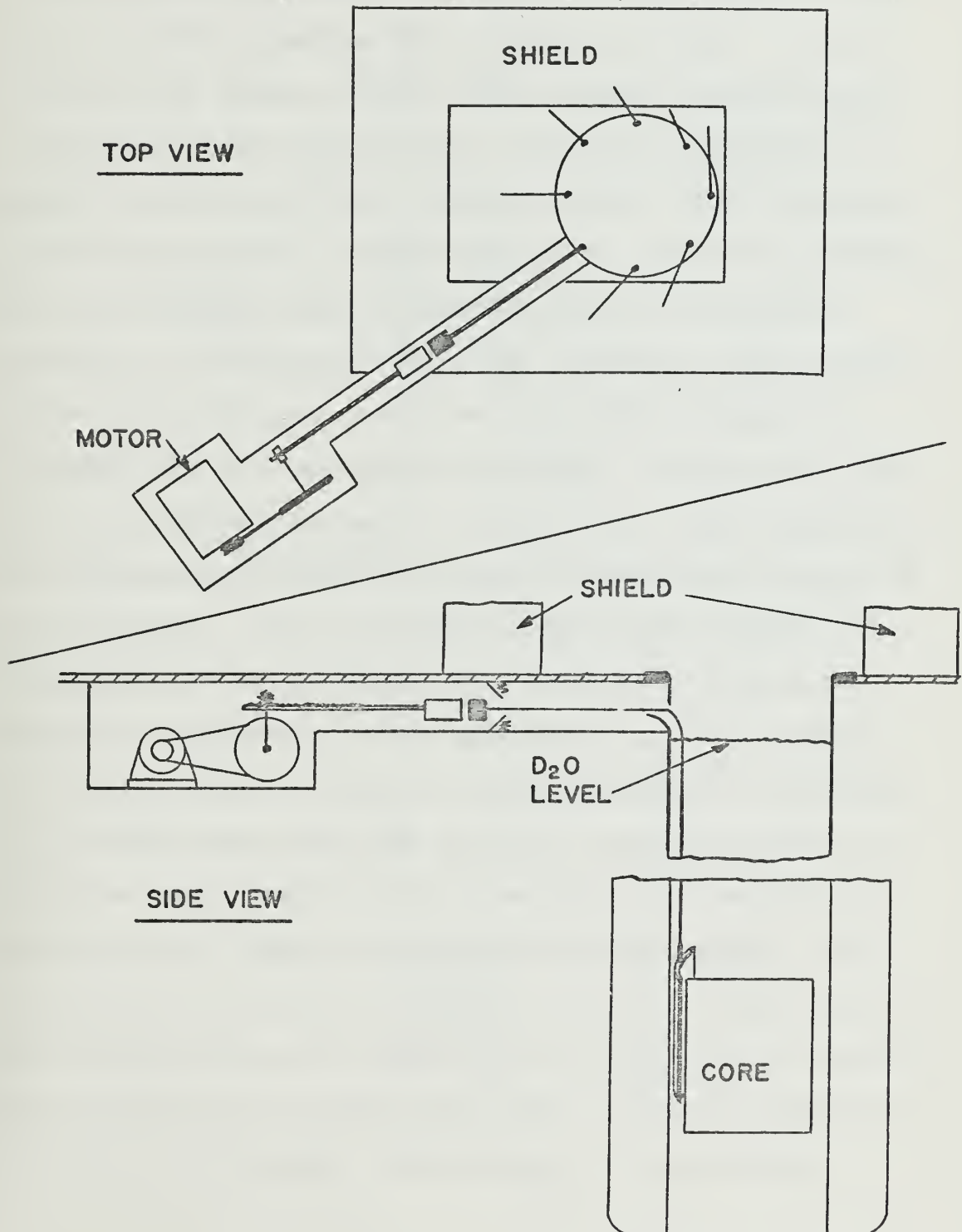
In order to eliminate the complexity involved with having the control rod drive mechanisms penetrate through the annular ring of shielding, designs were proposed which would locate the magnets and drive mechanisms on the reactor top, entirely above the D<sub>2</sub>O level in the tank. Three possible design arrangements were proposed by this author.

The first design proposed called for horizontally placed withdrawal mechanisms installed flush with the reactor top (Figure 2.4.4.1). The control absorber would be attached to the magnet armature by a cable extending vertically to the surface of the D<sub>2</sub>O column, thence horizontally to the position of the armature. Eight curved absorber plates would form a cylindrical shell completely surrounding the core. The entire withdrawal mechanism assembly would be easily accessible through removable covers on the reactor top. The cable withdrawal mechanism provides excellent protection for the magnet, but suffers one serious disadvantage. The absorber will only return to the core by the force of gravity. It cannot be driven into the core, thus ensuring that the absorber is, in fact, completely inserted to its furthest point.

In order to provide for a means whereby the control absorber section could be driven into the core, a design was proposed whereby the withdrawal mechanisms would be



FIGURE 2.4.4.1  
CABLE WITHDRAWAL MECHANISM



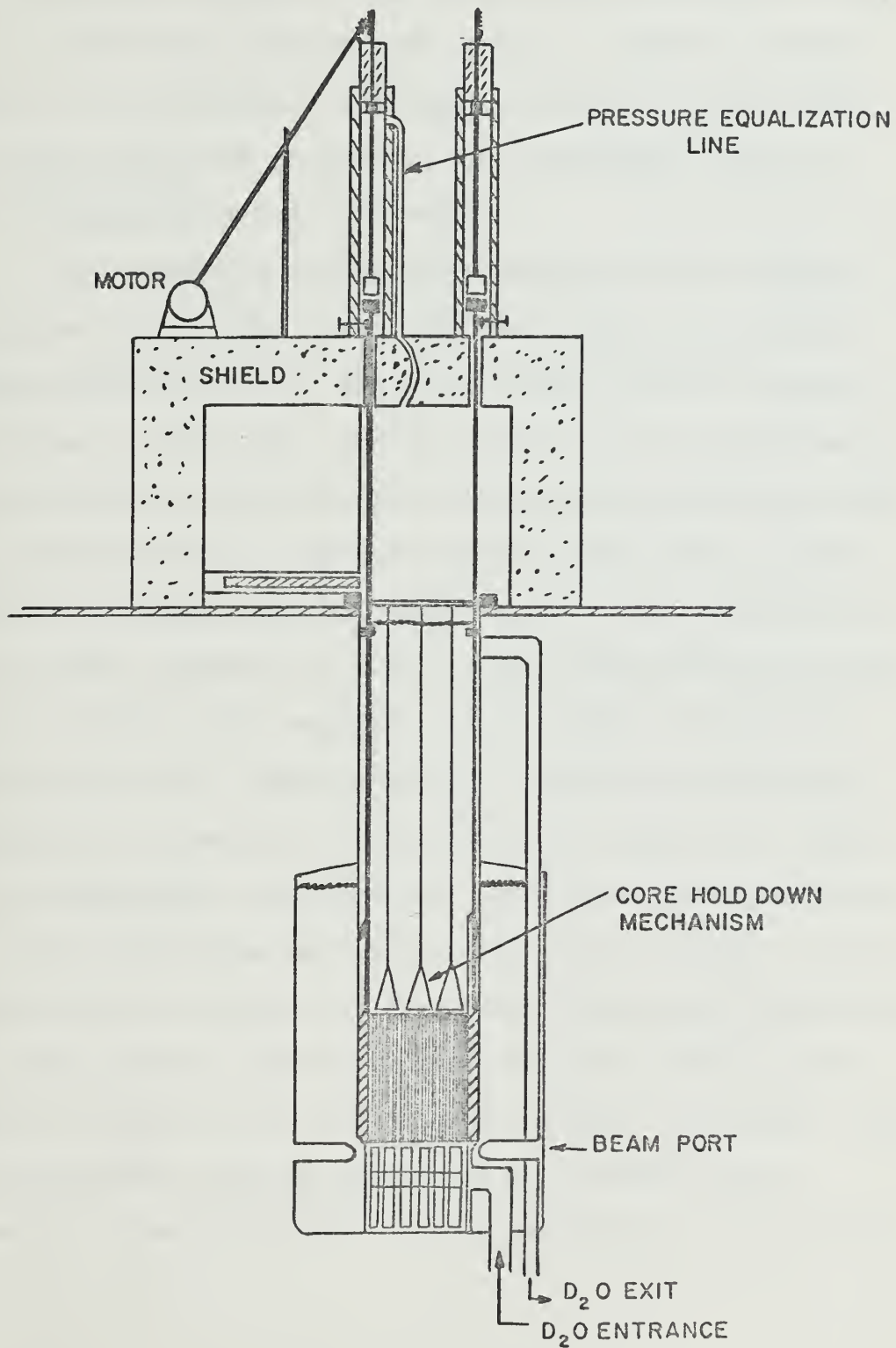




located directly above the absorber sections. The withdrawal mechanisms would be situated vertically atop the reactor top shielding and connected to the absorber sections by solid aluminum rods (Figure 2.4.4.2). As with the previous design, eight arced absorber sections would completely encircle the core. The shaft connecting the magnet armature with the control absorber would be composed of two sections joined together by a screw-in fitting. The two sections could be disconnected at a position parallel to the reactor top, thus allowing a cover shield to be slid into place over the  $D_2O$  column during fuel flipping and fuel changing evolutions. A key at the base of the withdrawal mechanism housing and a gear just below the armature would mate to allow the upper rod section to be unscrewed. The penetrations through the reactor top shielding for the aluminum rods would have to provide adequate clearance so as to guarantee that the aluminum rod would always be free to travel through the shielding. A pressure equalizing line would be required in order to equalize the pressure of the area below the reactor top shielding with that in the area above the magnet. The equalizing line would be required to have a cross sectional area greater than the cross sectional area of the clearance surrounding the aluminum rod as the rod passes through the reactor top shielding. The purpose of the pressure



FIGURE 2.4.4.2  
WITHDRAWAL MECHANISMS ABOVE SHIELDING



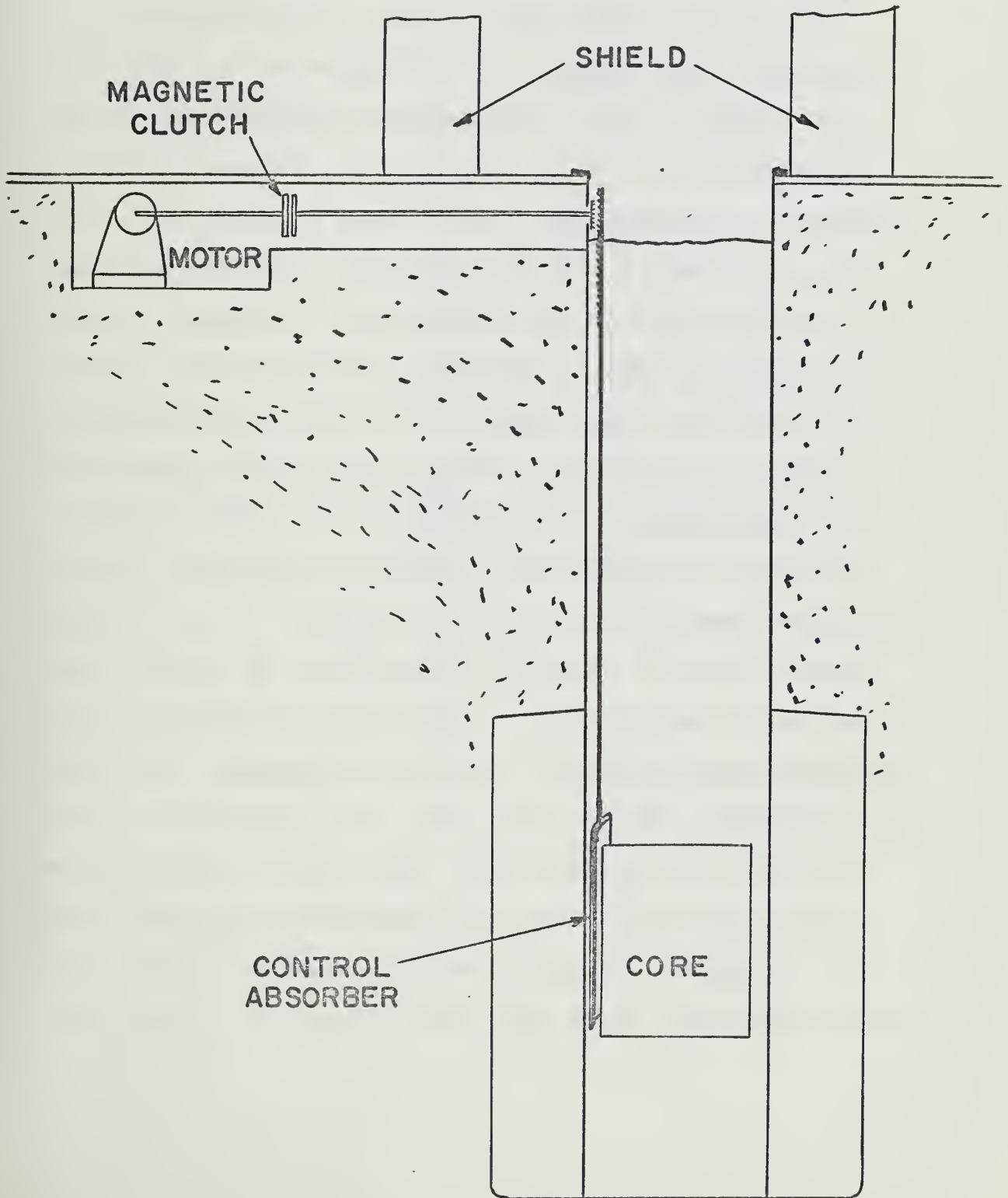


equalizing line would be to ensure that a sudden increase in reactor pressure would not exert itself on the bottom of the magnet armature, thus using the armature as a piston to drive the control rods upward. With the entire control rod withdrawal mechanism located on top of the shielded refueling enclosure, all components would be readily available for maintenance.

A third design alternative proposed would employ features of both the above designs. Vertical aluminum shafts would lead from the eight arced control absorber sections to just above the  $D_2O$  level in the necked tank. A horizontal shaft would be coupled to the vertical shaft by matching gears. The horizontal shaft would in turn lead to a magnetic clutch and thence to the control rod drive motor (Figure 2.4.4.3). Upon interruption of electrical current, the magnetic clutch would release the horizontal shaft, thus allowing it to turn freely and allowing the absorber to drop down into the core. With this arrangement, the absorber could also be driven into the core should the need arise for such a feature. It is a requirement that all of the gears connecting the horizontal and vertical control rod shafts turn freely at all times in order to be effective in a scram condition. Such a requirement could be presented as a design flaw. However, it was felt that the probability of two or more



# MAGNETIC CLUTCH WITHDRAWAL MECHANISM







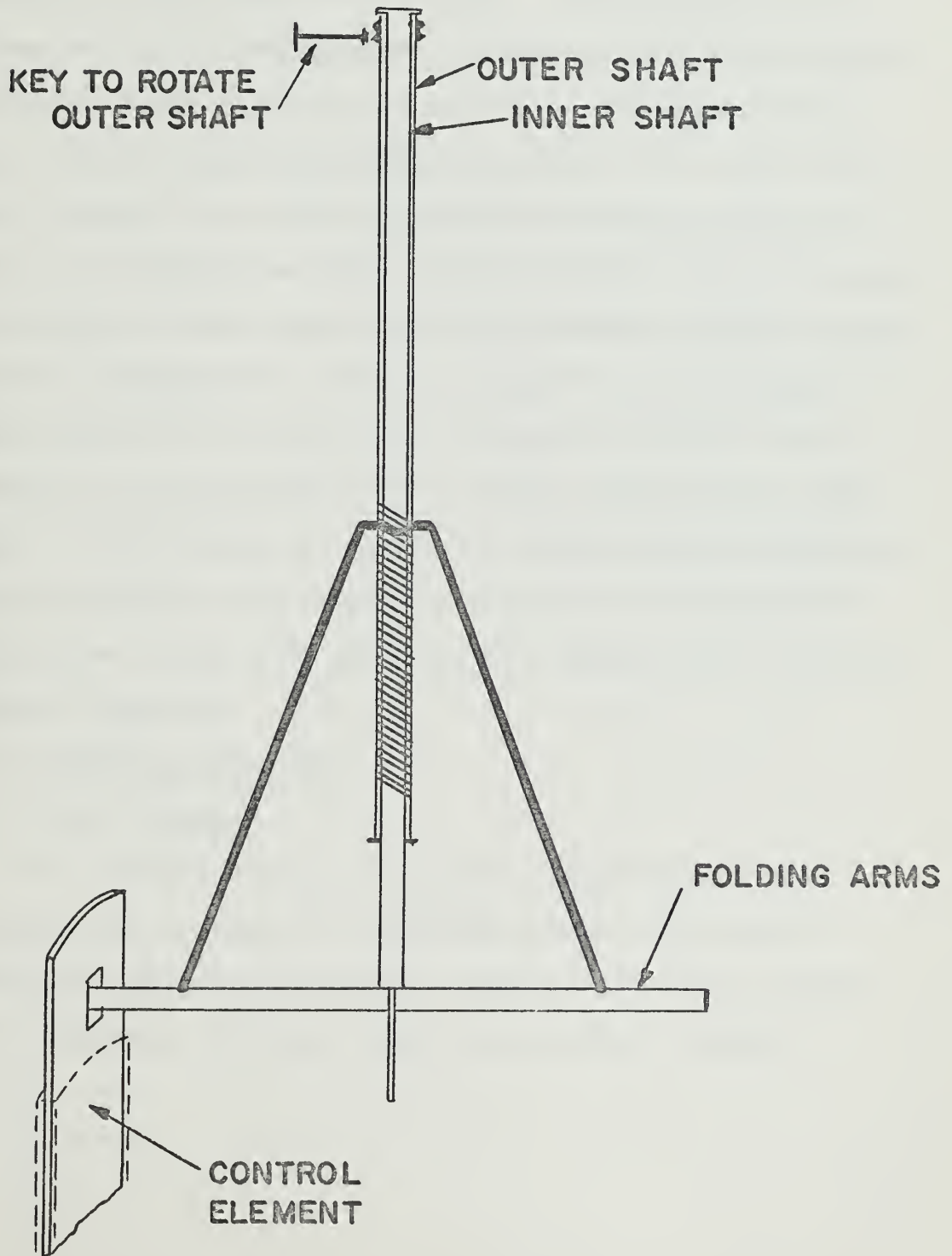
gear couplings jamming simultaneously was so small as to be nearly nonexistent. Any one of the eight control absorbers would be sufficient to shut down the reactor.

#### 2.4.5 Drive Mechanisms for Inner Control Elements

In reviewing the safety requirements for the High Flux MITR, it was decided by Dr. Thompson that sufficient control must exist to maintain the core in a subcritical condition, even if the core were to be filled with light water. In order to satisfy this requirement, Dr. Thompson suggested that the core should contain an inner ring of control elements. The necessity for an incore ring of control elements posed a considerable design problem. A mechanism which would not interfere with the removal or replacement of any fuel element, yet would provide for reliable control of the inner absorber elements was required. The design proposed by this author is shown in Figure 2.4.5.1. The inner control rod withdrawal mechanism would consist of two concentric shafts. The inner shaft would be attached at its base to four pivoted support bars capable of swinging up or down. The support bars would in turn be connected to the outer shaft by four aluminum rods, each pivoted at either end. The connection to the outer shaft would be accomplished by a clamp-type collar which would ride on threaded grooves cut onto a portion of the outer shaft. By rotating the outer shaft, the collar could



INNER CONTROL ELEMENT  
DRIVE MECHANISM





be caused to move upward or downward, thus raising or lowering the support bars. In their lowered (vertical) position the support bars would occupy an area above the center of the core no larger than the area of the cryostat planned for the center of the core. Consequently, the mechanism would not hinder the removal of any fuel element. In their raised (horizontal) position, the support bars would engage slots in the upper section of the inner control elements. The entire mechanism would be raised in order to withdraw the inner control elements from the core. (It should be noted that the inner absorber elements would require followers in order to prevent the flux peaking which would occur if  $D_2O$  were allowed to fill the space vacated by the absorber as the control elements are withdrawn.) The withdrawal mechanism would utilize a magnetic coupling and be constructed identical to the withdrawal mechanisms for each of the absorber sections for the outer control elements.

## 2.5 Refueling Mechanism

### 2.5.1 General

The initial design concept for refueling and fuel flipping was to employ a refueling flask with a self-contained flipping mechanism. However, after the concept of a permanent, enclosed refueling and fuel flipping



facility to be located directly above the core tank on the reactor top was proposed by Mr. Barnett, a new area for design was created. This author set about the task of developing a refueling and fuel flipping scheme which could be used in such an enclosure. In the process, two quite similar designs were developed, each of which is described below.

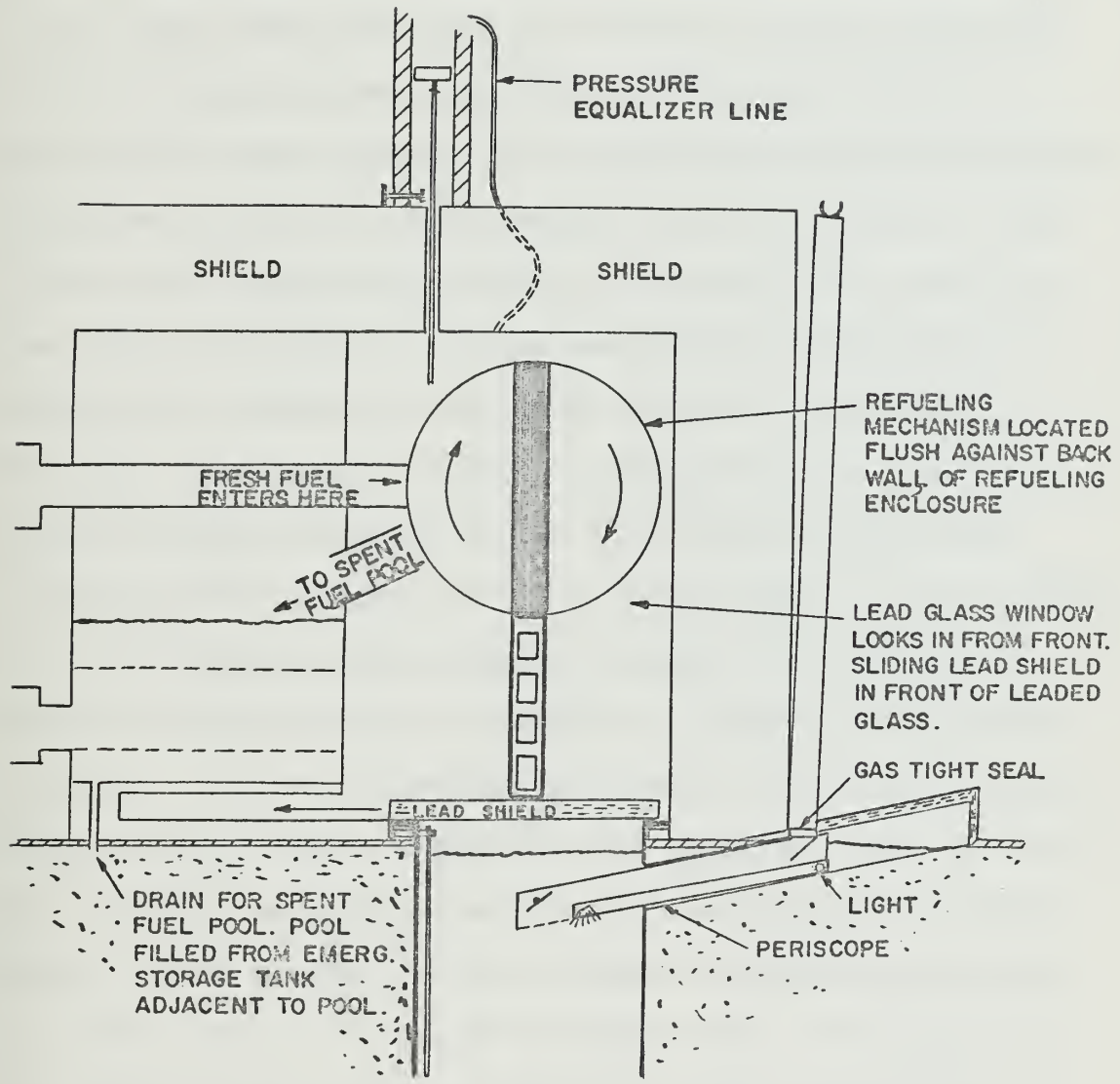
### 2.5.2 Fuel Flipper Above Core Tank

In order to provide a means of rotating a fuel element end for end a rotating table was designed to be mounted vertically against a side wall of the refueling enclosure. On the rotating table would be a bracket designed to accept a fuel element. Directly below the rotating table would be another bracket designed to accept the lower adapter unit of the fuel element. To one side of the  $D_2O$  column would be a horizontal shute through which fresh fuel would enter, and a downward sloping shute through which spent fuel would be discharged into a small  $D_2O$  filled spent fuel pool. A leaded glass window would be provided in the side wall opposite the rotating table in order to provide an operator with visual access to the refueling cavity during refueling or flipping operations. A refueling/fuel flipping sequence would proceed somewhat as follows (assuming control rod drives to be located atop the refueling enclosure): A fuel grabbing tool would be inserted into the reactor tank from the reactor top, latch onto the desired fuel element, and





FIGURE 2.5.2.1  
FUEL FLIPPER MECHANISM





pull it up into the refueling enclosure. Meanwhile the control rod drive shafts would be disconnected at the surface of the  $D_2O$  and the upper portion of the drive shaft withdrawn into the withdrawal mechanism housing. A 2 in. thick lead shield would next be slid into position above the  $D_2O$  column. The lead shield would serve to prevent the fuel element from falling back into the reactor core area should it accidentally become unlatched. (The lead shield would also assist in isolating the refueling enclosure from the core while performing maintenance on any of the refueling or control rod drive mechanisms.) With the lead cover in place, a clamping tool would be inserted through the side of the refueling enclosure and clamp the fuel element to the rotating table. Once secure, the tool used to raise the fuel element out of the core would be disconnected and removed. Another tool would be inserted into the refueling enclosure to pull out the pins connecting the fuel element to its adapter. Once the pins are pulled, the adapter would be allowed to drop down two inches, thus giving the fuel element sufficient clearance to rotate away. If the fuel element were to be replaced, the table would rotate to align the fuel element with the chute to the spent fuel pool, the element would be discharged, and table rotated to receive a new fuel element from the horizontal chute. If the fuel element were to be



flipped, the table would simply be rotated  $180^{\circ}$ . The remainder of the refueling/flipping operation would be the reverse of the above. The lower adapter would be raised and attached to the fuel element, the fuel retraction/loading tool attached to the fuel element, the fuel element and fuel element adapter clamps removed, the lead shield cover removed from the tank top, the control rod drive shafts reconnected, and the fuel element lowered into its respective position in the core.

After allowing a spent fuel element sufficient time to cool (radiation wise), the spent fuel pool would be drained and the fuel element removed through a plug in the refueling enclosure shielding, and thence taken to the main spent fuel pool in the reactor building basement.

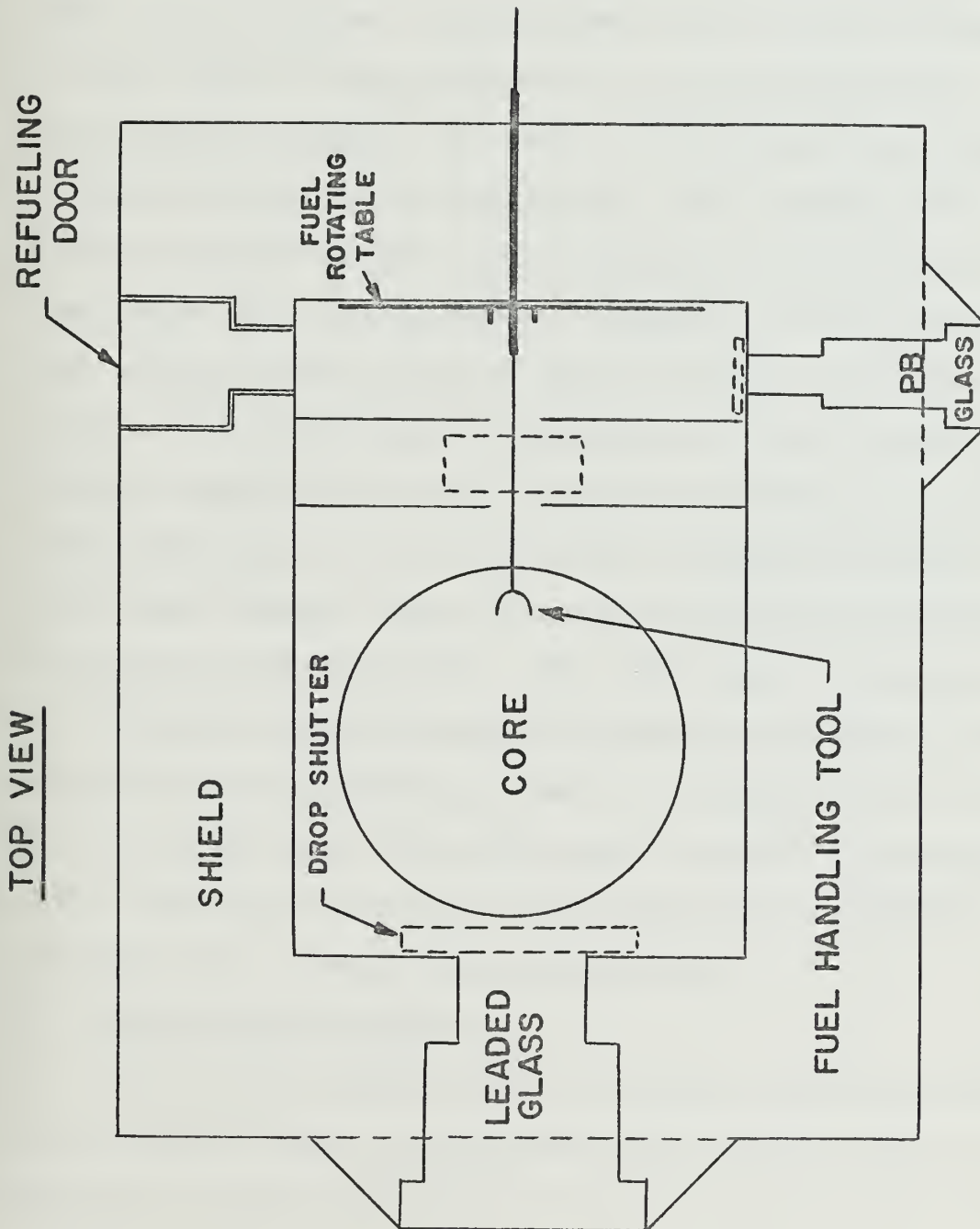
### 2.5.3 Fuel Flipper Away from Core Tank Top

In order to remove the fuel flipping operation from the area directly above the core, a modification to the design of the preceding paragraph was proposed. This design is shown in Figure 2.5.3.1. The purpose in removing the mechanisms involved in fuel flipping/refueling from the area immediately above the core to an area which could be isolated from the space directly above the core was to produce a design whereby maintenance could be performed on the fuel flipping/refueling mechanisms while the reactor was operating at full power. In this manner it was



FIGURE 2.5.3.1

FUEL FLIPPER MECHANISM —  
ALTERNATE APPROACH







anticipated that reactor down time necessitated by maintenance and repairs could be minimized.

The rotating table would be separated from the area above the core tank by a 6 in. lead shielding wall. A removable lead shutter in the center of the shielding wall would raise to allow a fuel element and its lower adapter to pass from the core tank area to the rotating table. The fuel element clamping tool would extend through the center of the shaft of the rotating table. The clamping tool for the fuel element adapter would penetrate the shielding wall just below the rotating table. Instead of being discharged into a small spent fuel pool on the reactor top, spent fuel would be removed through a refueling door into a small fuel element transport flask and transported directly to the large spent fuel pool in the reactor building basement. Fresh fuel elements would also enter the refueling enclosure through the refueling door. Two leaded glass windows would be provided to enable visual observation and control of the entire refueling/flipping process. One window would be in the wall adjacent to the  $D_2O$  column, facing the rotating table. The other would be in the enclosure containing the rotating table, facing the refueling door.

## 2.6 Underwater Periscope

While visual access to the refueling enclosure would be provided by one or more leaded glass windows placed in the walls of the refueling enclosure, it is also desirable



that a means be provided for looking down into the core itself. Being able to see the core would be a necessity during refueling operations, and in addition would be valuable for instructional purposes. It would be possible to locate a leaded glass window in the upper corner of the refueling enclosure, angled downward in such a manner as to allow one to observe the core. However, with such an arrangement one would not get a clear view of the core as a result of attempting to look through a gas-liquid interface at the core tank surface. During reactor operation, the liquid ( $D_2O$ ) surface would be turbulent due to the rapid circulation of the coolant. The turbulence alone would hamper vision, but in addition it is necessary to shine a light down into the coolant tank in order to see the core. Some of this light would be reflected back from the coolant surface, thus creating what would be the major hindrance to clear observation of the core.

In order to eliminate the difficulties mentioned in the previous paragraph associated with observing the core by way of the refueling enclosure, a retractable periscope was designed. As shown in Figure 2.5.2.1, the periscope is mounted at an angle in such a way that when fully inserted into the core the outside end of the periscope remains above the level of the coolant. In this manner the connection between the periscope and the vertical viewing tube is



not required to span a liquid interface. When retracted, the tip of the periscope would be flush with the edge of the coolant tank wall, thereby eliminating any interference to the insertion or removal of components in the area of the periscope. Although the entire core would be visible when looking through the periscope, the mirror which extends into the tank would be able to pivot in order that one might scan for some distance up the sides of the core tank wall. The periscope would have its own self-contained light source. The light source would be located at the base of the periscope, well removed from the intense radiation area, and project its light onto the core via a mirror near the periscope tip. One would look into the periscope through a vertical viewing tube which would extend to a height of 4 ft. above the periscope.



## Chapter 3

## SHIELDING CALCULATIONS

3.1 General

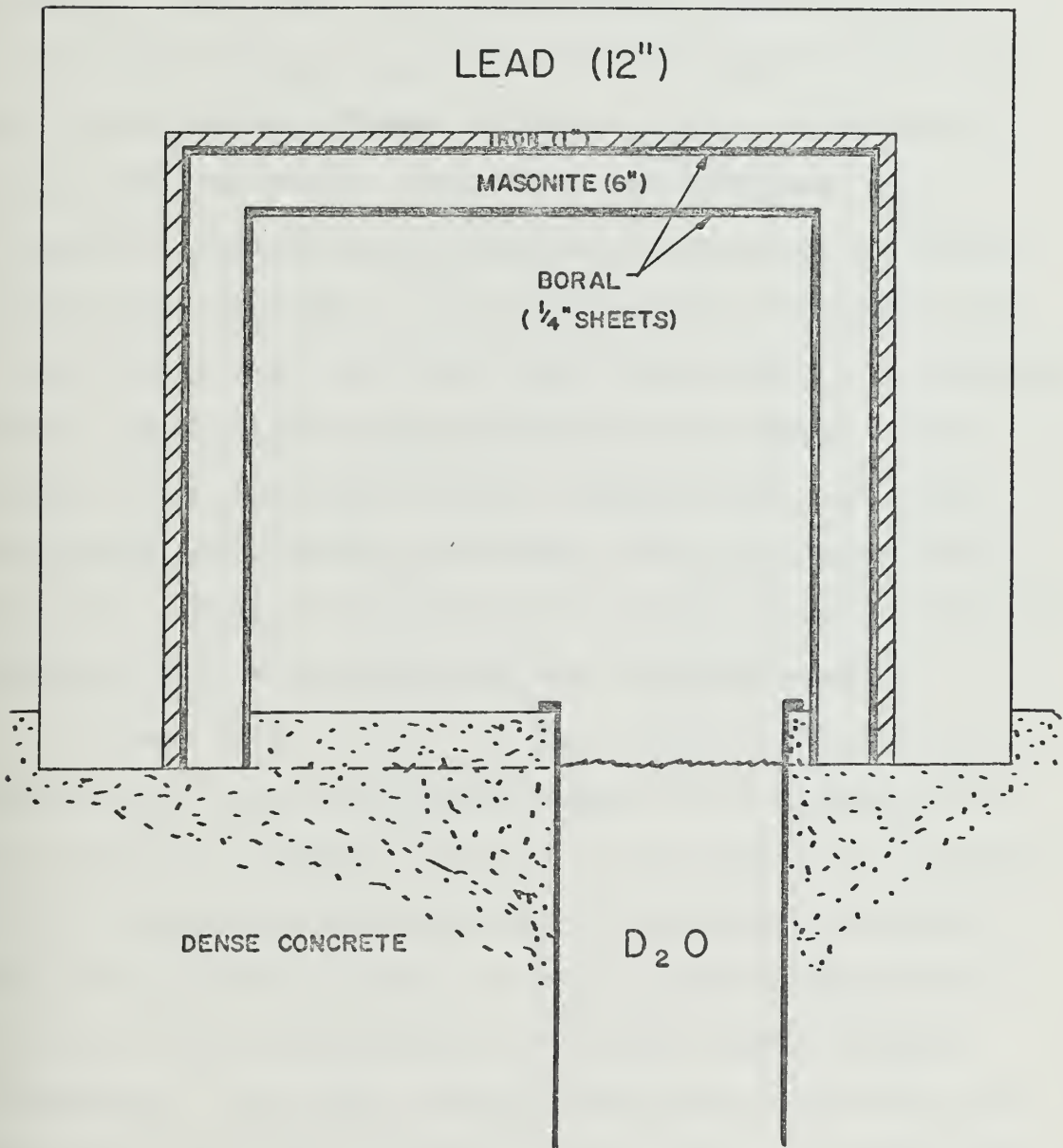
The reactor top shielding design and supporting calculations were originally done for the phase one reactor design. This chapter will first present, therefore, the shielding design and calculational work done for a  $D_2O$  moderated, cooled, and reflected core in some detail. When the core moderator and coolant were changed to light water, a new set of shielding calculations was required. Since the method and reasoning employed in the phase two calculations was exactly the same as that employed for the phase one calculations, phase two calculations will not be reported in detail, but rather a summary of required shielding and calculated dose rates will be given in Sections 3.7-3.9.

In phase one, based on the assumption that the reactor top shielding design would consist of an enclosure similar to that shown in Figure 3.1.1, it was necessary to determine both the composition and thickness of the shielding which would be required. As the calculations of this chapter will show, no major shielding problems were encountered. Such was not known in the early stages of the design project, however. It was anticipated that shielding requirements during reactor operation might be dictated,





FIGURE 3.1.1  
REACTOR TOP SHIELDING ENCLOSURE





not by the radiation being emitted from the core but by the radiation dose due to gamma emission from  $N^{16}$  decay or the gamma emission accompanying the formation of  $H^3$  in the necked region of the core tank, to mention but one example. While the calculations which follow serve to justify the chosen composition and thickness of the reactor top shielding (shown in Figure 3.1.1), it should be noted that the shield composition and thickness were originally determined by successive iterations of exactly similar calculations. It is for the sake of brevity and clarity that only the final set of calculations is presented here. No shielding calculations were performed in the radial direction since neither reactor power nor radial shielding will undergo any change from the present MITR. In fact, radial attenuation will be improved since the core boundary will be further from the shielding walls.

It was required that the  $D_2O$  column combined with the shielding of the refueling enclosure be so designed as to be capable of reducing the dose on the reactor top sufficiently such that a worker working full time in this area would not receive a dose in excess of the maximum whole body dose limit established by the U.S. Atomic Energy Commission. The Atomic Energy Commission's maximum allowable whole body dose levels are 100 mrem per 40 hour week or 2.5 mrem per hour (6). However, it is desirable that



the shielding be capable of reducing the dose anywhere on the reactor top to well below these maximums. The present MITR was designed so that the dose on the reactor top would be less than 1 mrem per hour at 5 megawatts (8). Similarly, the goal in the design of the shielding for the High Flux MITR was to reduce the dose anywhere on the reactor top to less than 1.0 mrem per hour when the reactor is at a power of 5 Mw.

The dose rates during both shutdown and operational conditions were determined. For the shutdown condition, the sources of radiation of most concern are those resulting from material activation and fission product decay. For the operational condition one must consider, in addition to the shutdown sources, the dose due to gamma ray production in fission, fission neutrons, photoneutrons, gamma rays from the decay of  $N^{16}$ , and gamma rays from the production of tritium.

## 3.2 Calculational Methods

### 3.2.1 General

The calculational methods followed in performing the shielding calculations for the High Flux MITR were the same as those used in the design of the shield for the Omega West Reactor at Los Alamos Scientific Laboratory (see reference 7). This same procedure was also used in obtaining the initial shielding estimates for the present



MITR. Radiation measurements recorded subsequent to the completion of the Omega West Reactor tend to bear out the validity of using the calculational methods employed in the shield design. As an example, the calculated dose rate due to gamma rays through the lid on the reactor top was 114 mrem/hr. The measured value was 107 mrem/hr.

### 3.2.2 Gamma Ray Attenuation

The sources of gamma rays in the High Flux MITR will be treated as point sources. The assumption of a point source has been estimated by Gage to produce results which are at most 20% greater than those obtained from calculations performed utilizing a distributed source. The error involved in assuming a point source of radiation is compensated for an adjustment to the radiation source strength, as discussed in a later section of this chapter. The equation for the attenuation of gamma rays from a point source is:

$$\phi = \frac{S}{4\pi R^2} FBe^{-\mu x} \gamma's/cm^2\text{-sec} , \quad (3.2.2.1)$$

where, S = source strength ( $\gamma's/\text{sec}$ ),

R = distance from the source (cm),

F = fraction of gamma rays in energy range of interest,

$\mu$  = linear absorption coefficient ( $\text{cm}^{-1}$ ),





$x$  = thickness of absorbing material (cm), and

$B$  = buildup factor

The Omega West Reactor shielding calculations were done in terms of decade lengths rather than in terms of the linear absorption coefficient, and so decade lengths will be used here also. A decade length is defined as that thickness of material,  $d$ , required to reduce the flux by a factor of ten. Decade length is determined as follows:

$$1/10 = e^{-\mu d}$$

$$d = 2.3/\mu \text{ cm} = 0.0754/\mu \text{ ft.}$$

The shield thickness in decade lengths,  $D$ , is defined as  $D = \frac{x}{d}$ , where  $x$  is again defined as the thickness of absorbing material. It is also necessary to convert the buildup factor,  $B$ , from its normally listed value in terms of e-folding lengths to decade lengths. Buildup factors in terms of decade lengths for water, iron, and lead were taken from reference (7) and are given in Figures 3.2.2.1, 3.2.2.2, and 3.2.2.3 respectively. It should be noted that Figure 3.2.2.1 is for light water. However, since gamma ray attenuation is most strongly dependent on the atomic number of the absorber, and  $H_2O$  and  $D_2O$  both have the same total  $Z$  value, Figure 3.2.2.1 is assumed to be applicable to heavy water as well. This is a conservative



FIGURE 3.2.2.1

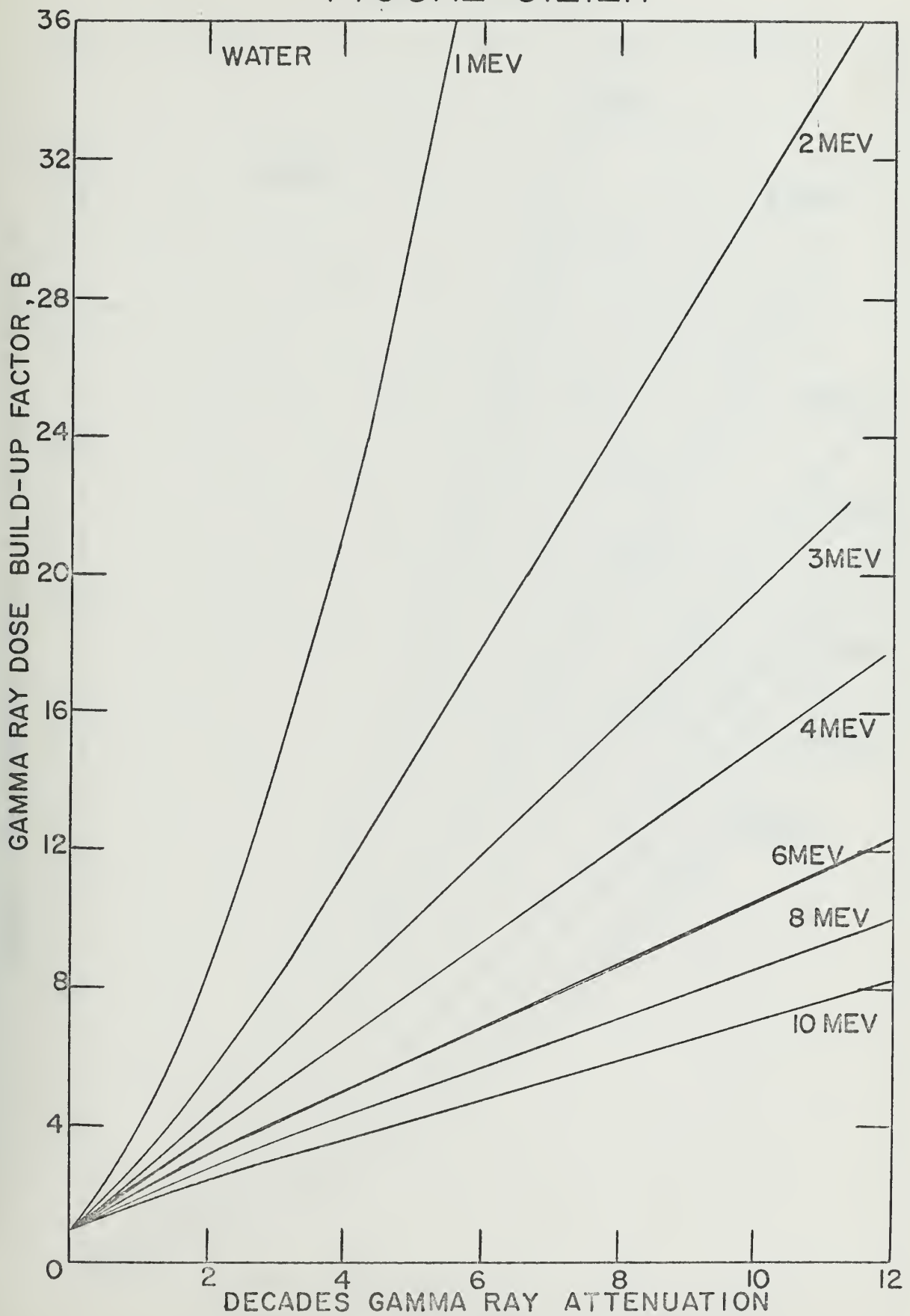




FIGURE 3.2.2.2

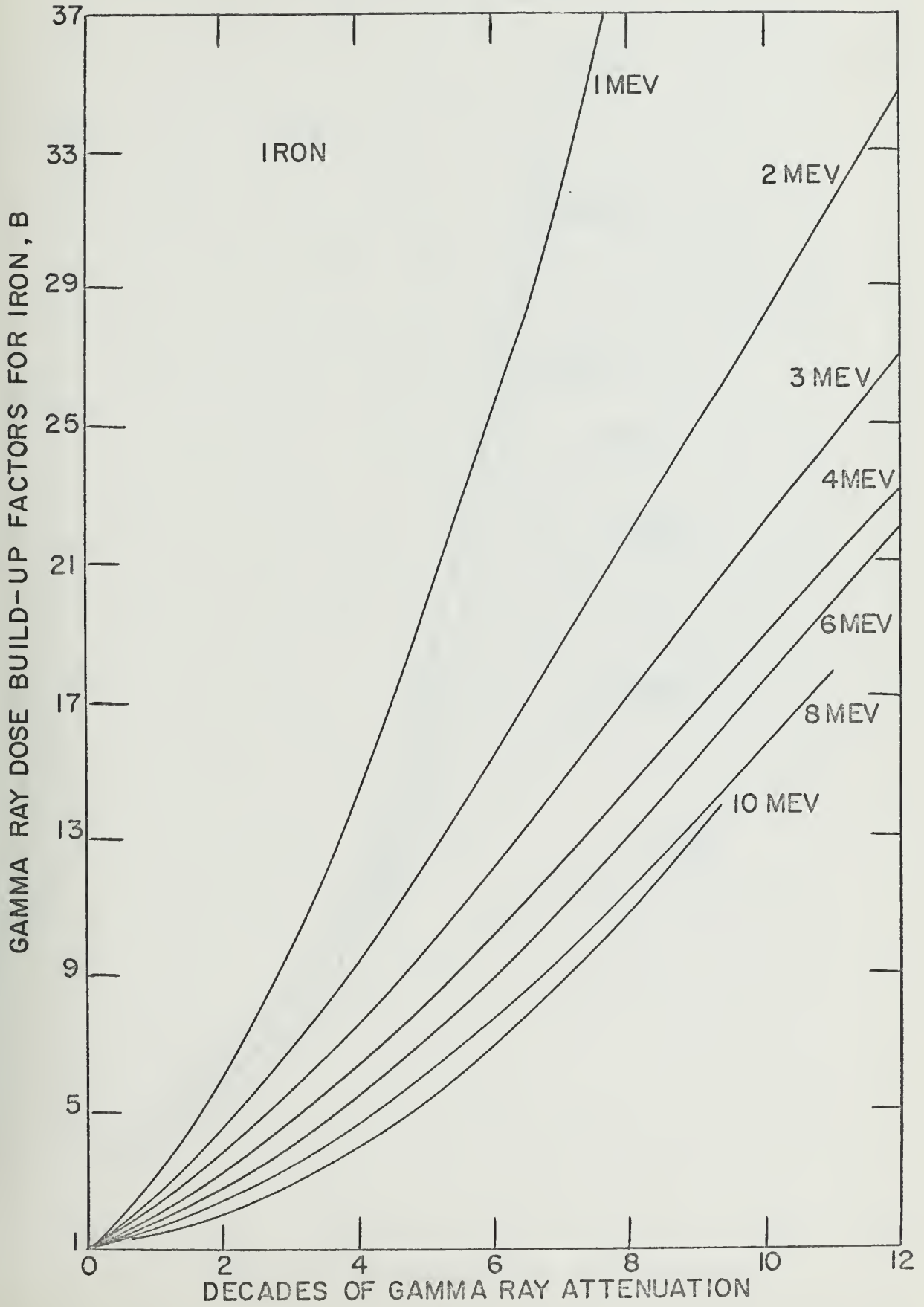
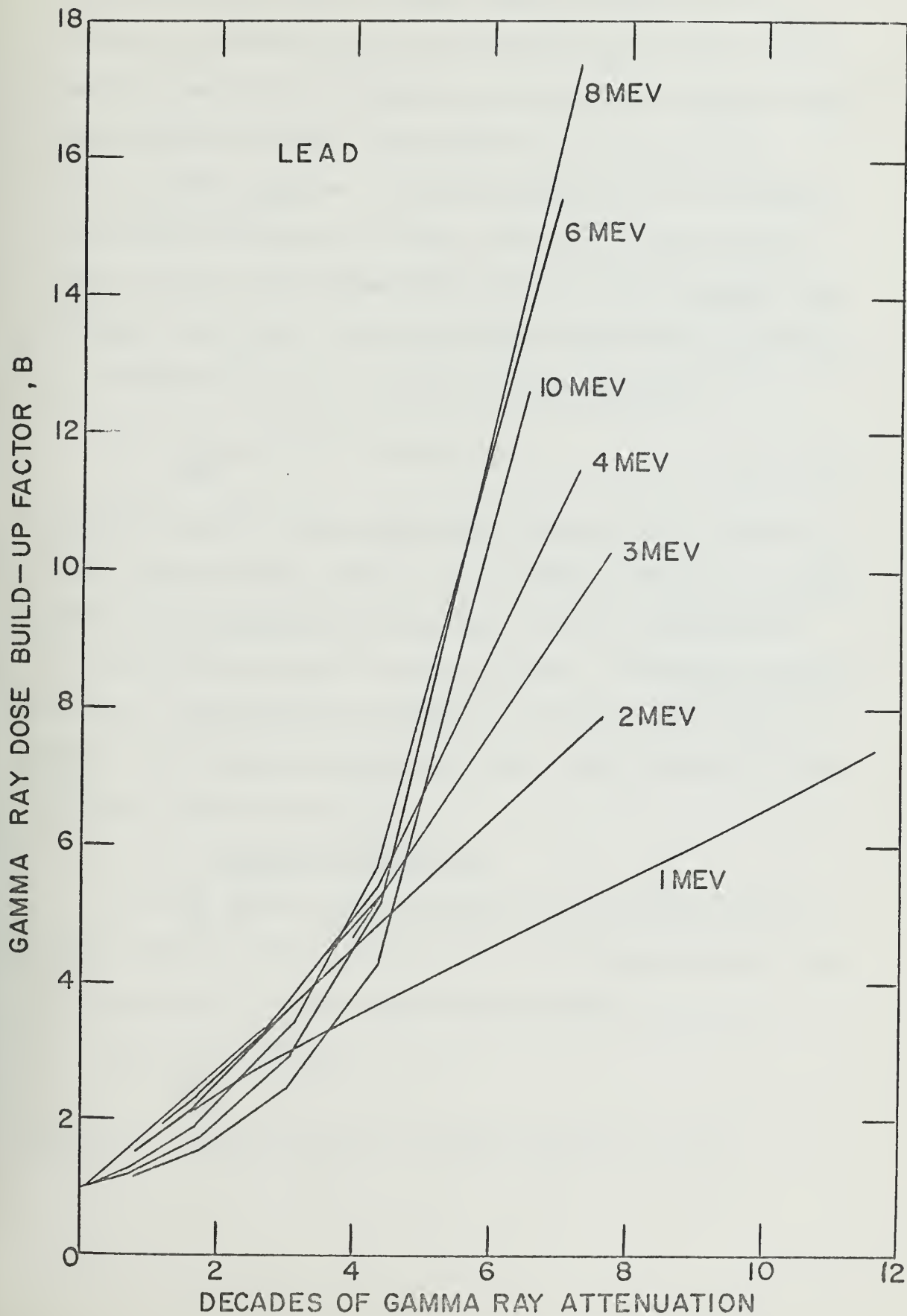




FIGURE 3.2.2.3







assumption since  $D_2O$  is about 10% more dense than  $H_2O$ . It should also be noted that buildup factors for heavy concrete were not available, so the buildup factors for iron (Figure 3.2.2.2) were used in the calculations later in this chapter. This substitution is reasonable since heavy concrete is about 75% iron. The result is conservative from a shielding point of view because the buildup factor for iron is greater than that of concrete.

Equation 3.2.2.1 can now be re-written as

$$\phi = \frac{S}{4\pi R^2} \text{FB } 10^{-D} \text{ } \gamma' \text{s/cm}^2\text{-sec} . \quad (3.2.2.2)$$

In applying this flux attenuation equation to a shield consisting of many layers, it is assumed that the buildup factor for the shield is the sum, and not the product, of the buildup factors for each layer. Although this may not be a conservative assumption, it has been shown by Gage to be much more accurate than if the product of the buildup factors were used.

### 3.2.3 Neutron Attenuation

As with gamma rays, neutrons will be considered as being emitted from a point source. The equation for the attenuation of fission spectrum neutrons is:

$$\phi = \frac{N}{4\pi R^2} e^{-R/\lambda} n$$

where  $N$  = neutron source strength (neutrons/sec),



$R$  = distance from the source (cm), and

$\lambda_n$  = relaxation length for removal of neutrons (cm).

A decade length for the attenuation of fast neutrons is determined as follows:

$$\frac{1}{10} = e^{-d/\lambda_r}$$

$$d = 2.3 \lambda_r (\text{cm}) = 0.0754 \lambda_r (\text{ft}).$$

Relaxation lengths and decade lengths for some shielding materials of interest were taken from reference (7) and are given in Table 3.2.3.1.

The attenuation of thermal neutrons is determined by means of diffusion theory. The applicable diffusion equation for thermal neutrons from an infinite plane source in an infinite homogeneous media is:

$$\phi = \phi_0 \frac{Le^{-x/L}}{2D} \text{ neutrons/cm}^2\text{-sec} , \quad (3.2.3.2)$$

where  $L$  = diffusion length (cm),

$D$  = diffusion coefficient (cm),

$x$  = thickness of attenuating material (cm), and

$\phi_0$  = thermal neutron flux on the core side of the shield

### 3.3 Shielding Calculations, Normal Operation (Phase I)

#### 3.3.1 Fission Gamma Rays

The primary source of radiation to be shielded against is the gamma rays produced by fissions in the core.



Table 3.2.3.1

Material	Specific Gravity	Microscopic Effective Removal Cross Section, $\sigma_r$ (barns/atom)	Relaxation Length, $\lambda_r$ (cm)	Decade Length, d (ft)
Portland Concrete	2.3	-	11.1	0.836
Brookhaven Concrete	4.3	-	6.3	0.475
Barytes Concrete	3.5	-	8.0	0.603
Water	1.0	2.99	9.98	0.752
Graphite	1.67	0.84	14.2	1.07
Aluminum	2.7	1.2	13.8	1.04
Iron	7.8	2.0	5.90	0.445
Lead	11.3	3.4	8.94	0.673



Assuming 198.22 MEV are released per fission (see Section 4.2), the source strength of the High Flux MITR operating at 5 megawatts would be:

$$(5 \times 10^6 \text{ watts})(3.1 \times 10^{10} \text{ fissions/watt-sec}) = 1.55 \times 10^{17} \text{ fissions/sec.}$$

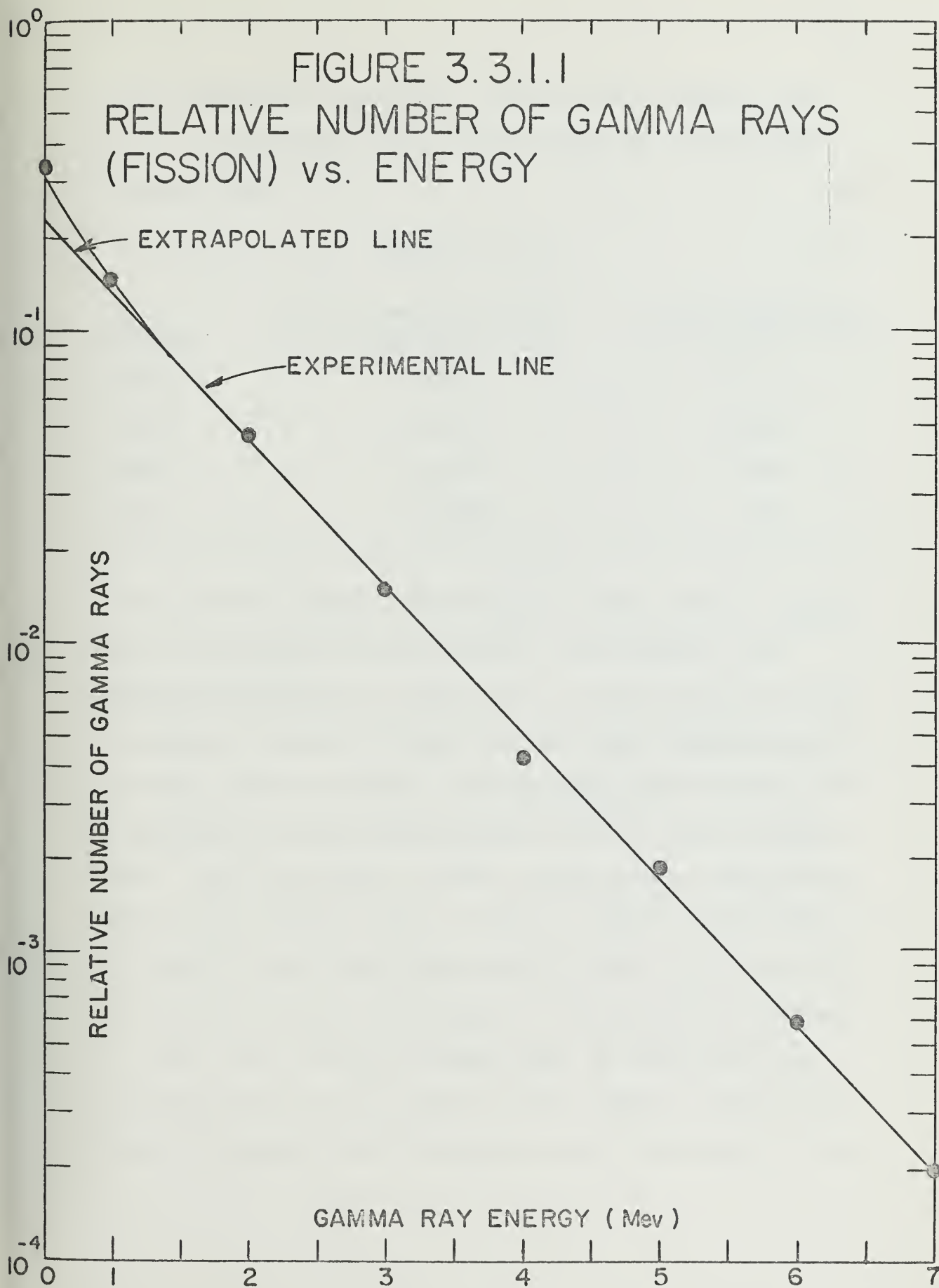
With each fission event there are, on the average, 7.5 gamma rays emitted from the fissioning nucleus (9). Thus, the source strength of the fission gamma rays from a core operating at 5 megawatts is:

$$(1.55 \times 10^{17} \frac{\text{fissions}}{\text{sec}})(7.5 \frac{\text{gammas}}{\text{fission}}) = 1.17 \times 10^{18} \frac{\text{gammas}}{\text{sec}} .$$

Figure 3.3.1.1, taken from reference (7), shows the relative number of fission gamma rays versus energy. The straight line extrapolation shown in the figure was used to calculate the percentage of gamma rays above a given energy. The results obtained are conservative. Gage has shown that for energies above 1.5 MeV the extrapolated line predicts about 30 percent more gamma rays than exist. The excess in the fraction of gamma rays predicted above an energy E in the range 0 to 1.5 MeV decreases from 30% to zero as E decreases from 1.5 to 0 MeV. It is assumed that the fission gamma rays can be lumped into three energy groups. Table 3.3.1.1 gives the calculated fractions above each of the three energy groups assumed using









the straight line analysis, and also the assumed fraction at each energy that will be used in the shielding calculations.

Table 3.3.1.1

<u>Energy</u>	<u>Calculated Percentage Above E</u>	<u>Assumed Percentage at E</u>
0 MeV	100%	
1 MeV	33.4%	100%
3 MeV	3.7%	33%
6 MeV	0.14%	3%

Note that the assumed percentage of gamma rays at  $E_{\text{calc}}$  have been greatly overestimated. For example, the assumed percentage of gamma rays at 6 MeV has been overestimated by about a factor of 20. This overestimation of gamma source strength was the method used by Gage to compensate for the nonconservative point source assumption. Gage performed a twelve energy group calculation with energy groups from 0-12 MeV in order to check the accuracy of the three energy group model. For the water and concrete radial shielding of the Omega West Reactor, he found that the three group model as described above was conservative by a factor of 5. Similar conservatism could be expected for the D<sub>2</sub>O and lead shielding of the



## High Flux MITR.

The height of the coolant above the core top is 8 ft. Since the gamma source is being treated as a point source of radiation, it is necessary to add to this the additional 1 ft. which exists between the center of the core and the core top. Hence, the total thickness of D<sub>2</sub>O to be considered is 9 ft. The helium-filled space between the D<sub>2</sub>O surface and the bottom of the shielding enclosure is 4-1/2 ft. in height. The refueling enclosure top shielding block consists of 6 in. of masonite sandwiched between two 1/4 in. sheets of boral (neglected for gamma ray calculations), 1 in. of steel used for support, and 1 ft. of lead. (Note: D<sub>2</sub>O cooling coils will loop through the lead and masonite-boral sandwich.)

For clarity Eq. 3.2.2.2 may be rewritten as:

$$\phi = \frac{SF}{4\pi(R_D+R_H+R_{US})^2} (B_D+B_I+B_L) 10^{-(D_D+D_I+D_L)}, \quad (3.3.1.1)$$

where the subscripts D, H, I, and US refer to D<sub>2</sub>O, Helium, Iron, Lead, and Upper Shield respectively. For calculational purposes, the helium gap will be treated as void. Decades of attenuation and buildup factors for materials of interest as a function of energy are given in Table 3.3.1.1.



Table 3.3.1.1.1

Shield Material	Shield Thickness (ft)	Gamma Energy (MeV)	Decade Length (ft)	Decades of Attenuation	Buildup Factor
D <sub>2</sub> O	9.0	1	0.973	9.25	72*
		3	1.738	5.20	9.2
		6	2.505	3.59	4.3
Steel	0.083	1	0.164	0.51	2
		3	0.273	0.30	1.3
		6	0.322	0.26	1.2
Lead	1.0	1	0.0946	11.11	7.1
		3	0.161	6.21	8.0
		6	0.149	6.71	14.6

\*Obtained by linear interpolation





Substituting into Eq. 3.3.1.1 for the dose rate due to 6 MeV core gamma rays on the reactor top directly above the core yields:

$$\phi_6 = \frac{(1.17 \times 10^{18})(0.03)}{4\pi (9+5+.083+1) \times 30.48^2} (4.3+1.2+14.6) 10^{-(3.59+.26+6.71)}$$

$$\phi_6 = 7.41 \text{ gamma rays/cm}^2\text{-sec.}$$

For 6 MeV gammas  $157.7 \frac{\text{gamma rays}}{\text{cm}^2\text{-sec}} = 1 \text{ mrem/hr.}$ , the conversion from gamma rays/cm<sup>2</sup>-sec to mrem/hr having been obtained from page 7-66 of reference (9). The R.B.E. for gamma rays was taken to be 1. Therefore,  $\phi_6 = 0.047 \text{ mrem/hr.}$

Following exactly the same procedure for the 3 MeV group,

$$\phi_3 = 5.42 \text{ gammas/cm}^2\text{-sec} = 0.021 \text{ mrem/hr,}$$

and for the 1 MeV group,

$$\phi_1 = 4.4 \times 10^{-8} \text{ gammas/cm}^2\text{-sec} = 7.6 \times 10^{-11} \text{ mrem/hr.}$$

Summing the above calculated dose rates, the total dose rate on the reactor top directly above the core due to fission gamma rays is calculated to be:

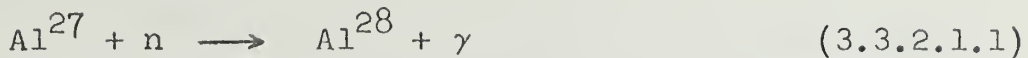
$$\phi = 0.047 \times 0.021 + 7.6 \times 10^{-11} = 0.068 \text{ mrem/hr.}$$

### 3.3.2 Material Activation

#### 3.3.2.1 General

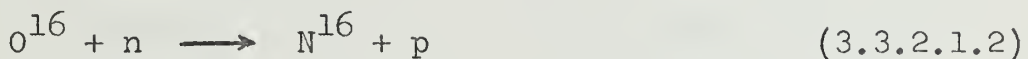
The primary reaction which must be considered is the thermal neutron activation of the aluminum contained in the core and surrounding structure. The reaction of concern is:





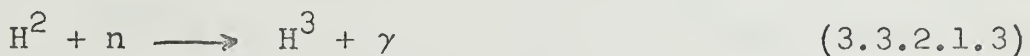
The thermal cross section for this reaction is 0.215 barns.  $\text{Al}^{28}$  emits an average of two prompt gamma rays for each neutron captured by  $\text{Al}^{27}$  (10).

Also of concern from a shielding point of view are the gamma rays released in the decay of Nitrogen 16, which is formed in the reaction:



Although the activation cross section averaged over the entire fission spectrum for this section is only 20 micro barns, it is usually the most important reaction associated with the reactor coolant. Nitrogen 16 decays with a half-life of 7.35 sec., liberating gamma rays of energy 6.1 MeV (75%) or 7.1 MeV (7%), plus one prompt proton which has no significance from a shielding point of view. (11)

The final material activation reaction to be considered in this section will be the formation of tritium, the reaction of interest being:



The thermal neutron cross section for this reaction is 0.57 milli-barns, and the resulting prompt gamma has an energy of approximately 6.26 MeV (9).

### 3.3.2.2 $\text{Al}^{27} (n, \gamma) \text{Al}^{28}$

In order to determine the dose rate on the reactor top due to the decay of  $\text{Al}^{28}$ , the reactor core area was



divided into three regions as shown by the dotted lines in Figure 3.3.2.2.1. Gamma rays born due to the decay of  $\text{Al}^{28}$  were assumed to be point sources located at the center of each of the three regions. The volume of aluminum in each of the three regions was determined based on a best estimate of ultimate core and supporting structure composition:

Region I	$V = 5500 \text{ cm}^3$
Region II	$V = 56,700 \text{ cm}^3$
Region III	$V = 10,100 \text{ cm}^3$

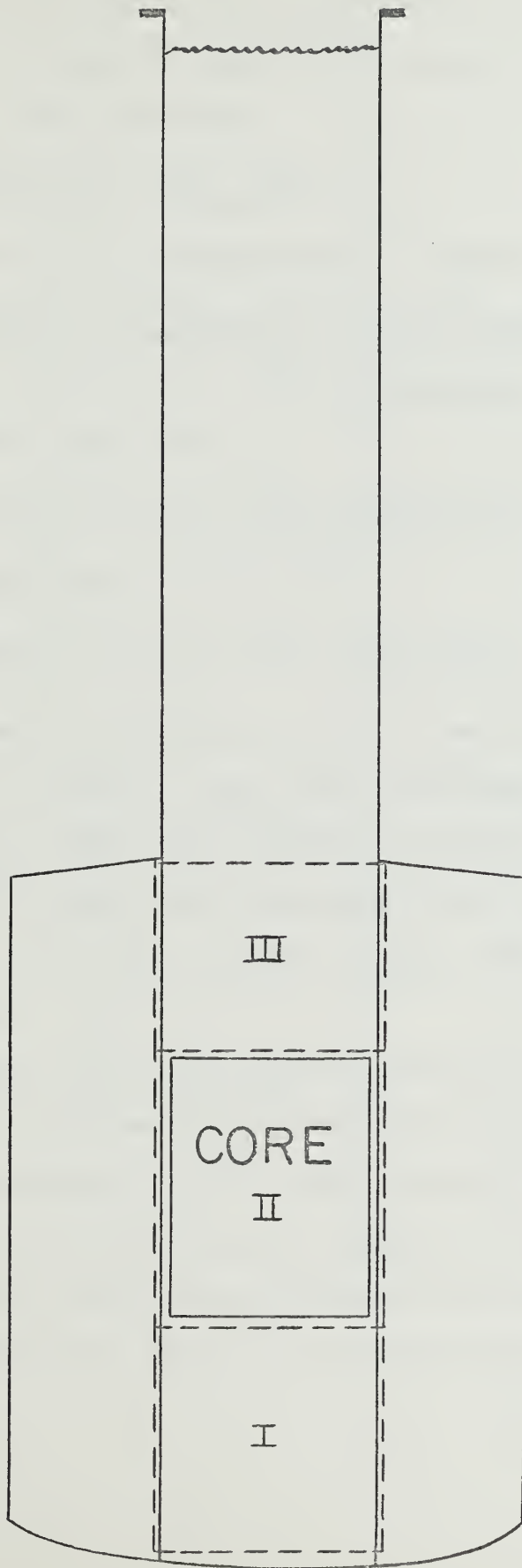
The aluminum volumes by region were based on assumed aluminum volume percents within each region of 2% for region I above the core, 43% for region II in the core, and 4.3% for region III below the core, plus a 1/8 in. thick 100% aluminum tank wall forming the boundary of each region. The average thermal flux in each of the three regions was conservatively estimated based on the preliminary core physics calculations described in Chapter 4 of this thesis:

Region I	$\phi = 10^{12} \text{ neutrons/cm}^2\text{-sec}$
Region II	$\phi = 5 \times 10^{13} \text{ neutrons/cm}^2\text{-sec}$
Region III	$\phi = 10^{14} \text{ neutrons/cm}^2\text{-sec}$

Only the thermal neutron induced flux is considered here due to the rapid decrease in the reaction cross section of aluminum at higher energies. The activation cross section for 0.2 MeV neutrons is down to about  $10^{-3}$  barns,



REGIONS FOR  $Al^{27}$ ,  $(n, \gamma) Al^{28}$  CALCULATIONS







for example. Assuming an irradiation of infinite duration, the number of neutron captures per second in  $\text{Al}^{27}$  is described by the equation:

$$\text{Captures/sec} = N \sigma_{\text{act}} \phi V_{\text{Al}} \quad (3.3.2.2.1)$$

Proceeding with the calculation for region I,

$$\begin{aligned} N \sigma_{\text{act}} \phi V_{\text{Al}} &= (0.06023)(0.215)(10^{12})(5500) = \\ &7.12 \times 10^{12} \text{ captures/sec.} \end{aligned}$$

Similarly for region II,

$$N \sigma_{\text{act}} \phi V_{\text{Al}} = 3.66 \times 10^{16} \text{ captures/sec,}$$

and for region III,

$$N \sigma_{\text{act}} \phi V_{\text{Al}} = 1.31 \times 10^{16} \text{ captures/sec.}$$

Information for Table 3.3.2.2.1 was taken from references (7) and (9), and lists the number and mean energy of the gamma rays emitted per thermal neutron capture in  $\text{Al}^{27}$ , along with the gamma flux to dose rate conversion and the decade lengths in  $\text{D}_2\text{O}$ , iron and lead respectively.

Equation 3.3.1.1 was used to obtain the dose rate on the reactor top directly above the core due to the thermal neutron activation of  $\text{Al}^{27}$ . Table 3.3.2.2.2 lists the input data not previously given required to solve the equation, and the resulting dose rate on the reactor top due to gammas from each region. The calculational procedure was



Table 3.3.2.2.1

Mean Energy (MeV)	Gamma Rays per Neutron Capture	Gamma Rays per mrem/hr	Decade Length in D <sub>2</sub> O (ft)	Decade Length in Iron (ft)	Decade Length in Lead (ft)
2	1.67*	340	1.38	0.226	0.146
4	0.77	210	2.00	0.290	0.158
6	0.21	158	2.50	0.315	0.153
8	0.35	128	2.83	0.325	0.145

\*Includes one 1.8 MeV gamma (taken as 2MeV for calculations) which is given off in the decay of Al<sup>28</sup>.



Table 3.3.2.2.2

Region	Mean Energy	D <sub>D2O</sub>	D <sub>iron</sub>	D <sub>lead</sub>	B <sub>D2O</sub>	B <sub>iron</sub>	B <sub>lead</sub>	neutrons/cm <sup>2</sup> -sec	$\phi$	Dose Rate mrem/hr
I	2	4.96	0.37	6.85	14.5	1.7	7.1	9.3 x 10 <sup>-5</sup>		2.7 x 10 <sup>-7</sup>
	4	3.42	0.29	6.32	5.8	1.3	10.2	4.5 x 10 <sup>-3</sup>		2.1 x 10 <sup>-5</sup>
	6	2.77	0.26	6.53	3.8	1.1	13.9	3.9 x 10 <sup>-3</sup>		2.5 x 10 <sup>-5</sup>
	8	2.42	0.25	6.89	3.3	1.1	15.9	7.1 x 10 <sup>-3</sup>		5.5 x 10 <sup>-5</sup>
II	2	6.47	0.37	6.85	21.0	1.7	7.1	1.4 x 10 <sup>-2</sup>		4.2 x 10 <sup>-5</sup>
	4	4.45	0.29	6.32	9.0	1.3	10.2	1.9		9.0 x 10 <sup>-3</sup>
	6	3.59	0.26	6.53	4.6	1.1	13.9	2.37		1.5 x 10 <sup>-3</sup>
	8	3.18	0.25	6.89	3.6	1.1	15.9	4.89		3.8 x 10 <sup>-2</sup>
III	2	8.23	0.37	6.85	25.1	1.7	7.1	7.7 x 10 <sup>-5</sup>		2.3 x 10 <sup>-7</sup>
	4	5.68	0.29	6.32	8.8	1.3	10.2	3.1 x 10 <sup>-2</sup>		1.5 x 10 <sup>-4</sup>
	6	4.56	0.26	6.53	5.5	1.1	13.9	7.3 x 10 <sup>-2</sup>		4.6 x 10 <sup>-4</sup>
	8	4.01	0.25	6.89	4.2	1.1	15.9	2.0 x 10 <sup>-1</sup>		1.6 x 10 <sup>-3</sup>



exactly the same as the sample calculation done in Section 3.3.1, and so is not repeated here. Summing the dose rates listed in Table 3.3.2.1.1 gives a total dose rate on the reactor top due to the thermal neutron activation of  $\text{Al}^{27}$  to be 0.064 mrem/hr.

### 3.3.2.3 $\text{O}^{16} (n,p) \text{N}^{16}$

Although the decay of  $\text{N}^{16}$  often results in high radiation levels around exit coolant piping, there is normally little reason to consider the  $\text{O}^{16} (n,p) \text{N}^{16}$  reaction for purposes of reactor vessel shielding due to the small activation cross section of  $\text{N}^{16}$ . However, the fluid flow scheme for the High Flux MITR calls for the coolant to circulate up to very near the top of the necked portion of the  $\text{D}_2\text{O}$  tank. It is for this reason that the dose rate due to  $\text{N}^{16}$  decay is calculated.

The threshold energy for the  $\text{O}^{16} (n,p) \text{N}^{16}$  reaction is very high (approximately 10 MeV). Therefore, it is reasonable to assume that  $\text{N}^{16}$  may only be formed on the first collision of a fission neutron. The probability of a fission neutron interacting to form  $\text{N}^{16}$  is simply the ratio of the cross section for the formation of  $\text{N}^{16}$  to the total removal cross section seen by a fission neutron. Table 1.1 in Rockwell gives the effective removal cross section for fission neutrons in  $\text{D}_2\text{O}$  as 2.8 barns per molecule (12). The probability that an  $\text{O}^{16} (n,p) \text{N}^{16}$  reaction occurs in





the first collision of a neutron is therefore,

$$P(n,p) = \frac{20 \times 10^{-6}}{2.8} = 7.15 \times 10^{-6}$$

where it has been assumed that all neutrons have that first collision with either  $H^2$  or  $O^{16}$ . This assumption is conservative and leads to a slight overestimation of  $P(n,p)$ . The rate of production of  $N^{16}$  in the entire reactor becomes:

$$\begin{aligned} R &= \# \text{ fission neutrons} \times P(n,p) \\ \# \text{ fission neutrons} &= (5 \times 10^6 \text{ watts}) \\ &\quad (3.14 \times 10^{10} \frac{\text{fissions}}{\text{watt-sec}}) (2.48 \frac{\text{neutrons}}{\text{fission}}) \\ \# \text{ fission neutrons} &= 3.9 \times 10 \text{ neutrons/sec.} \end{aligned}$$

$R = (3.9 \times 10^{17})(7.15 \times 10^{-6}) = 2.78 \times 10^{12}$  activations/sec. It is now assumed that all the  $N^{16}$  atoms formed are formed in the  $D_2O$  which circulates up through the necked core tank. This assumption is conservative because some  $N^{16}$  will be formed in the reflector  $D_2O$ , but the  $N^{16}$  formed in the reflector will make a negligible contribution to the dose rate on the reactor top. The volume of the  $D_2O$  in the inner coolant tank is about 225 gallons. Therefore, at 1850 gallons per minute the coolant takes 7.5 seconds to pass from the inner tank inlet to exit. The external system  $D_2O$  volume is approximately 475 gallons. Therefore, at 1850 gallons per minute the total cycle time for the  $D_2O$



is approximately 23.3 seconds. Now assuming  $N^{16}$  to be formed uniformly throughout the height of the inner core tank (an obviously conservative assumption since few fission neutrons will undergo their first collisions near the top of the necked  $D_2O$  column), and taking the activity of the entire volume of  $D_2O$  in the inner tank to be that of the coolant as it exits the upper portion of the inner tank, (again a very conservative assumption) the saturation activity due to  $N^{16}$  decay becomes:

$$A_{sat} = R \frac{1 - e^{-\lambda t_c}}{1 - e^{-\lambda t_t}} \quad (3.3.2.2.1)$$

where  $\lambda$  = decay constant for  $N^{16} = \frac{.693}{7.35} \text{ sec} = .0943 \text{ sec}$   
 $t_c$  = irradiation time in the inner core tank  
 $t_t$  = total cycle time

$$A_{sat} = (2.68 \times 10^{12}) \frac{1 - e^{-(0.0943)(7.5)}}{1 - e^{-(0.0943)(23.3)}}$$

$A_{sat} = 1.59 \times 10^{12}$  disintegrations/sec. From Section 3.3.2.1, it is recalled that  $N^{16}$  decays by emission of either a 6.1 MeV gamma (75% of the time) or a 7.1 MeV gamma (7% of the time). It is assumed in the following calculations that  $N^{16}$  always decays by emission of a 6 MeV gamma. (This assumption is conservative since in lead a 6 MeV gamma is more penetrating than a 7 MeV gamma.) The dose rate on the reactor top due to  $N^{16}$  decay is



calculated assuming the total saturated activity to be a point source located at the surface of the D<sub>2</sub>O column.

Again substituting into Eq. 3.3.1.1:

$$\phi = \frac{(1.59 \times 10^{12})(1.0)}{4\pi (5 + .083 + 1)30.48^2} (1.2 + 14.6) 10^{-(.26 + 6.71)}$$

$$\phi = 6.32 \text{ } \gamma\text{'s/cm}^2\text{-sec .}$$

Therefore,

$$\text{Dose Rate} = 0.04 \text{ mrem/hr.}$$

The dose rate due to N<sup>16</sup> decay calculated above is ultra-conservative from a shielding point of view. (The dose is overestimated by about a factor of 10.) The primary purpose of the calculations was to show that even using overly conservative assumptions the decay of N<sup>16</sup> would not make a dominant contribution to the total dose rate on the reactor top.

#### 3.3.2.4 H<sup>2</sup> (n, γ) H<sup>3</sup>

Since only thermal neutrons are important in the formation of tritium, the gamma ray flux resulting from tritium formation will vary, as a function of position in the core, directly with the thermal neutron flux. Tritium decays by emission of a beta particle, which, although very significant from a health physics standpoint should it be ingested into the body, is insignificant for purposes



or reactor top shielding calculations. For calculational purposes, the  $D_2O$  volume was divided into four regions as shown in Figure 3.3.2.4.1, and the gamma rays from each region were assumed to originate from point sources located as shown in the figure. An average thermal flux was assumed for regions I and II based on a conservative interpretation of the results shown in Chapter 4 of this thesis. The average thermal flux in regions III and IV was calculated by considering the necked core tank to be a  $D_2O$  thermal column in which the calculational method to be shown in Section 3.3.4.2 applies.

The number,  $n$ , of gamma rays produced per second in each region due to the formation of tritium is given by:

$$n = N \sigma_{act} \bar{\phi} V_{D_2O} , \quad (3.3.2.4.1)$$

where  $N$  = deuterium atom density =  $0.06646 \times 10^{24}$  atoms/cm<sup>3</sup>,

$\sigma_{act}$  = activation cross section for  $H^2(n, \gamma)H^3$  reaction =  
 $0.57 \times 10^{-3}$  barns,

$\bar{\phi}$  = average thermal flux,

$V_{D_2O}$  = coolant volume of interest.





REGIONS FOR  $H^2(n, \gamma) H^3$  CALCULATIONS

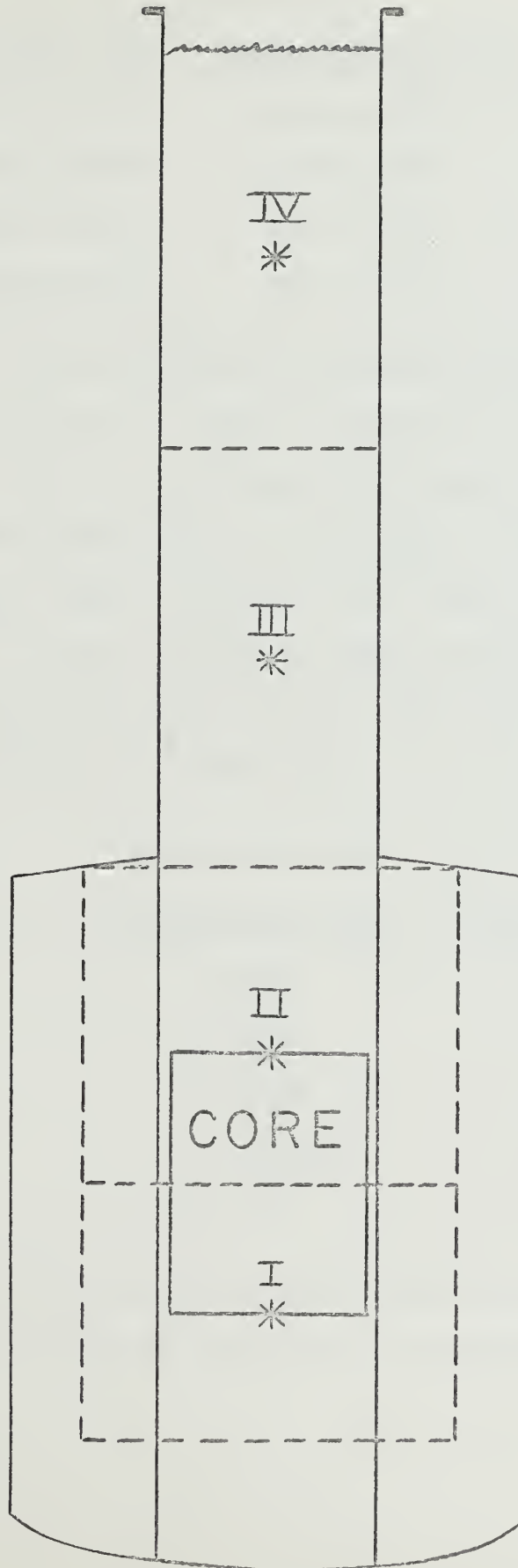




Table 3.3.2.4.1

Region	Volume (cm <sup>3</sup> )	(neutrons/cm <sup>2</sup> -sec)	S(gammas/sec)
I	6.0 x 10 <sup>5</sup>	1.0 x 10 <sup>14</sup>	1.14 x 10 <sup>15</sup>
II	5.4 x 10 <sup>5</sup>	1.0 x 10 <sup>12</sup>	1.02 x 10 <sup>13</sup>
III	1.95 x 10 <sup>5</sup>	1.8 x 10 <sup>10</sup>	6.65 x 10 <sup>10</sup>
IV	1.95 x 10 <sup>5</sup>	5.3 x 10 <sup>6</sup>	1.96 x 10 <sup>7</sup>

Again the calculational procedures outlined in Section 3.3.1 are followed in order to obtain the dose rate on the reactor top due to the H<sup>2</sup> (n,γ) H<sup>3</sup> reaction. Since a 6 MeV gamma is more penetrating in lead than a 7 MeV gamma, the reaction gamma rays are taken to be 6 MeV (a conservative assumption). Table 3.3.2.4.2 lists the results of the calculations for gamma flux and dose rate on the reactor top due to the H<sup>2</sup> (n,γ) H<sup>3</sup> reaction.

Table 3.3.2.4.2

Region	(gammas/cm <sup>2</sup> -sec)	Dose Rate (mrem/hr)
I	0.246	1.56 x 10 <sup>-3</sup>
II	0.026	1.65 x 10 <sup>-4</sup>
III	0.0056	3.54 x 10 <sup>-5</sup>
IV	0.000036	2.30 x 10 <sup>-7</sup>
Total	0.278	1.76 x 10 <sup>-3</sup>

As shown by the above calculation, the dose rate on the reactor top due to tritium formation is negligible.



### 3.3.3 Fission Product Decay

As one might expect, the dose rate due to fission product decay is small compared with the dose rate from prompt fission gammas. An infinite irradiation time is assumed, thereby yielding a dose rate which contains the contribution of both short and long-lived fission products. The results so obtained are conservative since in practice the reactor will operate during the week and be shut down on weekends.

According to Rockwell, the rate of energy emission by gamma rays after an infinite operating time at 5 MW is  $1.14 \times 10^{18}$  MeV per second (12). If the average decay gamma ray energy is taken to be 2 MeV, the decay gamma ray source strength becomes  $5.7 \times 10^{17}$  gammas/sec (13). A point source is assumed at the core center, and the calculational procedure outlined in Section 3.3.1 is once again used. The dose rate on the reactor top due to fission product decay is calculated to be  $4.1 \times 10^{-4}$  mrem/hr.

### 3.3.4 Neutron Attenuation

#### 3.3.4.1 Fast Fission Neutrons

The relation for the attenuation of fission spectrum neutrons is given by Eq. 3.2.3.1, here repeated in slightly different form:

$$Q = \frac{S}{4\pi R^2} e^{-(\Sigma x / \lambda_r)} , \quad (3.3.4.1.1)$$



where  $S$  = neutron source strength (neutrons/sec),

$R$  = distance from the source (cm),

$x$  = thickness of attenuating materials (cm), and

$\lambda_r$  = relaxation length for removal of neutrons (cm).

The relaxation length,  $\lambda_r$ , is calculated by the relation:

$$\lambda_r = \frac{A}{N_a \rho \sigma_r} \text{ (cm) ,} \quad (3.3.4.1.2)$$

where  $\sigma_r$  = microscopic removal cross section (barns/atom),

$N_a$  = Avagardo's number ( $6.04 \times 10^{23}$  molecules/gm-mole),

$\rho$  = density (gms/cm<sup>3</sup>), and

$A$  = molecular weight (gms/gm-mole).

For  $D_2O$ ,

$$\lambda_r = \frac{20.03}{(0.604 \times 10^{24})(1.105)(2.8 \times 10^{-24})} = 10.7 \text{ cm.}$$

The relaxation lengths for lead and iron are given in Table 4.2.3.1 to be 8.94 cm and 5.90 cm respectively.

As calculated in Section 3.3.1 there will be  $1.55 \times 10^{17}$  fissions/second in the High Flux MITR operating at 5 MW. Taking the neutron yield per fission to be 2.47, and considering that one of these neutrons is needed to sustain the chain reaction, there will be a total of  $(1.47)(1.57 \times 10^{17})$   $2.31 \times 10^{17}$  fission neutrons per second available for leakage or for absorption in the various reactor materials.





The conservative approach is to assume that all  $2.31 \times 10^{17}$  neutrons leak from the core.

Substituting into Eq. 3.3.4.1.1, the fast fission neutron flux on the reactor top is calculated:

$$\phi = \frac{(2.31 \times 10^{17})}{4\pi [(9+5+.083+1) \times 30.48]^2} e^{-\left(\frac{9 \times 30.48}{10.7} + \frac{.083 \times 30.48}{5.90} + \frac{1 \times 30.48}{8.94}\right)}$$

$$\phi = 1.69 \times 10^{-2} \text{ neutrons/cm}^2\text{-sec.}$$

From Figure 2.3 of reference (12), the conversion from fission neutron flux to dose rate is taken to be 8.6 neutrons/cm<sup>2</sup>-sec per mrem/hr. Therefore, the dose rate on the reactor top due to fast fission neutrons is calculated to be,  $\frac{1.69 \times 10^{-2}}{8.6} = 1.96 \times 10^{-3}$  mrem/hr. As one might expect, the low fission neutron flux on the reactor top is primarily due to the excellent moderating characteristics of the D<sub>2</sub>O in the necked core tank region. Using the above calculational method, it was found that the fast neutron flux at the coolant surface is only 1.96 neutrons/cm<sup>2</sup>-sec.

Not included in the above calculation is the moderating effect of the masonite. In practice, most of the fast neutrons reaching the masonite are thermalized in the masonite, and subsequently absorbed in the surrounding boral. To neglect the masonite, therefore, yields a conservative result.



### 3.3.4.2 Thermal Neutrons

In order to determine the dose rate on the reactor top due to thermal neutrons, it is first necessary to determine the thermal neutron flux at the surface of the necked coolant tank. This can be done by assuming the necked coolant tank region to be a cylindrical thermal column. The thermal flux at the base of the necked coolant tank is conservatively estimated, based on the results of the flux calculations in Chapter 4 of this thesis, to be  $10^{12}$  neutrons/cm<sup>2</sup>-sec. For the situation of interest here, the applicable relation for the flux as a function of axial position in the necked core tank is:

$$\phi(Z) = \phi_0 e^{-\gamma Z} \quad (3.3.4.2.1)$$

where  $Z$  = axial distance above the necked core tank base (cm),

$$\gamma = \sqrt{\left(\frac{1}{L}\right)^2 + \left(\frac{2.405}{r'}\right)^2} \quad (\text{cm}^{-1}),$$

$L$  = diffusion length = 100 cm in  $D_2O$ ,

$r'$  = extrapolated tank radius =  $r + 0.71 \lambda_{tr}$

$\lambda_{tr}$  = transport mean free path =  $3D$

$D$  = diffusion length = 0.80 cm in  $D_2O$ , and

$r$  = core tank radius = 25.4 cm.

Substituting in numerical values,

$$\gamma = \sqrt{\left(\frac{1}{100}\right)^2 + \left(\frac{2.405}{28.8}\right)^2} = 0.0842 \text{ cm}^{-1}$$

$$\phi(Z) = (10^{12}) e^{-(0.0842)(Z)} \text{ neutrons/cm}^2\text{-sec.}$$



Calculated values of  $\phi(Z)$  are given in the following table:

Table 3.3.4.2.1

Z (cm above base of necked core tank)	(Z) neutrons/cm <sup>2</sup> -sec
48	$1.8 \times 10^{10}$
145	$5.3 \times 10^6$
193 (coolant surface)	$9.6 \times 10^4$

Because lead is a very poor attenuator of thermal neutrons, and because it is desirable to avoid the capture gamma rays which are produced in a  $\text{Fe}^{56} (n, \gamma) \text{Fe}^{57}$  reaction, it was decided to line the interior of the refueling enclosure with boral. A 1/4 in. thick sheet of boral will result in a maximum fractional transmission of thermal neutrons of  $5 \times 10^{-3}$  (14). Consequently, if the refueling enclosure is lined with two 1/4 inch sheets of boral, the thermal neutron flux will be effectively eliminated before entering the iron or lead shielding.

### 3.3.5 Photodisintegration of Deuterium

The threshold energy for the  $\text{H}^2 (\gamma, n) \text{H}^1$  reaction is 2.23 MeV. The reaction cross section increases from zero at the threshold energy to a maximum value of 2.24 millibarns for a gamma energy of 4 MeV. The cross section then decreases to a value of 1.2 millibarns for a 13 MeV gamma (11). For calculational purposes, it will be assumed that all gammas



of energy greater than 2 MeV are capable of initiating the  $(\gamma, n)$  reaction and that the average reaction cross section is 1.5 millibarns.

In order to determine the number of neutrons generated as a function of position in the core, it is necessary to determine the flux of gamma rays above 2 MeV as a function of position in the reactor tank. For this purpose, the tank was again divided into four regions as shown in Figure 3.3.2.3.1. The gamma flux in a given region is that due to gammas born in the region plus that due to gammas entering the region from each of the surrounding regions. Except for fission gammas, the number of gamma rays per region of energy greater than 2 MeV was taken from the results of calculations performed in previous sections of this chapter. Table 3 on page 50 of reference (7) shows that 19.3% of all fission gammas have energies greater than 2 MeV, and so this percentage was used rather than the assumed percentage given in Section 3.3.1. The flux entering a region from each of its three neighbors is calculated using Eq. 3.3.1.1 where the gamma rays born in each region were treated as point sources, and attenuation to neighboring regions is based on point source to point source distance. Mean gamma energy is taken to be 3.5 MeV (a very conservative estimate). Results obtained are listed in the following table:





Table 3.3.5.1

Region	I	II	III	IV
Flux* due to gammas born within the region	$4.70 \times 10^{12}$	$8.95 \times 10^{11}$	$1.27 \times 10^8$	$1.22 \times 10^3$
Flux contribution due to region I gammas	-	$4.62 \times 10^{12}$	$1.29 \times 10^{10}$	$2.09 \times 10^8$
Flux contribution due to region II gammas	$8.8 \times 10^{11}$	-	$2.98 \times 10^{10}$	$4.31 \times 10^8$
Flux contribution due to region III gammas	$4.4 \times 10^4$	$5.25 \times 10^5$	-	$4.33 \times 10^5$
Flux contribution due to region IV gammas	$8.4 \times 10^{-3}$	$9.1 \times 10^{-2}$	$5.25$	-
Total gamma flux	$5.6 \times 10^{12}$	$5.5 \times 10^{12}$	$4.3 \times 10^{10}$	$6.4 \times 10^8$

\*Flux is here defined to include all gammas of energy greater than 2 MeV.



Having determined the average gamma ray flux per region, the number of neutrons,  $n$ , produced per second is given by the relation:

$$n = N \sigma \bar{\phi}_\gamma V \text{ neutrons/sec,} \quad (3.3.5.1)$$

where

$N$  = atom density of  $H^2 = 6.6 \times 10^{22}$  atoms/cm<sup>3</sup>,

$\sigma$  = activation cross section =  $1.5 \times 10^{-27}$  cm<sup>2</sup>,

$\bar{\phi}_\gamma$  = average region gamma flux

$V$  = volume of  $D_2O$  in the region.

Table 3.3.5.2

Region	Photoneutrons, $n$ , born per second
I	$1.09 \times 10^{14}$
II	$1.07 \times 10^{14}$
III	$8.4 \times 10^{11}$
IV	$1.25 \times 10^{10}$

The neutron and proton released by the  $H^2 (\gamma, n) H^1$  reaction share equally the difference between the gamma energy and the threshold energy. Assuming an average reaction gamma energy of 3.5 MeV, the average energy of the neutron released is 0.64 MeV. Conservatively, the energy spectrum of the photoneutrons born in the coolant tank can be approximated as a fission spectrum. The neutron flux on the reactor top is therefore calculated by substituting



into Eq. 3.3.4.1.1. To the results obtained from Eq. 3.3.4.1.1, which included neutron attenuation due to distance,  $D_2O$ , iron and lead was multiplied a factor of  $10^{-2}$  to account for the attenuation due to the 6 in. of masonite (16). The calculated results are summarized in the following table:

Table 3.3.5.3

Region	Neutrons/cm <sup>2</sup> -sec	Dose Rate (mrem/hr)
I	$2.8 \times 10^{-13}$	$3.3 \times 10^{-14}$
II	$6.5 \times 10^{-4}$	$7.6 \times 10^{-5}$
III	0.03	0.004
IV	<u>0.09</u>	<u>0.010</u>
Total	0.12	0.014

As the above tabulated values show, the addition of 6 in. of masonite is sufficient to reduce the neutron dose rate on the reactor top to a very low level. From a dose rate point of view, it would be possible to reduce the thickness of the masonite. However, since masonite is relatively inexpensive, the reduction of neutron induced activation of reactor top structural materials resulting from the additional masonite shielding is well worth the small additional expense. A low activity level is particularly desirable in planning for the eventuality that one may want at some future time to disassemble the reactor top shielding enclosure.



### 3.4 Shielding Calculations, Reactor Shutdown (Phase I)

#### 3.4.1 General

The predominate radiation sources in the reactor after shutdown are: (1) fission product decay gammas, (2) gammas from the induced activity of the structure and the coolant, and (3) the photodisintegration of deuterium. Immediately after reactor shutdown, radiation due to delayed neutrons should also be considered.

Quite obviously, the magnitude of the shutdown radiation sources is only a small fraction of that for the reactor operating at power. Consequently, a calculation of the dose rate on the reactor top after shutdown would, under normal circumstances, yield a minute result which would have little meaning. There are, however, two important situations in which the dose rate on the reactor top due to shutdown radiation may be quite significant: (1) when reactor top shielding is removed from the area directly above the core tank, and (2) immediately after shutdown when all coolant is lost from the necked core tank.

#### 3.4.2 Reactor Top Shield Plug Removed

Shielding directly above the reactor core tank would not normally be removed except for purposes of reactor maintenance or repair. Assuming, for instance, that the reactor is shut down at 5 p.m. on Friday, work in the area of the reactor top would not commence until Saturday morning, a cooling time of at least 14 hours. During this time period,





virtually all the activity due to  $\text{Al}^{28}$  ( $T_{1/2} = 2.3$  min) and  $\text{N}^{16}$  ( $T_{1/2} = 7.35$  sec) decay will have died away.

From Figure 3 of reference (13), the total gamma energy decay rate after infinite operation followed by a 14 hour decay period is approximately  $1.5 \times 10^{10}$  MeV/watt-sec.

Following operation at 5 MW this figure becomes  $7.5 \times 10^{16}$  MeV/sec. Again taking the average gamma energy to be 2 MeV, the fission product decay source strength is  $3.75 \times 10^{16}$  gammas/sec.

Equation 3.3.1.1 is again used to determine the gamma flux on the reactor top, where in this case gamma attenuation is due only to distance and the coolant in the necked core tank. The calculated result is  $\phi = 1.03 \times 10^5$  gammas/cm<sup>2</sup>-sec, which converts to a dose rate of 303 mrem/hr.

In order to determine the number of photoneutrons produced by the fission product decay gammas, it is necessary to determine the flux of gammas in excess of 2.23 MeV as a function of position in the coolant tank. Figure 3.2b of reference (12) shows that gammas in excess of 2 MeV comprise roughly 3% of the total decay gamma source strength 14 hours after shutdown. The decay gamma source strength capable of initiating the  $\text{H}^2 (\gamma, n) \text{H}^1$  reaction is therefore,

$$\frac{(0.03)(7.5 \times 10^{16} \text{ MeV/sec})}{2.3 \text{ MeV/gamma}} = 9.8 \times 10^{14} \text{ gammas/sec.}$$



The core tank was divided into three regions (shown in Figure 3.4.2.1) and the average gamma flux per region calculated using Eq. 3.3.1.1. Knowing the average flux capable of inducing the  $(\gamma,n)$  reaction, the number of photoneutrons produced in each region was calculated using Eq. 3.3.5.1, where for fission product decay gammas the average activation cross section was taken to be 0.001 barns. Results obtained are summarized in the following table:

Table 3.4.2.1

Region	Gamma Flux (gammas/cm <sup>2</sup> -sec)	Neutrons Produced (neutrons/sec)
I	$1.87 \times 10^{10}$	$1.41 \times 10^{12}$
II	$2.23 \times 10^8$	$2.88 \times 10^9$
III	$7.92 \times 10^5$	$1.02 \times 10^7$

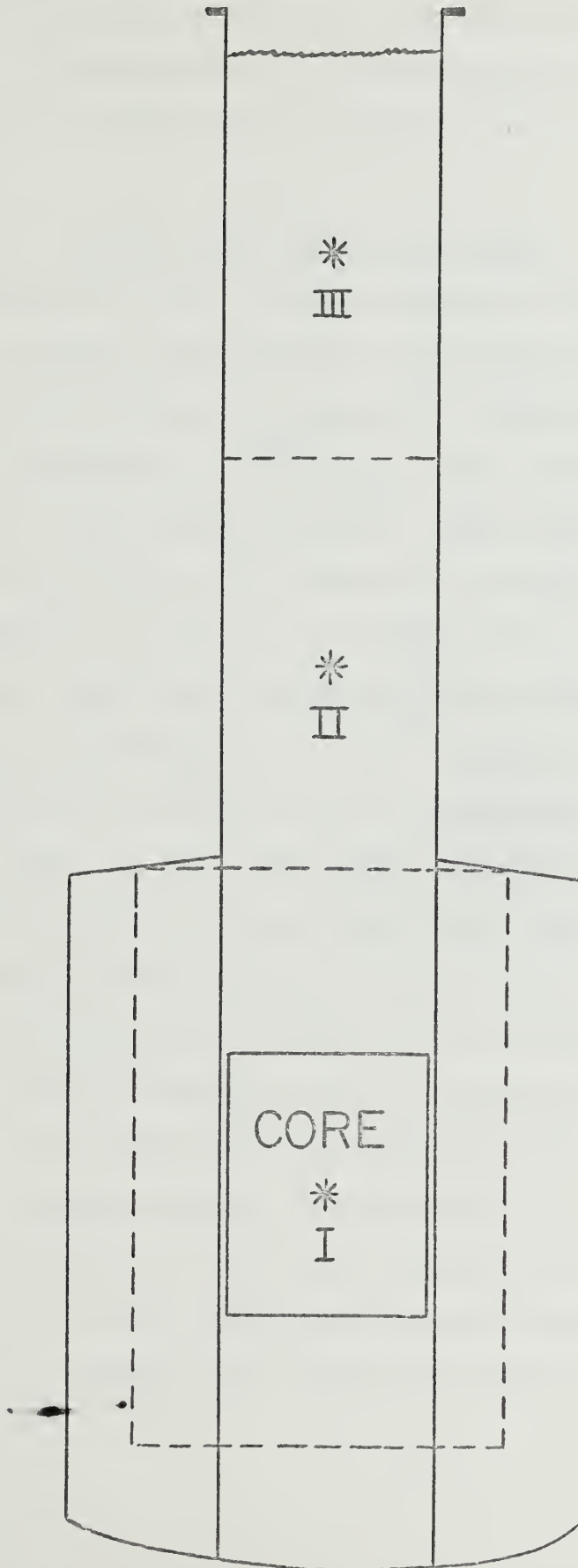
Taking the average activation gamma ray energy to be 2.3 MeV, the average energy of the photoneutron is calculated to be:

$$\frac{2.30 - 2.23}{2} = 35 \text{ KeV}$$

Neutrons of such low energy will be thermalized very near their birthplace by the surrounding D<sub>2</sub>O. The photoneutrons generated due to decay gammas are therefore considered to be thermal neutrons, and the method of Section 3.3.4.2 is used to determine the neutron flux on the surface of the core tank. Having reached the surface, the neutrons are assumed to radiate as a point source out through the opening



REGIONS FOR PHOTO-NEUTRON CALCULATIONS





in the reactor top shielding. The dose rate on the reactor top due to photoneutrons is calculated to be 0.03 mrem/hr, negligible in comparison to the dose rate due to decay gammas.

### 3.4.3 Coolant Lost from Necked Tank

Immediately after reactor shutdown coincident with the loss of coolant in the necked core tank, the primary sources of radiation would be the decay of fission products in the core and the decay of  $\text{Al}^{28}$  in the core and surrounding structure. From Section 3.3.2.1, the initial  $\text{Al}^{28}$  rate of decay will be  $4.97 \times 10^{16}$  gammas per second, the decay gammas having an energy of 1.8 MeV (taken as 2 MeV for calculations). The total source strength immediately after shutdown is, therefore,  $6.2 \times 10^{17}$  gammas per second. The gamma flux on the reactor top is calculated using Eq. 3.3.1.1, where in this case gamma attenuation is due only to distance and the iron and lead shielding on the reactor top. The calculated result is  $\phi = 1.3 \times 10^5$  gammas/cm<sup>2</sup>-sec, which converts to a dose rate of 383 mrem/hr. After 14 hours, should coolant still be absent from the necked core tank, the dose rate on the reactor top will have decayed to approximately 23.2 mrem/hr.

In Section 3.3.4.1 it was assumed that  $2.31 \times 10^{17}$  neutrons per second leak from the core during normal operation. Assuming the delayed neutrons fraction to be





0.007,  $1.63 \times 10^{15}$  of these neutrons are delayed neutrons. Therefore, at the instant of reactor shutdown the core will continue to emit  $1.62 \times 10^{15}$  neutrons/sec. Using the method of Sections 3.3.4.1 and 3.3.5, the neutron dose on the reactor top at the instant of shutdown is calculated, where in this case neutron attenuation is provided only by distance and the masonite, iron and lead shielding. The result is 18.5 rem/hr. Fortunately, the half-life for delayed neutron emission is small (0.43 - 55.6 seconds) and so after about 15 minutes the dose rate on the reactor top would be negligible (15).

Needless to say, should coolant be lost from the necked core tank, personnel should stand well clear of the area immediately above the necked core tank.

### 3.5 Dose Rate Through Concrete Shielding (Phase I)

Thus far in this chapter all shielding calculations have been performed for radiation passing up through the necked coolant tank and out through the reactor top shielding enclosure. Although one can reasonably expect that the 6-1/2 feet of dense concrete which shields the reactor top work area surrounding the necked core tank will allow only minute radiation levels on the reactor top, one brief and approximate calculation is in order. An estimation of the required density for the reactor top shielding concrete will also be made.



All radiation, except the thermal neutron flux, is assumed to be emitted from a point source located at the core center. Radiation source levels as a function of energy were taken from the preceding sections of this chapter.

Table 3.5.1

Energy (MeV)	Gamma Ray Source Strength (gammas/sec)
8	$1.74 \times 10^{16}$
7	$1.14 \times 10^{15}$
6	$4.56 \times 10^{16}$
4	$3.80 \times 10^{16}$
3	$3.87 \times 10^{17}$
2	$6.50 \times 10^{17}$
1	$1.17 \times 10^{18}$

Fast neutron source strength =  $2.31 \times 10^{17}$  neutrons/sec.

Thermal neutron flux at the tank wall =  $10^{12}$  neutrons/cm<sup>2</sup>-sec. Gamma ray attenuation through the D<sub>2</sub>O and concrete shielding is calculated utilizing Eq. 3.3.1.1 where for the current case:

$$\phi = \frac{S}{4\pi(R_D+R_C)^2} (B_D+B_C) 10^{-(D_D+D_C)}, \quad (3.5.1)$$

where the subscripts D and C refer to D<sub>2</sub>O and concrete respectively. Decade lengths as a function of energy were taken from reference (7). The calculated results appear in the following table:



Table 3.5.1

Energy (MeV)	$D_{D_2O}$	$D_{concrete}^*$	$B_{D_2O}$	$B_{concrete}$	$\phi(\gamma's/cm^2-sec)$	Dose Rate (mrem/hr)
8	0.95	11.6	1.8	18.6	0.110	$8.6 \times 10^{-4}$
7	1.00	11.7	1.9	20.0	0.005	$3.6 \times 10^{-5}$
6	1.10	11.8	2.1	21.8	0.135	$8.6 \times 10^{-4}$
4	1.34	13.2	2.8	25.0	0.003	$1.4 \times 10^{-5}$
3	1.57	14.1	3.4	32.3	0.003	$1.1 \times 10^{-5}$
2	1.96	15.7	5.4	45.3	0.00007	$2.7 \times 10^{-7}$
1	2.80	23.3	13.5	155.1	$2 \times 10^{-12}$	$3.5 \times 10^{-15}$
					Total	$1.78 \times 10^{-3}$

\*Concrete of specific gravity = 4.5.



Equation 3.3.4.1.1 is used to determine the fast neutron flux on the reactor top. Converting the exponential attenuation coefficients to decade lengths,

$$d_{D_2O} = 0.0754 \times 10.7 = 0.806 \text{ ft.},$$

$$d_{\text{concrete}} = 0.8 \text{ ft. (experimentally measured value for O.W.R. concrete shielding, specific gravity = 4.6).}$$

Substituting into Eq. 3.3.4.1.1,

$$\phi = \frac{2.31 \times 10^{17}}{4\pi [(3+6.5)30.48]^2} 10^{-(3.72 + 8.13)}$$

$$\phi = 0.242 \text{ neutrons/cm}^2\text{-sec.}$$

Therefore, Dose Rate = 0.028 mrem/hr.

Thermal neutron attenuation through the concrete shielding was calculated using Eq. 3.2.3.2, where for concrete with specific gravity = 4.5 Gage has determined that  $L = 1.91$  cm., and  $D = 0.372$  cm. Substituting into Eq. 3.2.3.2 yields:

$$\phi = 2.58 \phi_0 e^{-x/1.91} \quad (3.5.2)$$

A thermal neutron decade length in concrete is equal to  $0.0754 \times (L) = (0.0754)(1.91) = 0.144$  ft. Therefore,

$$\phi = 2.58 \phi_0 10^{-x/0.144}, \text{ or } \phi = (2.58 \times 10^{12})(10^{-x/0.144})$$

$$\phi = (10^{12.412})(10^{-6.94x})$$





In order to reduce the thermal neutron flux to 1 neutron/cm<sup>2</sup>-sec, a concrete thickness of  $x = \frac{12.412}{6.94} = 1.8$  ft. is required. Thus, nearly all the thermal neutrons from the tank will be absorbed in the first 2 ft. of concrete. Beyond the first 2 ft. the thermal neutron flux results from the slowing down of the fast flux, and is thus approximately equal to the fast flux at each point.

Although the calculations of this section indicate a dose rate through the concrete shielding of 0.03 mrem/hr, thereby indicating that concrete of specific gravity = 4.5 is actually more dense than required, it is felt that dose rate uncertainties attendant with the various penetrations through the upper concrete shielding are sufficient to warrant the use of the s.g. = 4.5 concrete.

### 3.6 Shielding Calculations Summary (Phase I)

#### 3.6.1 Dose Through Shielding Directly Above the Core

<u>Source</u>	<u>Dose Rate (mrem/hr)</u>
Core Prompt Fission Gammas	0.068
Al <sup>27</sup> (n, $\gamma$ ) Al <sup>28</sup>	0.064
N <sup>16</sup> Decay	0.04
H <sup>2</sup> (n, $\gamma$ ) H <sup>3</sup>	0.0018
Fission Product Decay Gammas	0.0004
Fast Fission Neutrons	0.002
Thermal Neutrons	0.005
Photoneutrons	<u>0.014</u>
Total	0.195 mrem/hr.



### 3.6.2 Dose Through Reactor Top Concrete

<u>Source</u>	<u>Dose Rate (mrem/hr)</u>
All Sources Combined	0.0018 mrem/hr

### 3.6.3 Shielding Conclusions

The maximum dose rate anywhere on the High Flux MITR top is calculated to be less than 0.2 mrem/hr. This figure is a factor of 5 less than the design goal, and a factor of 12.5 less than the limit set by the AEC. The reactor top shielding, as described in previous sections of this chapter, is therefore considered adequate and safe.

## 3.7 Shielding Calculations, Normal Operation (Phase II)

### 3.7.1 General

The phase II design differs from the phase I design, for shielding purposes, in three basic ways: (1) the water column above the core is light water instead of heavy water, (2) the water column above the core is 11 ft. high vice 8 ft., and (3) the shielding lid on top of the water column is simply a flat cover instead of the "doghouse" enclosure shown in Figure 3.1.1. In going from phase I to phase II, the magnitude of the shielding problem was greatly reduced. No longer need one be bothered by tritium, either from a health physics or a shielding standpoint. Light water makes a much better neutron shield than heavy water due to its much larger neutron absorption cross section, and in addition does not act as a source for



photoneutrons. By iterative calculations, it was determined that a lead shield 10 inches thick on top of the water column would provide adequate shielding. The following calculations serve to justify this choice and to indicate the expected dose rate on the reactor top.

### 3.7.2 Fission Gamma Rays

Table 3.7.2.1 presents the calculations for the leakage of fission gamma rays through the lead shielding lid on the tank top.

Table 3.7.2.1

<u>Material</u>	<u>Thickness</u>	1 Mev		3 Mev		6 Mev	
		<u>D</u>	<u>B</u>	<u>D</u>	<u>B</u>	<u>D</u>	<u>B</u>
H <sub>2</sub> O	12 ft.	11.2	170	6.3	12.3	4.4	5.4
Lead	10 in.	<u>8.8</u>	<u>6</u>	<u>5.2</u>	<u>6.4</u>	<u>5.6</u>	<u>10.2</u>
	Totals	20.0	176	11.5	18.7	10.0	15.6
$\emptyset(r)$ (no attenuation)		$1 \times 10^{12}$		$3.3 \times 10^{11}$		$3 \times 10^{10}$	
$\gamma$ 's/cm <sup>2</sup> -sec							
$\emptyset$ (attenuated)		$1.76 \times 10^{-6}$		19.5		46.8	
$\gamma$ 's/cm <sup>2</sup> -sec							
Conversion Factor		700		270		158	
Dose Rate (mrem/hr)		$2.5 \times 10^9$		0.072		0.292	
Total Dose Rate = 0.364 mrem/hr							

### 3.7.3 Material Activation

#### 3.7.3.1 Al<sup>27</sup> (n, $\gamma$ ) Al<sup>28</sup>

From Section 3.3.2.2 it is seen that the only significant contribution to the reactor top dose rate is made by



6 and 8 MeV gammas from regions II and III. Collapsing the  $\text{Al}^{27} (n, \gamma) \text{Al}^{28}$  source strength to a point source located at the core center, a source of  $5 \times 10^{16}$  gammas/sec is obtained. Calculated results are given in the following table.

Table 3.7.3.1.1

Material	Thickness	6 Mev		8 Mev	
		D	B	D	B
H <sub>2</sub> O	12 ft.	4.4	5.4	3.78	4.0
Lead	10 in.	<u>5.6</u>	<u>10.2</u>	<u>5.75</u>	<u>11.0</u>
Totals		10.0	15.6	9.53	15.0

$\emptyset(r)$  (no attenuation)  $3.42 \times 10^{10} \text{ } \gamma\text{'s/cm}^2\text{-sec}$

Fraction  $0.21$   $0.35$

$\emptyset$  (attenuated)  $\gamma\text{'s/cm}^2\text{-sec}$   $11.2$   $53$

Conversion Factor  $158$   $128$

Dose Rate (mrem/hr)  $0.071$   $0.415$

Total Dose Rate =  $0.485$  mrem/hr

### 3.7.3.2 $\text{H}^1 (n, \gamma) \text{H}^2$

The production of gamma rays from thermal neutron capture in hydrogen was not treated in the phase I calculations, and so will be described here. One gamma ray of energy 2.23 MeV is emitted in the  $\text{H}^1 (n, \gamma) \text{H}^2$  reaction, the reaction cross section being 0.33 barns (7). In order to simplify calculations, the water in the core was considered to be a sphere 1 ft. in radius and the average





thermal neutron flux over the sphere taken to be  $5 \times 10^{13}$  neutrons/cm<sup>2</sup>-sec. The number of neutron captures by hydrogen was calculated by the following equation, which is also the number of gamma rays emitted. A point source of gamma rays was assumed at the core center and attenuation of gamma rays through the water and lead shielding was calculated as before.

$$\begin{aligned} \text{neutron captures/cm}^3\text{-sec} &= N\sigma_a\phi = \Sigma_a\phi \\ \text{neutron captures/sec} &= V\Sigma_a\phi = \text{gamma rays/sec} \end{aligned}$$

$$N = 6.71 \times 10^{22} \frac{\text{atoms H}^1}{\text{cm}^3}$$

$$V = 119,000 \text{ cm}^3$$

$$\Sigma_a(\text{H}) = 0.0221 \text{ cm}^{-1}$$

$$\text{gamma rays/sec} = 1.3 \times 10^{17} \text{ (assumed to be 2 MeV)}$$

The results of the dose rate calculation are given in the following table:

Table 3.7.3.2.1

Material	Thickness	D	B
Water	12 ft.	7.85	24.0
Lead	10 in.	<u>5.7</u>	<u>6.2</u>
	Totals	13.55	30.2

$$\phi(R) \text{ (no attenuation)} = 8.9 \times 10^{10} \text{ } \gamma\text{'s/cm}^2\text{-sec}$$

$$\phi(R) \text{ (attenuated)} = 0.076 \text{ } \gamma\text{'s/cm}^2\text{-sec}$$

$$\text{Dose Rate} = 2.23 \times 10^{-4} \text{ mrem/hr}$$



### 3.7.3.3 $^{16}\text{O}$ (n,p) $^{16}\text{N}$

In the phase II design the coolant water with its  $^{16}\text{N}$  activity will not circulate in the upper 4 ft. of the necked core tank. Thus, to calculate the reactivity on the reactor top for the phase II design, the point source strength calculated in Section 3.3.2.3 will be assumed to be located 4 ft. below the surface of the water in the necked core tank. Table 3.7.3.3.1 presents the calculated results:

Table 3.7.3.3.1

Material	Thickness	D	B
Water	4 ft.	1.47	2.5
Lead	10 in.	<u>5.6</u>	<u>10</u>
	Totals	7.07	12.5

$$\phi(R) \text{ (no attenuation)} = 5.45 \times 10^6 \text{ } \gamma\text{'s/cm}^2\text{-sec}$$

$$\phi(R) \text{ (attenuated)} = 5.8 \text{ } \gamma\text{'s/cm}^2\text{-sec}$$

$$\text{Conversion factor} = 158$$

$$\text{Dose Rate} = 0.037 \text{ mrem/hr}$$

### 3.7.4 Neutrons

The attenuation equation given in Section 3.3.4.1 can be used to show that the fast neutron flux from the core is nearly zero at the reactor top. The equation is:



$$\phi = \frac{S}{4\pi R^2} e^{-\Sigma \frac{\chi}{\lambda_r}} \text{ neutrons/cm}^2\text{-sec}$$

$$R = 13 \text{ ft.}$$

$$(H_2O) = 12 \text{ ft.}$$

$$\lambda_r(H_2O) = 9.98 \text{ cm.}$$

$$\chi(\text{Pb}) = 10 \text{ in.}$$

$$\lambda_r(\text{Pb}) = 8.94 \text{ cm.}$$

$$S = 2.31 \times 10^{17} \text{ neutrons/sec}$$

$$\phi = 5.7 \times 10^{-4} \text{ neutrons/cm}^2\text{-sec}$$

The dose rate due to fast neutrons on the reactor top is thus only  $6.6 \times 10^{-5}$  mrem/hr.

The dose rate due to thermal neutrons is easily seen to be negligible. The diffusion equation for thermal neutrons from an infinite plane source in an infinite homogeneous medium is:

$$\phi = \phi_0 \frac{L e^{-\chi/L}}{2D} \text{ neutrons/cm}^2\text{-sec}$$

$L$  = diffusion length, cm

$D$  = diffusion coefficient, cm

$\chi$  = thickness of attenuating material, cm.

For  $H_2O$ ,  $L = 2.88$  cm,  $D = 0.183$  cm, and the column height is 305 cm. The thermal neutron flux is thus attenuated by about a factor of  $10^{-45}$  in the water column above the core.

### 3.8 Shielding Calculations, Reactor Shutdown (Phase II)

The calculations performed in Section 3.4 were repeated for the phase II reactor design in order to complete the



comparison of shielding calculations for the two design phases. For the case of the reactor top shield plug removed, the calculated gamma flux at the coolant tank surface after a 14 hour decay period is  $7.5 \times 10^3$  gammas/cm<sup>2</sup>-sec, which converts to a dose rate of 22 mrem/hr. Were one fuel element to be raised to a position 8 ft. beneath the surface of the water (such as during a fuel flipping operation), however, the dose rate at the surface of the water would be about 480 mrem/hr. Thus, it is apparent that personnel should be protected by shielding when conducting refueling or fuel flipping operations.

The dose rate shortly after shutdown if coolant is lost from the necked core tank is calculated to be 12 rem/hr. After 14 hours the dose rate would decay to about 700 mrem/hr.

### 3.9 Shielding Calculations Summary (Phase II)

#### 3.9.1 Dose Through Reactor Top Shield Plug

<u>Source</u>	<u>Dose Rate (mrem/hr)</u>
Core Fission Gammas	0.364
Al <sup>27</sup> (n, $\gamma$ ) Al <sup>28</sup>	0.485
H <sup>1</sup> (n, $\gamma$ ) H <sup>2</sup>	0.0002
N <sup>16</sup> decay	0.037
Fast neutrons	0.0006
Thermal neutrons	<u>negligible</u>
Total	0.89 mrem/hr





### 3.9.2 . Dose Through Reactor Top Concrete

Same as Phase I

0.0018 mrem/hr

### 3.9.3 Shielding Conclusions

The maximum dose rate anywhere on the reactor top is calculated to be 0.89 mrem/hr. This figure is less than the design goal of 1.0 mrem/hr, and thus the 10 in. lead shield on top of the necked core tank is considered to provide adequate shielding protection.



## Chapter 4

## HEAT TRANSFER, PRELIMINARY CALCULATIONS

4.1 General

It was the purpose of the preliminary heat transfer calculations to determine whether or not the heat from the proposed High Flux MITR core could be adequately removed utilizing the currently installed process system. Although the calculations of this chapter were originally done for the phase I core design, they are equally applicable to the phase II design. Section 4.6 will indicate the differences in the two phases with respect to heat transfer.

In establishing the limiting temperature parameters for the operation of the High Flux MITR, the maximum design values given in the technical specifications for the present MITR were adhered to. These criteria are that the temperature at the hottest spot in the hottest fuel plate not exceed  $450^{\circ}\text{C}$  ( $842^{\circ}\text{F}$ ) under any circumstances, and that under normal operating conditions boiling must not be allowed to occur anywhere in the core. The  $450^{\circ}\text{C}$  temperature limitation was established by consideration of the structural stability of the aluminum fuel elements. While aluminum does not melt until it reaches approximately  $650^{\circ}\text{C}$ , it begins to soften significantly at about  $450^{\circ}\text{C}$  (18). The requirement that no



boiling be allowed to occur in the core was originally intended as a safety factor which would act as a backup to insure that the fuel plate hot spot would not exceed  $450^{\circ}\text{C}$ , and also to avoid the problem of flow instability caused by boiling. Neglecting the reactivity effects of voiding, if the coolant saturation temperature were exceeded sufficiently to cause nucleate boiling at some point on the fuel plate, the vapor bubbles formed at the fuel plate surface would either collapse at the wall or would leave the wall and collapse after traveling a short distance into the highly subcooled bulk fluid. The bubble formation would cause considerable agitation of the coolant and thereby lead to a substantial increase in the convective heat transfer coefficient. Heat would thereby be conducted away from the fuel plate surface at a greater rate, and thus tend to reduce the wall temperature.

However, as briefly mentioned in the introduction to this thesis, the reactivity effect of voiding in the area of the outermost fuel plates could be positive, although all core physics calculations done thus far indicate a negative value. Because the possibility of a local positive voiding coefficient does exist, however, one is provided with added incentive to insure boiling does not occur.

Because the fuel plates are so thin (0.050 in.) and because aluminum is a good conductor of heat



( $K = 119 \text{ BTU/hr-ft-}^\circ\text{F}$  for pure aluminum), the maximum temperature at any point within a fuel plate will be at most on the order of 3 to 4 degrees F above the fuel plate wall temperature at the same point.

#### 4.2 Distribution of Reactor Heat Load

The High Flux MITR will generate 5 megawatts of thermal energy which must be removed by the reactor coolant systems. For the purposes of fuel plate hot spot calculations, however, only that portion of the generated heat which is transferred to the coolant as it flows up through the core is of interest. This includes heat transferred to the  $\text{D}_2\text{O}$  coolant both by conduction through the faces of the fuel plates and by gamma ray and neutron interaction with the coolant.

Wolak has determined the total fission energy absorbed in the present MITR, operating at 1 megawatt, to be 198.22 MeV/fission (19). The specific distribution of this absorbed energy is given in Table 4.2.1.

Although the spectrum from the proposed high flux MITR will be harder than that for the present MITR, and although the amount of aluminum structure may be somewhat different, the value of 198.22 MeV/fission for the total fission energy absorbed is probably a good estimate for the High Flux MITR. As shown in Table 4.2.1, not all of this





Table 4.2.1

Fission Energy Absorption Distribution (Present  
MITR)

Fuel Elements	MeV/fission	% Total
K.E. Fission Fragments	168.00	
K.E. Beta Particles	7.00	
Gamma Energy	<u>4.29</u>	
	179.29	90.5
<u>D<sub>2</sub>O</u>		
K.E. Fast Neutrons	5.00	
Gamma Energy	<u>10.24</u>	
	15.24	7.7
<u>Shield</u>		
Gamma Energy	<u>3.69</u>	<u>1.8</u>
Total	198.22	100.0

energy is absorbed by the D<sub>2</sub>O coolant as it passes through the fuel elements. 1.8% of the total fission energy, in the form of gamma ray captures in the thermal shield, is carried away by the thermal shield coolant. The remaining 98.2% of the fission energy is transferred to the D<sub>2</sub>O coolant by conduction through the walls of the fuel plates or deposited directly into the D<sub>2</sub>O. Of the 15.24 MeV/fission deposited directly into the D<sub>2</sub>O within the reactor, DeVoto has estimated for the present MITR operating with a 19 element core that 9.03 MeV/fission of the gamma ray



energy and 2.5 MeV/fission of the energy carried by the fast neutrons are deposited in the D<sub>2</sub>O outside the fuel element boxes (20). Since the ratio of D<sub>2</sub>O outside the coolant channels to D<sub>2</sub>O in the coolant channels will be approximately the same in the High Flux MITR as in the present MITR, it seems feasible to assume that the above figures will still be reasonably valid. Following DeVoto's method of estimating the fraction of gamma energy deposited in the D<sub>2</sub>O inside the fuel elements as the ratio of D<sub>2</sub>O volume inside the fuel elements to total D<sub>2</sub>O volume, one obtains for the High Flux MITR

$$\frac{\pi(10)^2 \left(\frac{1.67}{1.77}\right)}{\pi(24)^2} = 0.164.$$
 Therefore, the percentage of total fission gamma energy deposited in the D<sub>2</sub>O as it flows through the fuel elements becomes  $(0.164)(10.24) + \frac{2.50}{198.22} = 2.1\%$ . Due to the fact that the close packed core will

lead to greater particle energy dissipation before the gamma rays can escape the core than currently exists, the above figures for gamma energy deposited in the D<sub>2</sub>O outside the coolant channels may be a little high and therefore not conservative. However, the difference is probably quite small. Hence, it will be assumed that 92.6% of the total fission energy will be deposited in the D<sub>2</sub>O coolant as it passes up through the fuel elements, and that 90.5% of the total fission energy will be conducted through the walls of the fuel plates and into the D<sub>2</sub>O coolant. (Note:



approximately 11 MeV per fission is carried off by neutrinos resulting from beta decay. However, since this neutrino energy is not deposited anywhere in the reactor it is not considered in thermal power calculations.)

In the calculations which follow, the heat flux affecting the coolant temperature rise will be reduced to 92.6% of the total, and the specific heat flux at the hot spot will be reduced to 90.5% of its computed value based on 5 megawatts.

#### 4.3 Hot Channel Factors

For conservative design, it is necessary to anticipate uncertainties in operating conditions, fuel element fabrication, design relations, etc. These uncertainties are expressed in terms of the hot channel factors which are elaborated below. An overall hot channel factor has been estimated for the present MITR by DeVoto to be 1.25. This estimate, however, not only includes inaccuracies introduced by the manufacturing tolerances, but also includes a consideration of variations in flux distribution through each element contained in the core. DeVoto's value is somewhat lower than those normally found in the literature due to the fact that he has given credit for several aspects in the design which tend to reduce the value of the heat flux at the hot spot. (20) . It is because DeVoto's results contain consideration of the neutron flux



distribution, and the proposed High Flux MITR differs radically from the present MITR in this respect, that direct application of DeVoto's results cannot be assumed to be valid for the High Flux MITR.

In determining values of hot channel factors to use for the High Flux MITR in order to account for variations in primary design variables caused by manufacturing tolerances, it seems appropriate to compare the magnitude of the tolerances which are specified for the present MITR, and which will also apply to the High Flux MITR, with those specified for the Brookhaven High Flux Beam Reactor (HFBR) (21). In this manner the hot channel factors determined for the Brookhaven reactor can be adjusted so as to make them applicable to the High Flux MITR. The contribution to the overall hot channel factor due to the variation in neutron flux along an element will not be determined as a separate sub-factor, but rather the variation in neutron flux will be used directly to determine average power produced per element and hot spot location on the element.

Since the calculations to be performed in this chapter will primarily be for the hottest spot in the core, the hot channel factors of interest will be the heat flux and heat transfer coefficient hot channel factors. The contribution of each individual item to either of these





overall hot channel factors are termed sub-factors. The sub-factors are multiplied by each other to determine the overall hot channel factor. A listing and description of the hot channel sub-factors follows:

1. Channel Dimensional Tolerance

The hot spot temperature rise due to the channel dimensional tolerance will occur in a channel of minimum average dimensions where the local dimension is a maximum. For the Brookhaven High Flux Beam Reactor (HFBR), the outermost coolant channels are 0.189 in. thick with a maximum tolerance of  $\pm 0.005$  in. The sub-factor determined for these characteristics was 1.09. For the phase one High Flux MITR, the coolant channels are 0.117 in. thick with a proposed maximum tolerance of  $\pm 0.005$  in. The sub-factor determined for these characteristics is

$$(F_{\Theta} = \frac{d_{\max}}{d_{\min}} \left( \frac{d_{\text{nom}}}{d_{\min}} \right)^{1/3} = \frac{.122}{.112} \left( \frac{.117}{.112} \right)^{1/3} = 1.11)$$

This factor is applied to the heat transfer coefficient hot channel factor.

2. Flow Distribution Among the Elements

Consideration of this item was not reported in reference (21). For the High Flux MITR, however, the maximum variation in the flow distribution among the elements is estimated to be  $\pm 10\%$ , as it is for the present MITR (2). It is assumed that this variation will increase the heat transfer coefficient hot channel factor by 1.10.



### 3. Fuel Core Alloy Variation

For the HFBR, local variations in the fuel loading are limited to  $\pm 5\%$  by the specification of the fuel alloy final thickness at  $0.020 \pm 0.001$  in. For the present MITR, however, no specification for the final thickness of the fuel alloy section is made. Rather, it is stated that the overall plate thickness shall not vary by more than  $\pm 0.003$  in., while the variation in the clad thickness on either side of the core alloy must be within  $\pm 0.005$  in. It is also stated in the MIT specifications that there is to be no objectionable segregation of uranium in the core alloy. Each plate is subject to radiographic inspection to determine whether such segregation exists. Hence, it is doubtful that the fuel alloy thickness of the present MITR plates exceeds the specification as quoted for the HFBR. If the U-235 segregation was sufficient to exceed this specification, the fuel plate would probably be rejected.

It is stated in reference (21) that the thickness specification made for the HFBR can be met without great difficulty by the fuel fabricator, except at the ends of the plates. Here the fuel alloy develops a local thickened region due to the plate lining process which is called the "dogbone". Since the specification for the fuel alloy



thickness (excluding the dogbone) as made for the HFBR appears sufficiently easy to satisfy, the same variation will be allowed for the High Flux MITR. Although the dogbone thickness in the HFBR is required to be no more than 10% greater than nominal thickness, a variation of 25% was allowed for in their calculations due to (1) the fact that the dogbone thickness is a sensitive item in the hot spot analysis, and (2) the fact that this is a difficult item for the fabricator to control. A 25% variation in the dogbone thickness will also be assumed for the High Flux MITR. This will give an added touch of conservatism to the hot spot calculations performed for this design. (In the phase II design, the "dogbone" is a very sensitive item because the fuel plate hot spot occurs in the region of the dogbone at the bottom of the core. Calibrated densitometer measurements will probably be required to determine the degree of dogboning.)

The fuel alloy thickness is combined with the dimensional tolerances in width and length of the fuel plates (and hence heat transfer area). The allowable variation in the core heat transfer area for the HFBR is 4.6%. The same variation is assumed to apply to the High Flux MITR. Therefore, in both the HFBR and the High Flux MITR, the heat flux term is increased by 1.10 (1.05 x 1.046)



everywhere, except at the ends of the fuel where it is increased by 1.31 (1.25 x 1.046).

#### 4. Reactor Power Measurement

It is estimated for the HFBR that the power calculator will be capable of measuring the reactor power to within 5%. The same estimate is made for the High Flux MITR. Hence, the heat flux hot channel factor is increased by 1.05 to account for this estimated variation.

#### 5. Heat Transfer Coefficient Deviation

The Phillips Reactor Safeguard Committee recommended the use of the modified Colburn correlation in the HFBR with a maximum negative deviation of 20% (21). This same correlation is used to determine the heat transfer coefficient for the High Flux MITR (Section 4.6.3). Consequently, this deviation results in increasing the heat transfer coefficient term by 1.20 for both the HFBR and the High Flux MITR.

#### 6. Summary of the Hot Channel Factors

##### Heat Flux Factors, $F_q$

Reactor power measurement error	1.05
Fuel alloy variation	<u>1.10 (1.31)*</u>
Total, $F_q$	1.155 (1.375)*

\*Value at the "dogbone"





Heat Transfer Coefficient Factors,  $F_h$

Channel dimensional tolerance	1.11
Flow distribution among the elements	1.10
Correlation equation	<u>1.20</u>
Total, $F_h$	1.46

A bulk hot channel factor was not calculated.

Instead the heat flux hot channel factors will be used when numerically integrating the power along a channel for the purpose of calculating bulk temperature rise. The design of the phase one coolant entrance plenum is such that the flow of coolant up through the outer coolant channels should be somewhat greater than the flow through the inner channels. Consequently, it is argued that this effect would overshadow any bulk hot channel sub-factors related to flow velocity, thereby making it conservative to simply neglect such sub-factors. It is these coolant flow velocity related sub-factors which distinguish the bulk hot channel factor from the heat flux channel factor. In addition, by employing the heat flux hot channel factors in determining the bulk temperature rise, the contribution to the bulk coolant temperature due to the "dogbone" effect at the fuel plate ends will be taken into account. This effect would be missed were a bulk hot channel factor calculated and used instead.



#### 4.4 Power Distribution in the Core

In order to determine the power distribution in the proposed high flux MITR core, the modified twenty grand diffusion code was used, and a two dimensional (R,Z) plot of the core power resulted. The basic core configuration and parameters utilized are described here.

A cylindrical homogenized core 24 centimeters in radius and 65 centimeters high was assumed. The core and surrounding reflector area were divided into 14 regions as shown in Figure 4.4.1. The material composition of each region is listed in Table 4.4.1. The calculations were done in four neutron energy groups:

Group 1:	$\infty$	-	$821 \times 10^3$	eV
Group 2:	$821 \times 10^3$	-	$5.53 \times 10^3$	eV
Group 3:	$5.53 \times 10^3$	-	0.625	eV
Group 4:	0.625	-	0.025	eV

The epithermal group cross sections for Boron, Hydrogen, Oxygen, and Uranium (235) were obtained from the table of "Few Group Cross Sections for Metal-H<sub>2</sub>O Systems Fueled with U<sup>235</sup>" found on page 142 of ANL-5800. The thermal cross sections for the above three elements were taken from the 16 group table of "Multigroup Constants for Fast Reactor Analysis (LASL)" found on pages 569-574 of ANL-5800. The 4 group cross sections for Deuterium and



FIGURE 4.4.1.  
LAYOUT OF REGIONS FOR TWENTY  
GRAND CALCULATION.

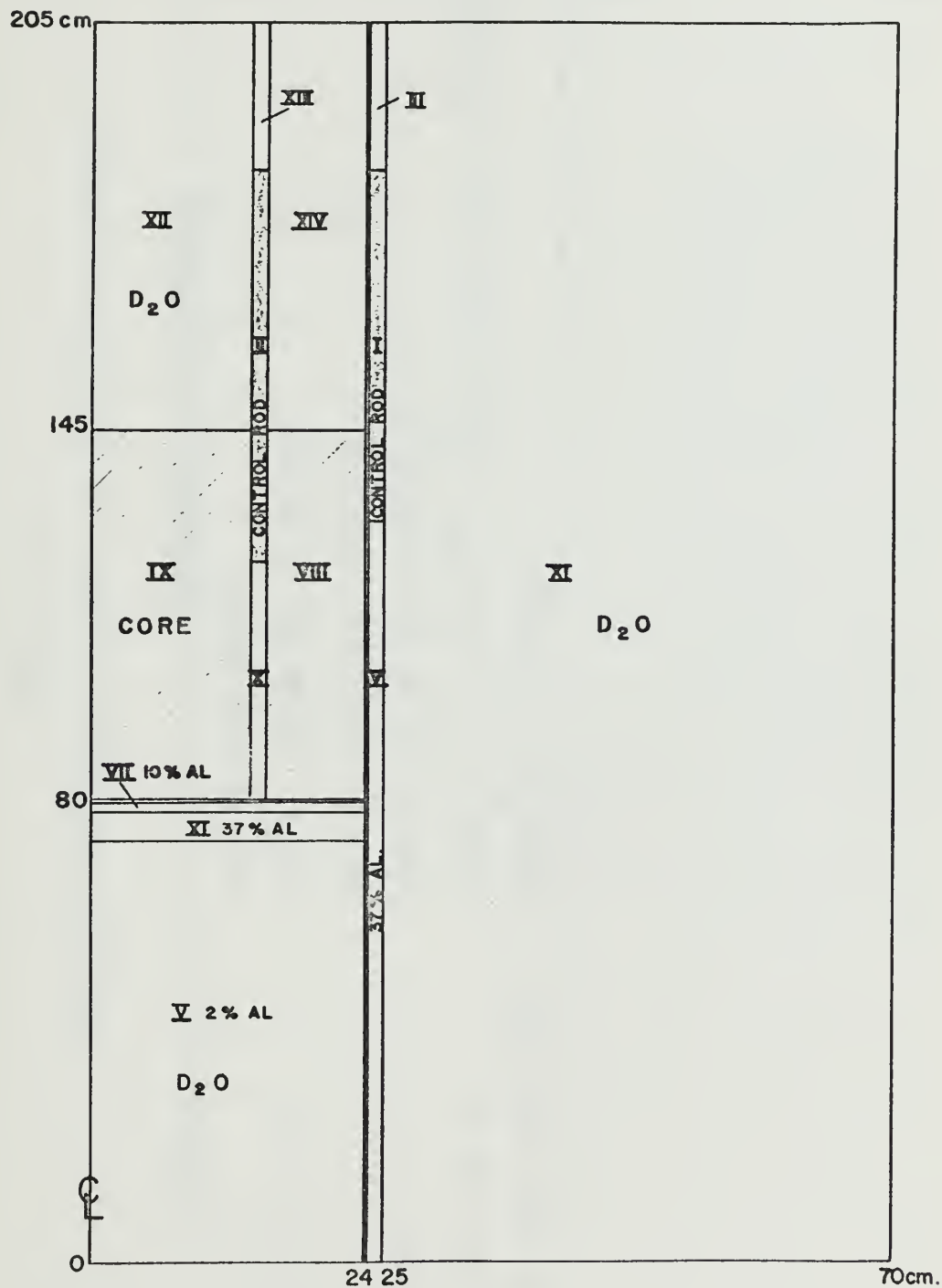




Table 4.4.1

## Material Composition of Core and Reflector by Regions

Region	Materials by Percentage
I, II	100% Natural Boron
III, IV, VI	37% Al, 62.8% D <sub>2</sub> O, 0.2% H <sub>2</sub> O
V	2% Al, 97.7% D <sub>2</sub> O, 0.3% H <sub>2</sub> O
VII	10% Al, 89.7% D <sub>2</sub> O, 0.3% H <sub>2</sub> O
VIII, IX, X	0.34% U <sup>235</sup> , 0.03% U <sup>238</sup> , 43% Al, 56.2% D <sub>2</sub> O, 0.17% H <sub>2</sub> O
XI, XII, XIII, XIV	99.7% D <sub>2</sub> O, 0.3% H <sub>2</sub> O





Uranium (238) were obtained by collapsing the 16 group cross sections to four energy groups. Fuel plate loading was taken to be 1.5 times the fuel loading in the present MITR core, or 15 grams of 93% enriched uranium per fuel plate.

It should be noted at this point that the purpose of the computer calculation was to obtain a rough estimate of the power distribution in the core in order to have some foundation upon which to base preliminary heat transfer calculations. The assumptions made concerning core size, composition, and control rod position could only be described as educated guesses based on information available at the time. Due to the expense involved in running the twenty grand program, only one run could be made. More detailed and precise core physics calculations were concurrently being performed by Andrews Addae. The core power distribution is shown plotted in Figure 4.4.2. As expected, this plot shows that the outermost fuel plate generates the greatest amount of power and therefore it is on the outermost fuel plate that the core hot spot will be found. Table 4.4.2 lists the power generated (in watts) at the various mesh points in the core. (Thermal neutron flux in both the core and reflector has been plotted in Figure 4.4.3 in order to illustrate why the core power distribution takes the shape it does.)



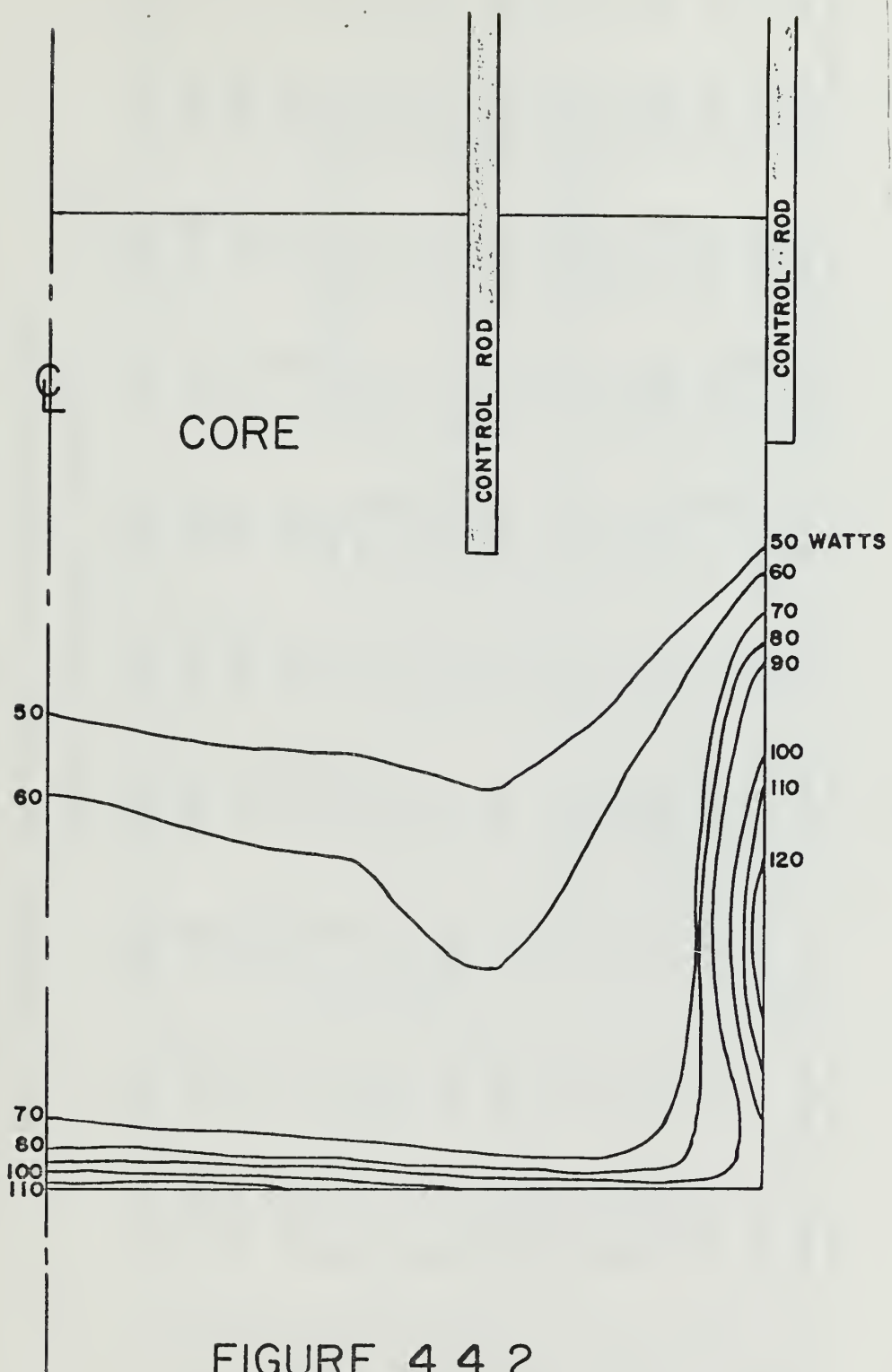


FIGURE 4.4.2

CORE POWER DISTRIBUTION (watts/cm<sup>3</sup>)



Table 4.4.2  
Power Generation (watts/cm<sup>3</sup>) at Core Mesh Points

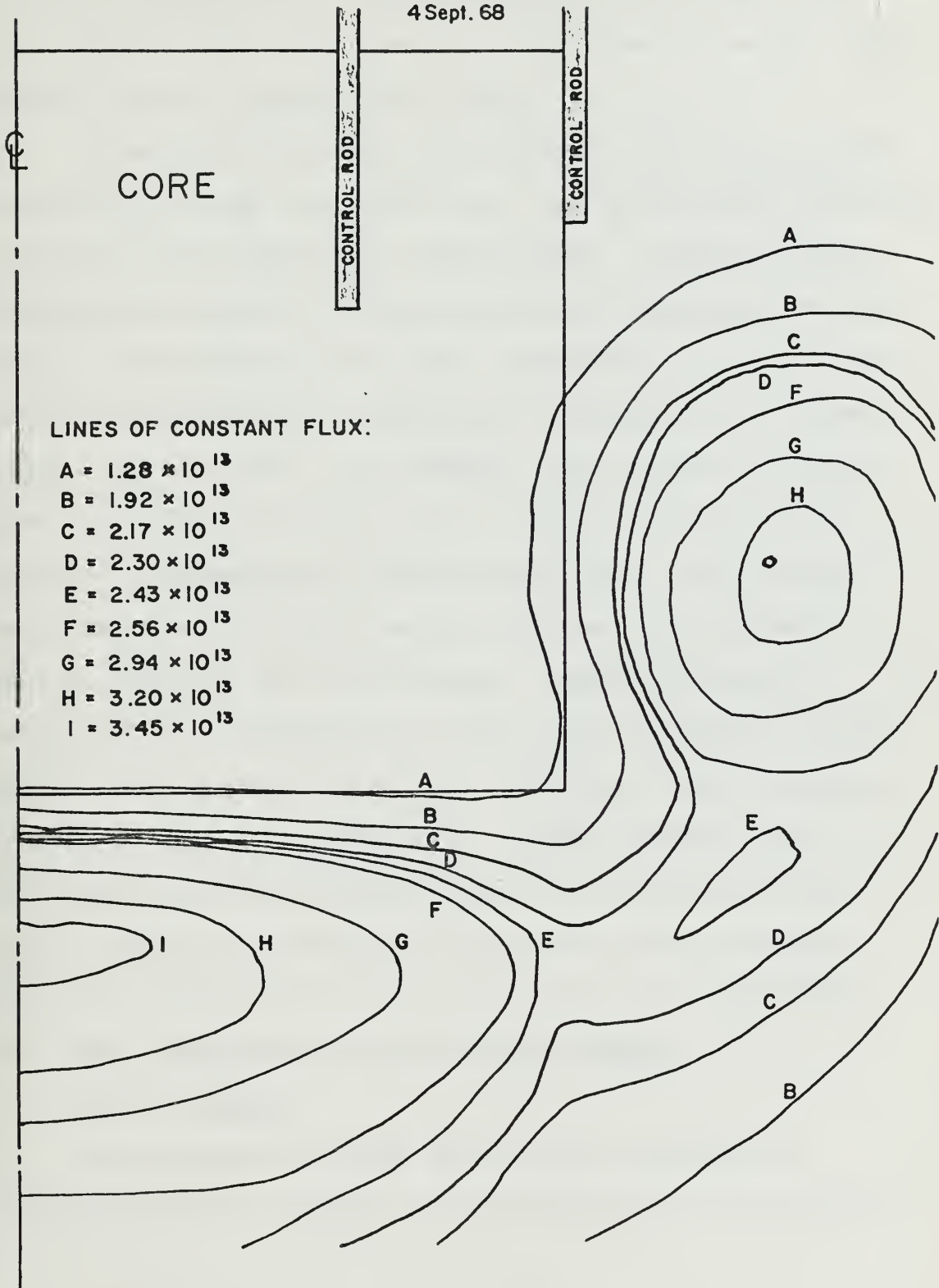
	Distance From Core Centerline → (cm)										
	2.0	6.0	10.0	14.0	15.0	19.0	21.0	23.0	24.0	24.010	
0.0	4.49	3.58	1.97	0.03	0.03	0.45	0.39	0.18	0.38	0.37	
7.5	4.47	3.62	2.05	0.09	0.08	0.72	0.64	0.31	0.08	0.08	
15.0	9.40	7.75	4.56	0.22	0.21	3.30	3.38	1.99	0.30	0.27	
22.5	20.54	17.77	11.68	1.58	1.71	19.27	29.77	44.90	56.40	56.55	
30.0	41.11	39.78	37.67	36.58	37.34	45.38	56.58	76.72	93.02	93.24	
37.5	57.63	56.47	54.67	53.7	54.30	61.08	73.31	96.54	115.80	116.10	
45.0	65.54	64.22	62.05	60.5	60.59	67.06	79.51	103.70	123.90	124.20	
50.0	65.93	64.54	62.19	60.30	60.60	66.16	78.12	101.60	121.30	121.60	
55.0	63.88	62.43	59.93	57.70	57.85	62.37	73.15	94.63	112.80	113.10	
57.5	64.18	52.65	59.98	57.40	57.40	60.90	70.60	90.38	107.30	107.60	
60.0	67.82	66.14	63.13	59.90	59.60	61.47	69.44	86.64	101.90	102.10	
62.5	79.95	77.90	74.12	69.60	68.85	67.83	72.86	85.55	97.86	98.08	
63.75	93.25	90.86	86.35	80.70	79.55	76.38	79.15	87.97	97.43	97.63	
65.0	113.90	111.00	105.40	98.15	96.45	90.52	90.54	94.20	98.48	98.63	
65.01	114.20	111.20	105.70	98.40	96.70	90.73	90.73	94.36	98.59	98.72	

Distance From Core Top (cm) ↓



FIGURE 4.4.3  
FLUX MAP

4 Sept. 68







Numerically integrating the power produced by a fuel element located on the outermost edge of the core over the height of the core yields a total power of watts produced in one of these "hot" plates.

In order to determine the hottest spot on the hottest plate in the High Flux MITR core, the axial power variation along the hot channel was investigated. In most reactor designs with upward flowing coolant the hot spot, or location of the maximum plate wall temperature, usually occurs a few centimeters above the point of maximum power generation. This is true, for instance, for reactors in which the axial flux distribution is a cosine function which peaks at the geometric center of the core. The maximum wall temperature occurs beyond the power peak primarily due to the fact that the coolant, coming in from the bottom at low temperatures, helps keep the bottom portion of the fuel element cooler than the top. Such considerations can also be applied when locating the hot spot in the High Flux MITR, and based upon these considerations we can expect to find the hot spot about 25 centimeters above the bottom of the core for phase one calculations.

#### 4.5 Wall Temperature Along Hottest Channel

##### 4.5.1 General

In arriving at values for the wall temperature along the hottest channel, it is assumed that the reactor



is operating at a state in which both the scram conditions for high coolant outlet temperature and for low coolant flow rate have been reached simultaneously.

#### 4.5.2 Formulation of Applicable Equation

To determine the magnitude of the wall temperature at various points along the hottest channel, one may proceed as follows. The temperature difference between the maximum wall temperature and the reactor inlet is made up of two parts. First is the film temperature drop, which is made up of the differences between the wall temperature and the average temperature of the coolant at that point in the channel,  $T_w - T_c$ . Second is the bulk coolant temperature drop, which is made up of the difference between the coolant temperature and the reactor inlet temperature,  $T_c - T_i$ . Denoting  $q_1/A$  as the specific heat flux at the point of interest and  $q_2$  as the total rate of heat transferred to the coolant from the channel entrance up to the point of interest, these temperature differences may be written as:

$$T_w - T_c = q_1/hA \quad (4.5.2.1)$$

$$T_c - T_i = q_2/W(ch)C_p(ch) \quad (4.5.2.2)$$

The symbols not already defined are:

$h$  = convective heat transfer coefficient

$W(ch)$  = mass flow rate of the coolant in the channel



$C_p(\text{ch})$  = specific heat evaluated at the average bulk temperature of the  $D_2O$  in the channel,  $\frac{T_i + T_o}{2}$

Adding Equations 4.51 and 4.52, one obtains an expression for the maximum wall temperature in terms of reactor inlet temperature, the specific heat flux at the point in question, and the total heat gained by the coolant from the channel entrance up to the point of calculation:

$$T_w = T_i + q_1/hA + q_2/W(\text{ch})C_p + \Delta T_{tm}, \quad (4.5.2.3)$$

( $\Delta T_{tm}$  is an allowance for error in temperature measurement, taken to be  $5^\circ\text{F}$ .) Following the arguments of DeVoto, it is more desirable that wall temperature calculations be based on reactor outlet temperature, which is recognized as an incompletely mixed bulk temperature, than on reactor inlet temperature as above. This is because the outlet temperature recorder is the first monitor encountered by the coolant after it leaves the core and hence is the logical place in the circuit to install the various alarm and scram circuits.

By considering the total heat removed by the coolant as it passes through the core of the High Flux MITR, an expression relating the reactor inlet temperature and the incompletely mixed reactor outlet temperature,  $T_o$ , may be obtained. Denoting  $q_r$  as the total heat rate in the



reactor core, the expression is:

$$q_r = W_t C_{p(r)}(T_o - T_i) \quad (4.5.2.4)$$

The symbol  $W_t$  refers to the total coolant mass flow rate in the reactor core, and  $C_{p(r)}$  is the specific heat of the  $D_2O$  evaluated at the reactor bulk temperature  $\frac{T_i + T_o}{2}$ . Solving this expression for  $T_i$ , and substituting the resulting expression into Equation (4.5.3) yields the result:

$$T_w = T_o + \frac{q_1}{hA} + \frac{q_2}{W(ch)C_p(ch)} - \frac{q_r}{W_t C_{p(r)}} + \Delta T_{tm} \quad (4.5.2.5)$$

#### 4.5.3 Heat Transfer Coefficient

The heat transfer coefficient,  $h$ , for turbulent flow in confined rectangular passages is calculated by means of the modified Colburn correlation (see references (22) and (23) for experimental verification of the use of the Colburn equation):

$$\frac{hDe}{K_f} = 0.023 \left[ \frac{DeV\rho}{\mu} \right]_f^{0.8} \left[ \frac{C_p u}{K} \right]_f^{0.3} \quad (4.5.3.1)$$

where

$h$  = heat transfer coefficient, BTU/hr-ft<sup>2</sup>°F

$De$  = equivalent diameter, 0.0188 ft.  $\left(\frac{4A}{P}\right)$

$K$  = thermal conductivity of the coolant, BTU/hr-ft°F,

Fig. (4.5.3.1)





$V$  = coolant velocity, 11530 ft/hr for flow rate of 1850 gpm.

$\rho$  = coolant density, lb/hr-ft, Fig. (4.5.3.2)

$\mu$  = coolant viscosity, lb/ft<sup>3</sup>, Fig. (4.5.3.1)

$C_p$  = specific heat, BTU/lb-°F, Fig. (4.5.3.2)

The subscript "f" means that the properties are evaluated at the film temperature. The film temperature is taken to be the average of the heat transfer surface temperature and the bulk water temperature,  $T_f = \frac{T_w + T_b}{2}$ .  $T_w$  has been previously defined, and  $T_b$  is the bulk temperature of the reactor coolant at the point of calculation. Equation (4.5.1.1) can be rewritten as:

$$h = \frac{0.023K_f}{De} \left[ \frac{W_t De}{\mu A_t} \right]_f^{0.8} \left[ \frac{\mu C_p}{K} \right]_f^{0.3} \quad (4.5.3.2)$$

Implicit in the above expression is the assumption that the coolant flow rate is the same for all channels, i.e.  $W_t/A_t = W_{ch}/A_{ch}$ . Hence, the Reynolds number will be the same whether defined for one interplate fuel element or the entire core. Heat transfer coefficient,  $h$ , is shown plotted versus film temperature in Figure (4.5.3.3) for a constant velocity through the core of 11530 ft/hr, which corresponds to a flow rate of 1850 gallons per minute at a bulk water temperature of 104°F. Taking a horizontal



FIGURE 4.5.3.1 VISCOSITY AND THERMAL CONDUCTIVITY OF HEAVY WATER AS A FUNCTION OF TEMPERATURE OF THE SATURATED LIQUID

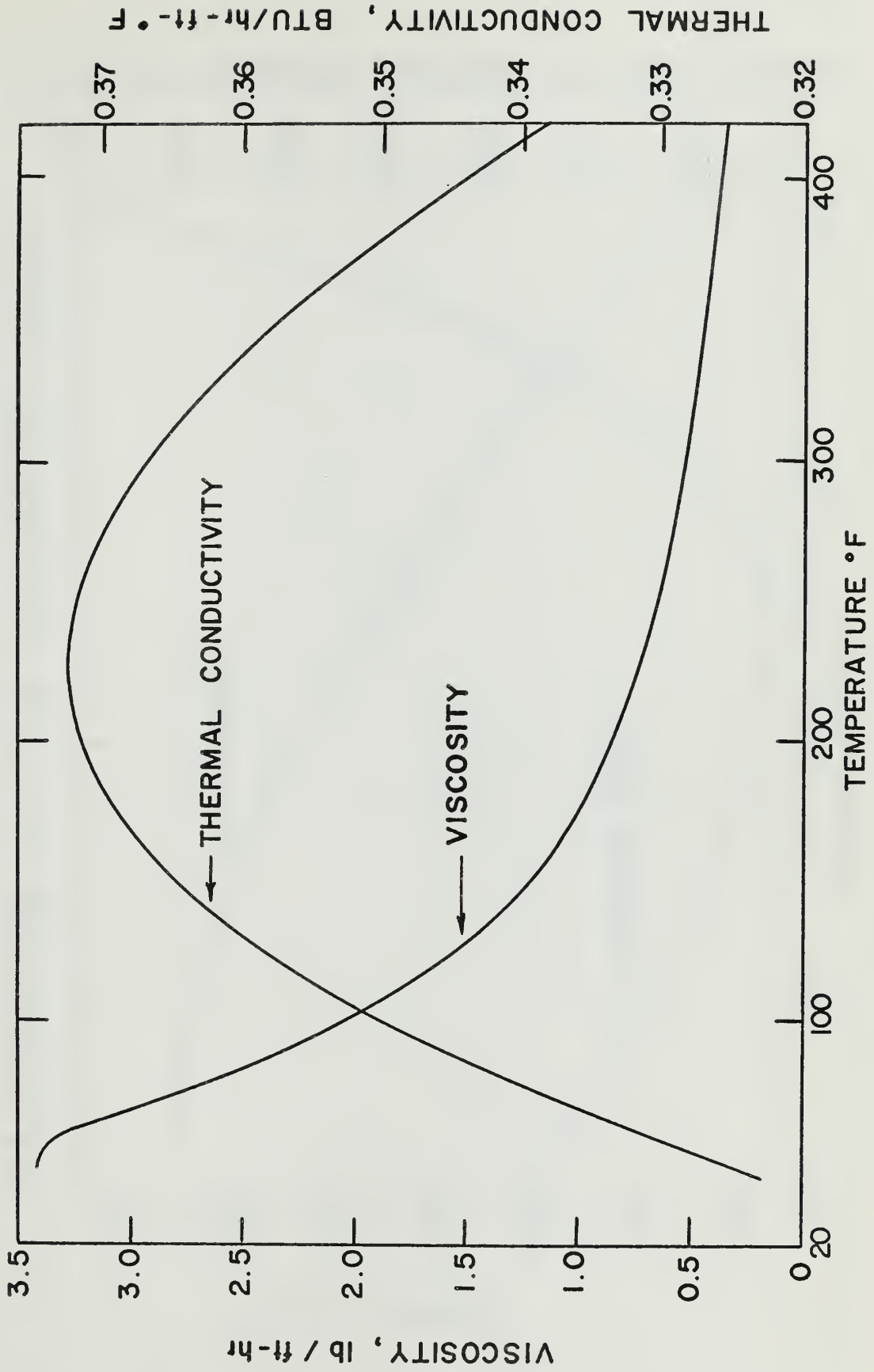




FIGURE 4.5.3.2 DENSITY AND SPECIFIC HEAT OF HEAVY WATER AS A FUNCTION OF TEMPERATURE OF THE SATURATED LIQUID

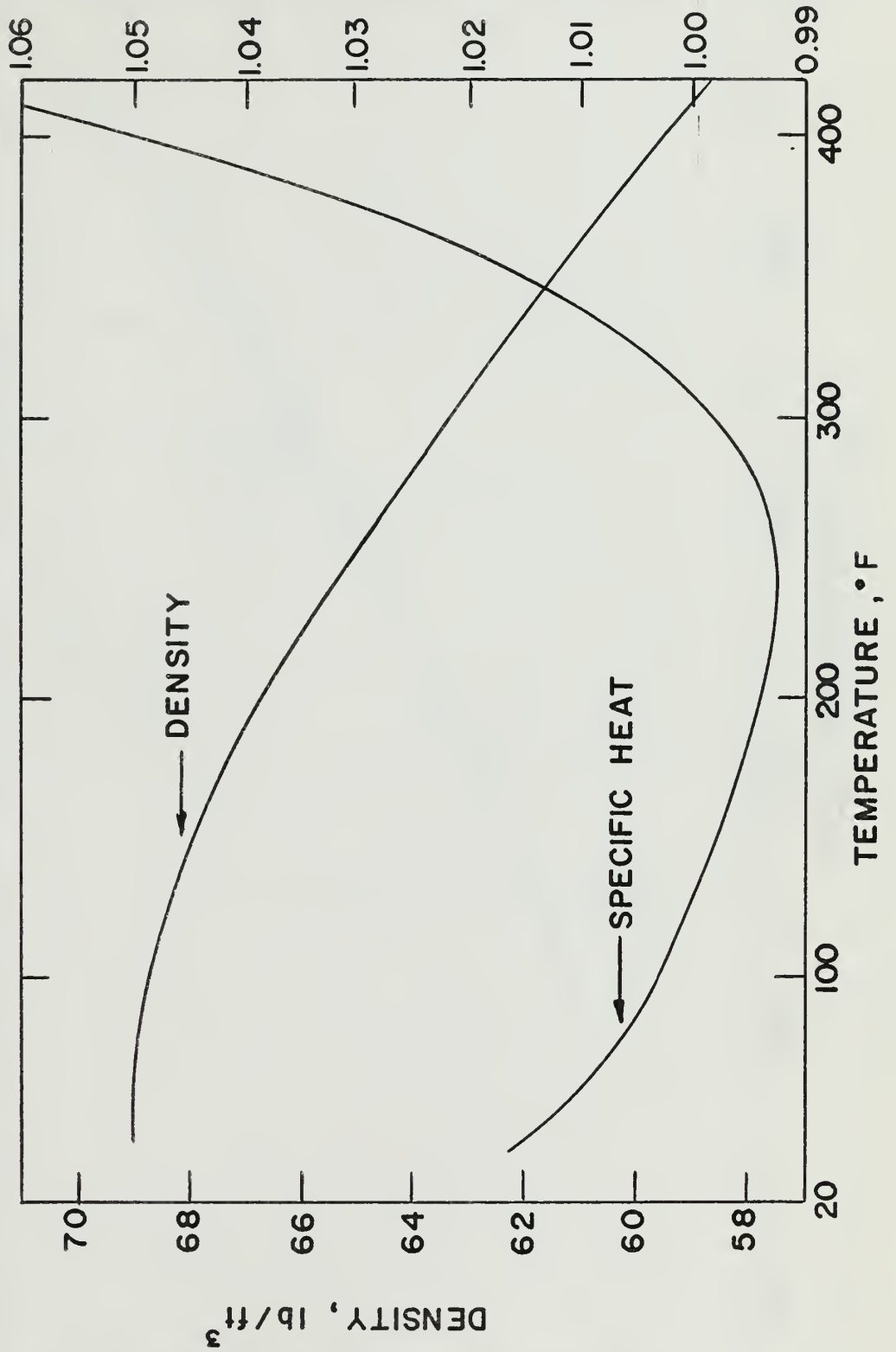
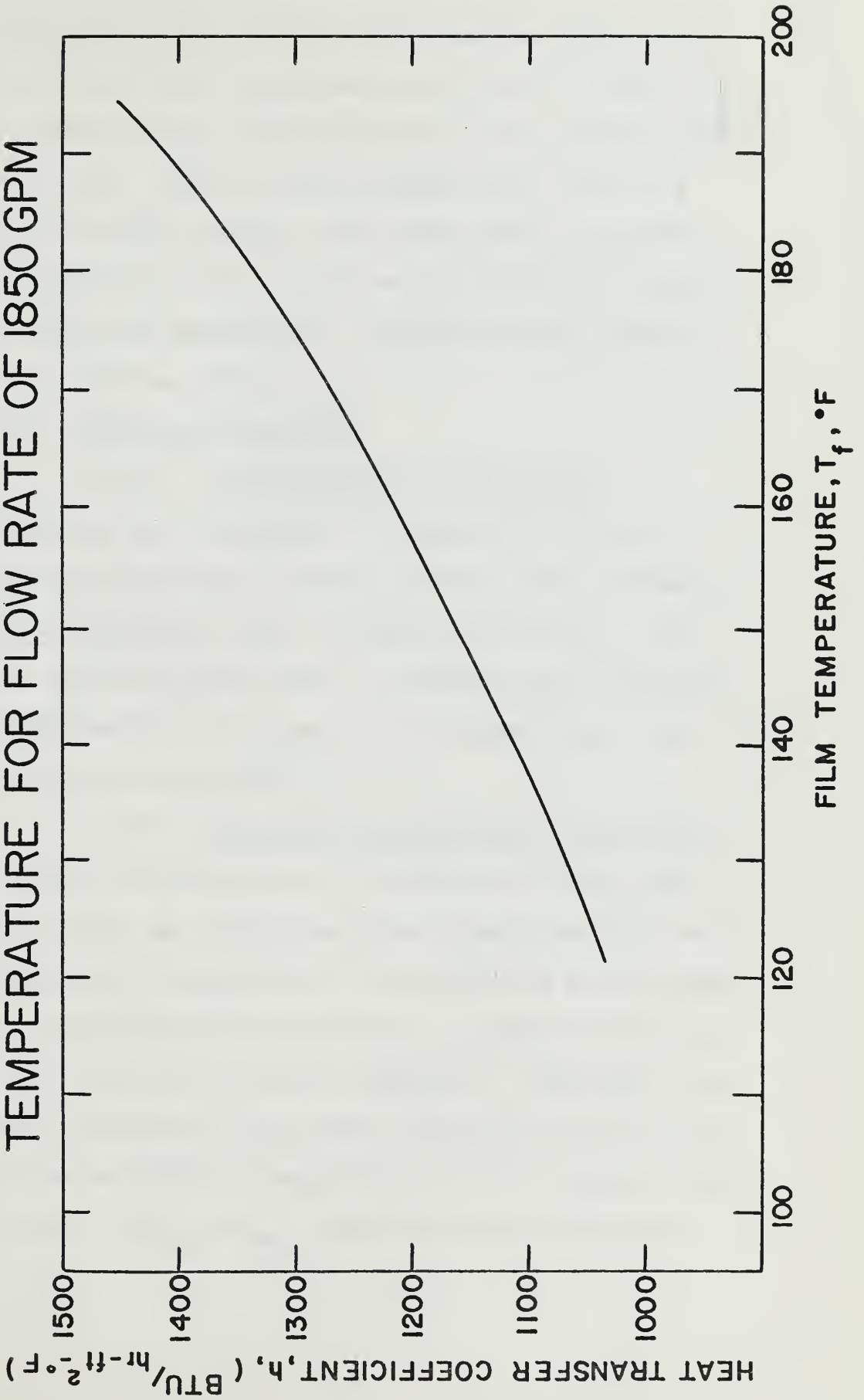




FIGURE 4.5.3.3

HEAT TRANSFER COEFFICIENT vs. FILM TEMPERATURE FOR FLOW RATE OF 1850 GPM







out through the core, coolant flow area was taken to be the entire core cross sectional area times the ratio of coolant channel cross sectional area to fuel plate cross sectional area. Taken as such coolant flow area is a conservative factor because flow area would be somewhat smaller than this in the actual core, thereby increasing flow velocity and consequently increasing heat transfer coefficient for the actual core.

#### 4.5.4 Limiting Parameters

##### 4.5.4.1 Reactor Outlet Temperature

Following the reasoning of Section III.3 of the Technical Specifications for the present MITR, the maximum outlet temperature,  $T_o$ , is taken to be  $55^{\circ}\text{C}$ . (The technical specifications quote a maximum outlet temperature of  $58^{\circ}\text{C}$  which is the audit and review level. The scram point was set at  $55^{\circ}\text{C}$ .)

##### 4.5.4.2 Maximum Allowable Wall Temperature

As stated in Section 3.1, in order to insure that the hottest spot on the hottest fuel plate does not reach  $450^{\circ}\text{C}$  under any circumstances, the criterion established is that cooling shall be sufficient to prohibit boiling of any type within the coolant channels. Therefore, the difference between the plate wall temperature at the hot spot and the saturation temperature of the coolant at the same location,  $T_{w_{\max}} - T_{\text{sat}}$ , must not be permitted to



reach the point of inception of nucleate boiling.

Several correlations are available which are designed to predict the amount of superheat necessary for the inception of nucleate (24,25) boiling. (See heat transfer texts by L.S. Tong or W.M. Rohsenow.) Three of these correlations are used in Section 4.5.3.4. However, such correlations are by no means exact and so for the purposes of determining the maximum allowable wall temperature it is prudent that we attempt to design our system such that we simply rely on the fact that boiling will not take place as long as the fuel plate wall temperature does not exceed the coolant saturation temperature at any point in the core. The top of the phase one design core is under 8 ft. of  $D_2O$ ; at this pressure the saturation temperature of the  $D_2O$  is  $223.5^{\circ}F$ .

#### 4.5.4.3 Coolant Flow Rate

Following arguments of Section III.2 of the technical specifications for the present MITR, the minimum allowable flow rate through the core of the High Flux MITR will be taken as 1850 gallons per minute.

#### 4.5.5 Calculations

Utilizing Equation 4.5.2.5, here repeated, wall temperature is calculated as a function of axial height above the core bottom for the hottest (outermost) fuel plate.



$$T_w = T_o + q_1/hA + q_2/w_{ch}C_{p,ch} - q_r/w_tC_{p,r} + \Delta T_m \quad (4.5.5.1)$$

The first calculation will be done in detail as a sample. For a point on the outermost fuel plate 10 centimeters above the bottom of the core:

$$T_o = 55^\circ\text{C} = 131^\circ\text{F}, \text{ a limiting condition by definition}$$

$$q_1 = F_q G_{q1} P(z=10)V$$

$$F_q = \text{heat flux hot channel factor} = 1.155$$

$$G_{q1} = \text{fraction of core power conducted through the fuel plates into the coolant} = 0.905$$

$$P(z=10) = \text{power produced per unit core volume} = 113.1 \text{ watts/cm}^3 \text{ (from Table 4.5.5.1)}$$

$$V = \text{volume of } 1/2 \text{ fuel plate plus } 1/2 \text{ coolant channel per unit axial dimension} = 1.60 \text{ cm}^3 \text{ (see Figure 4.5.5.1)}$$

$$A = \text{heat transfer area for one side of one plate per unit axial length} = 7.61 \text{ cm}^2 \text{ (see Figure 4.5.5.1)}$$

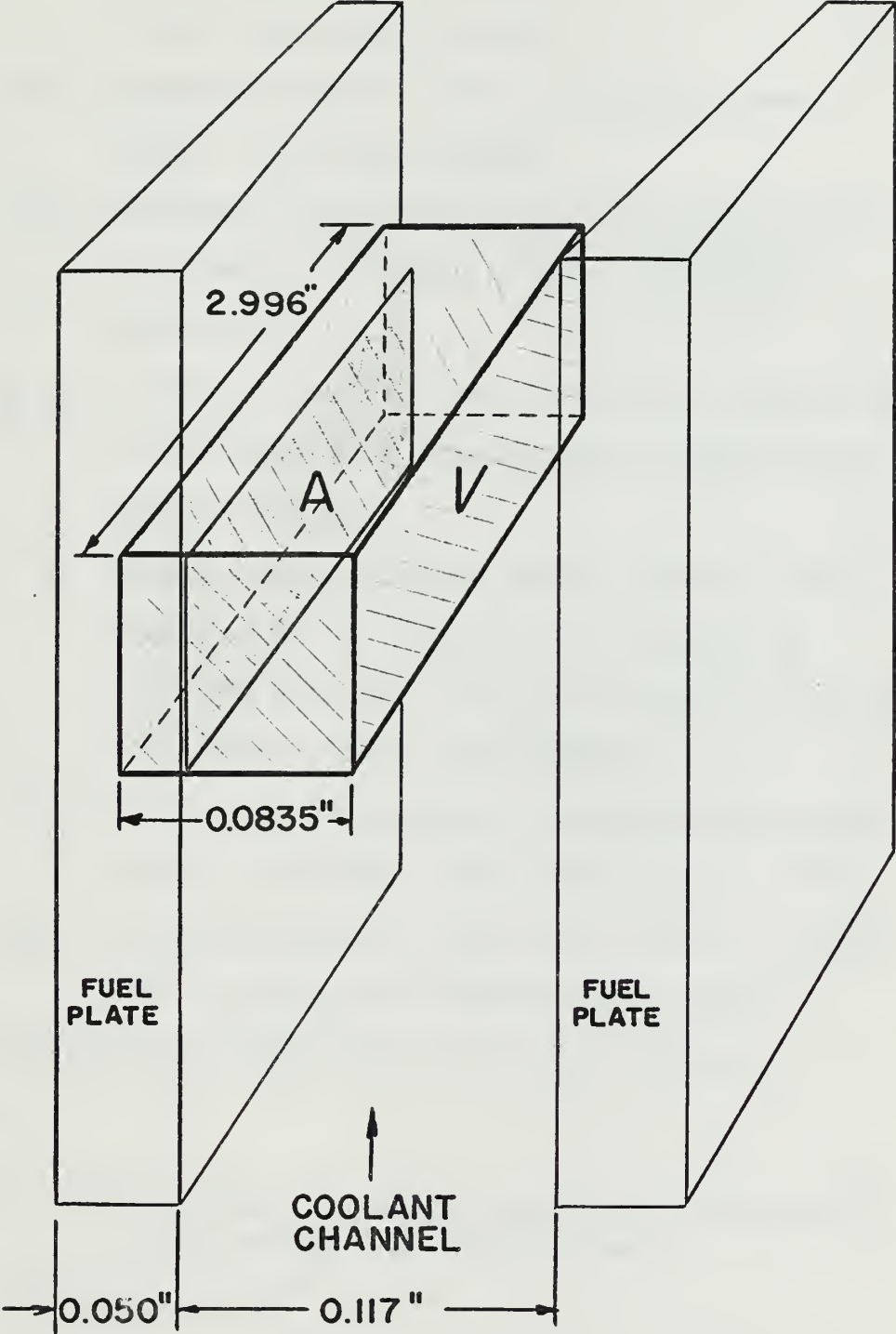
$$h = 1265 \text{ BTU/hr-ft}^2\text{-}^\circ\text{F} \text{ from Figure 4.5.3.5 for a film temperature of } 168^\circ\text{F}; F_h = 1.46 \text{ from Section 4.3.6}$$

$$q_2 = F_q G_{q2} \sum_{z=0}^{10} P(Z)V(Z)$$

$$G_{q2} = \text{fraction of core power carried off by the coolant as it passes through the core} = 0.926$$



FIGURE 4.5.5.1  
CORE VOLUME ELEMENT







$P(Z)$  = power produced per unit core volume at axial position  $Z$  in the hot channel; values taken from Table 4.5.5.1

$V(Z)$  = volume element of core producing power

$$P(Z) = V \times \text{mesh spacing}$$

$w_{ch}$  = one-half the coolant mass flow rate through one coolant channel =  $1/2w_t \frac{V(\text{channel})}{V(\text{core})} = 965 \text{ lb/hr}$

$C_{p,ch}$  = average specific heat in the hot channel up to the point of calculation = 0.9995 from Figure 4.5.3.4

$q_r$  = total power produced by the reactor which is removed by the coolant as it passes up through the core =  $(0.926) (5 \times 10^6) = 4.62 \times 10^6 \text{ watts} = 14.5 \times 10^6 \text{ BTU/hr}$

$W_t$  = total mass flow rate of coolant through the core = 1,020,000 lb/hr (1850 gpm at  $104^\circ\text{F}$ )

$C_{p,r}$  = average specific heat in the core = 1.0005 for a core bulk temperature of  $122^\circ\text{F}$

Substituting in the numerical values and solving:

$$q_1/hA =$$

$$\frac{(1.46)(1.155)(0.905)(3.412 \text{ BTU/hr-watt})(113.1 \text{ watts/cm}^3)}{(1265 \text{ BTU/hr-ft}^2\text{-}^\circ\text{F})(7.61 \text{ cm}^2)} \times$$

$$(1.60 \text{ cm}^3)(30.48 \text{ cm/ft})^2 = 91^\circ\text{F}$$



Table 4.5.5.1  
Power as a Function of Axial Position Along the Hot Channel

Distance (Z) Above Core Bottom (cm)	P(Z) (watts/cm <sup>2</sup> )	P(Z) x Mesh Spacing (watts/cm <sup>2</sup> )	Σ P(Z) x Mesh Spacing (watts/cm <sup>2</sup> )
0	98.72	0.99	
0.01	98.63	122.51	0.99
1.25	97.63	122.04	123.5
2.5	98.08	245.2	245.5
5.0	102.1	255.25	490.7
7.5	107.6	269.0	746.0
10.0	113.1	565.5	1015.0
15.0	121.6	608.0	1580.5
20.0	124.2	931.5	2188.5
27.5	116.1	870.75	3120.0
35.0	93.24	699.3	3990.7
42.5	56.55	424.13	4414.8
50.0	0.2748	2.06	4416.9
57.5	0.07846	0.59	4417.5
65.0	0.03706		



$$q_2/W_{ch} C_{p, ch} =$$

$$\frac{(1.375)(0.926)(3.412 \text{ BTU/hr-watt})(1015.0 \text{ watts/cm}^2)(1.60 \text{ cm}^2)}{(965 \text{ lb/hr})(0.9995 \text{ BTU/lb-}^\circ\text{F})}$$

$$= 7.3^\circ\text{F}$$

$$q_t/W_t C_{p, t} = \frac{(0.9237)(5 \times 10^6 \text{ watts})(3.412 \text{ BTU/hr-watt})}{(1.0005 \text{ BTU/lb-}^\circ\text{F})(1.02 \times 10^6 \text{ lb/hr})}$$

$$= 15.5^\circ\text{F} .$$

Hence,

$$T_w = 131 + 91 + 7.3 - 15.5 + 5 = 218.8^\circ\text{F} .$$

Repeating the above procedure for the other values of axial distance above the bottom of the core resulted in the values plotted on Figure 4.5.5.2. As shown on this figure, the maximum fuel plate wall temperature is  $231^\circ\text{F}$  and occurs about 23 centimeters above the base of the core. At this position in the core, the saturation temperature of the  $\text{D}_2\text{O}$  coolant is  $225.4^\circ\text{F}$ . Although the above calculated hot spot value is slightly above the coolant saturation temperature at that point, the amount of superheat is insufficient to cause boiling by calculation of any of the three correlations for the inception of nucleate boiling given in Tong, Boiling Heat Transfer and Two Phase Flow (25).

For the calculated values of heat flux, pressure, and saturation temperature at the position of the hot spot, the



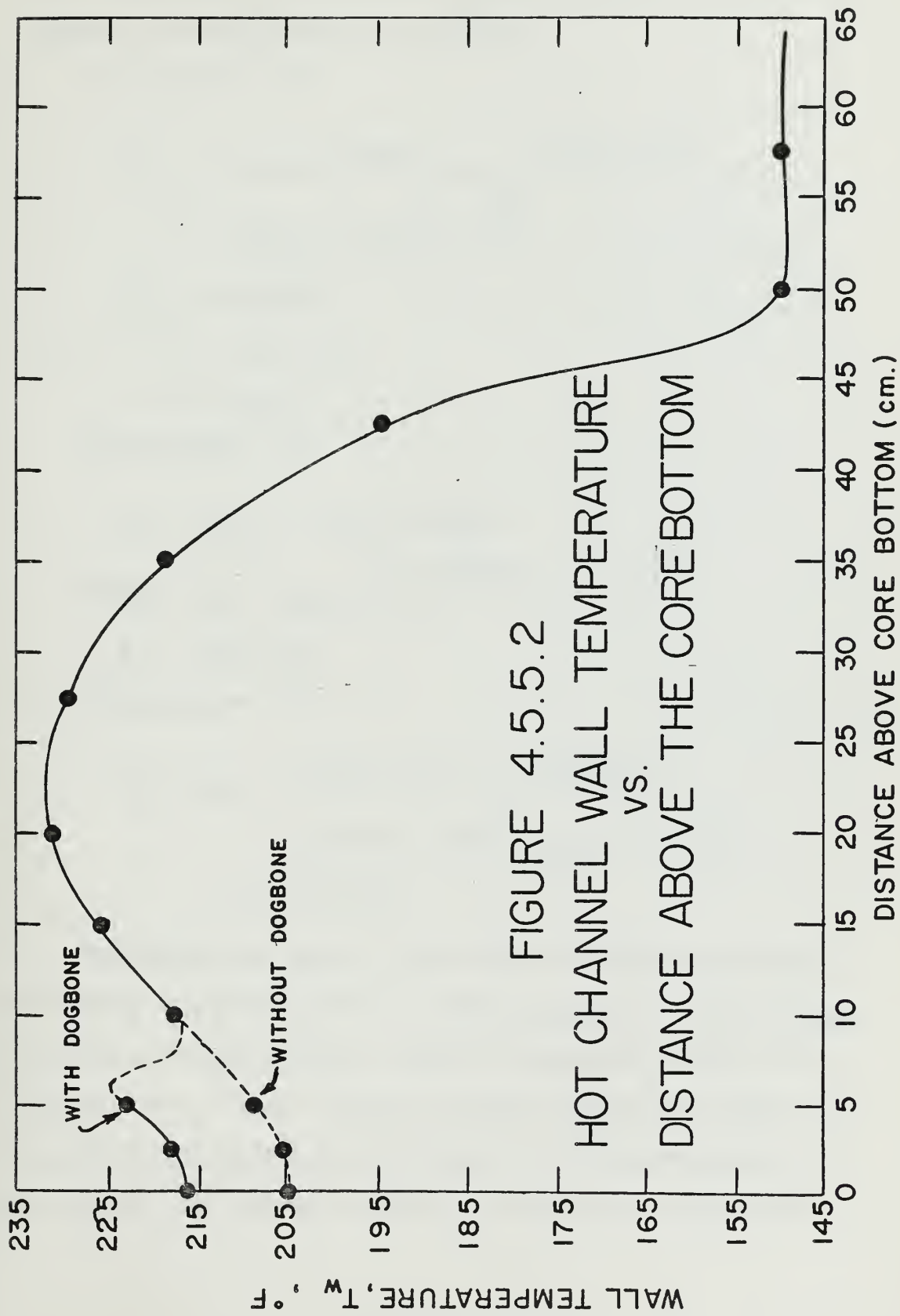


FIGURE 4.5.5.2  
HOT CHANNEL WALL TEMPERATURE  
VS.  
DISTANCE ABOVE THE CORE BOTTOM





wall temperature necessary to cause nucleate boiling to commence is calculated as follows:

Correlation (1),

$$q''_{LB} = 15.60 p^{1.156} (T_w - T_{sat})^{2.3/p^{0.0234}}$$

$$q'' = 124837.8 \text{ BTU/hr-ft}^2$$

$$T_{sat} = 225.6^\circ\text{F}$$

$$p = 19.17 \text{ psi}$$

$$T_w = 239.1^\circ\text{F}$$

Correlation (2),

$$T_{LB} = T_{sat} + \Delta T_{J+L} - q''/h$$

$$\Delta T_{J+L} = T_w - T_{sat} = 60 e^{P/900} (q''/10^6)^{1/4}$$

$$T_{LB} = 254.4^\circ\text{F}$$

Correlation (3),

$$\begin{aligned} T_w - T_{sat} &= 0.015 \times 10^6 (q''/10^6)^{1/4} \\ &= 12(500 - 0.707 T_{sat}) 10^{-6} \text{ lb/ft} \end{aligned}$$

$$T_w = 262.0^\circ\text{F}$$

Consequently, even if one were to abide by the requirement of Section 4.5.3.2 that  $T_{w,max}$  not exceed  $T_{sat}$ , only minor modifications would be required to the fluid flow system. Since the main coolant pumps are capable of supplying approximately 2100 gpm of  $D_2O$  through the core one could, for example, simply redefine the scram point



flow rate to be 2000 gpm. In addition, one might re-define the outlet temperature scram point to be  $53^{\circ}\text{C}$ . The combined effect of redefining scram point flow rate and outlet temperature would be to reduce  $T_{w,\text{max}}$  by approximately  $8^{\circ}\text{F}$ , more than enough to reduce  $T_{w,\text{max}}$  below  $T_{\text{sat}}$ . Preliminary calculations, therefore, have indicated that fluid flow and heat transfer would not pose a major design problem.

#### 4.5.6 Revised Data

As Andrews Addae began to obtain reliable results from his phase I core physics calculations, one fact became very clear: the maximum core power density would be much higher than the values used in the calculations of the preceding section. Best estimates indicated a maximum homogenized core power density of approximately  $320 \text{ watts/cm}^3$ , a factor of 2.5 greater than the maximum power density computed in Section 3.4. It should be noted that the computer code used by Mr. Addae in his calculations is based on diffusion theory, and as such values of power density near the edge of the core where the power density gradient is steep are only approximate. Since the film temperature rise term,  $q_1/hA$ , is the dominant term in the calculation of fuel plate wall temperature (Equation 4.5.2.5), it was clear that to a



first approximation one is faced with the necessity of increasing the magnitude of the product "hA" by a factor of approximately 2.5 for the Phase I design.

#### 4.6 Phase I vs Phase II

With respect to heat transfer, the major difference between the phase I and phase II core configurations is that the phase II configuration is much smaller. The power distribution in the two cores is very similar. For a constant mass flow rate, the flow velocity through the phase II core is a factor of 2.1 greater than that through the phase I core, which increases the heat transfer coefficient by a factor of 1.81. Partially offsetting this advantage is the fact that the maximum power density in the phase II core is a factor of 1.3 greater than that for the phase I core. The combined effect is that for the light water cooled core, instead of the factor of 2.5 augmentation in heat transfer required by Section 4.5.6, one must augment heat transfer by a factor of  $\frac{1.3}{1.81}(2.5) = 1.8$ . Maximum power density for the phase II core occurs along the bottom edge of the core.

In addition to being smaller, the column of water above the phase II core is 3 ft. higher than that above the phase I core. The additional head of water increases the coolant saturation temperature by about 5°F, thus making it conservative to use estimates based on phase I calculations to develop a phase II heat removal analysis.



## Chapter 5

## AUGMENTATION OF FUEL PLATE HEAT REMOVAL

5.1 General

Results of core physics calculations being performed by Mr. A. Addae (21), together with the results of the preliminary heat transfer calculations performed in the previous chapter of this thesis, have indicated that the product "hA" must be increased by a factor of approximately 2.5 (Phase I) or 1.8 (Phase II) in order to provide adequate heat removal from the High Flux MITR core. It is the purpose of the paragraphs which follow to explore the various means by which the product "hA" may be increased, and to experimentally verify any conclusions reached.

5.2 Methods of Increasing the Product "hA"5.2.1 Decreased Fuel Plate Spacing

The fuel plates in the present MITR are spaced so as to allow a coolant channel width of 0.117 inches. A survey of research reactors utilizing flat plate MITR-type fuel elements has revealed no parameter which would prevent plate spacing from being decreased. The narrowest flow channel discovered was the 0.050 inch channel between the fuel plates of the Oak Ridge High Flux Isotope Reactor (22). For a rectangular channel with high aspect ratio, decreasing the fuel plate spacing causes a proportional decrease in the effective channel diameter and increase in flow velocity. Taking the McAdams correlation for heat transfer





coefficient as typical of the several available,

$$\frac{hD_e}{K_b} = 0.023 \left( \frac{\rho V D_e}{\mu_b} \right)^{0.8} \left( \frac{\mu C_p}{K_b} \right)^{0.4}, \quad (5.2.1.1)$$

it is seen that for a constant mass flow rate the decrease in equivalent channel diameter and corresponding increase in flow velocity cancel each other, thus leaving the Reynolds number unchanged. As a result the Nusselt number remains unchanged, which in turn requires that the magnitude of the heat transfer coefficient  $h$  increase in direct proportion to the decrease in flow channel equivalent diameter. (Equivalent diameter is calculated for rectangular channels using the standard equation  $D_e =$

$\frac{4 \times \text{cross sectional area}}{\text{wetted perimeter}}$ .) Therefore, if one were to decrease the coolant channel width from the present 0.117 inch to 0.090 inch, one could expect the heat transfer coefficient to be increased by a factor of 1.3. (Note: A 0.090" coolant channel width was assumed for all Phase II calculations.)

### 5.2.2 Increased Mass Flow Rate

Increasing the mass flow rate of coolant through the core results in a proportional increase in flow velocity through the core. Referring to Eq. 5.2.1.1 it is seen that the heat transfer coefficient is proportional to velocity to the 0.8 power. If one were to add a third main



coolant pump, thereby increasing the flow velocity by approximately 50%, one could expect the heat transfer coefficient to be increased by a factor of 1.38.

When an increase in mass flow rate is contemplated, one must also investigate the associated increase in pressure loss around the primary coolant circuit.

$$\Delta P = 2f \frac{L}{D} \frac{V^2}{2} \text{ ft. of H}_2\text{O} \quad (5.2.2.1)$$

As shown by Eq. 5.2.2.1, pressure loss varies with the square of the flow velocity. Consequently, for a 50% increase in flow velocity one could expect pressure losses to increase by a factor of 2.25. In the present MITR the pressure loss through the core is on the order of 0.3 feet of H<sub>2</sub>O (2). From Eq. 5.2.2.1, pressure loss through the 8-inch piping is calculated to be approximately 0.07 feet of H<sub>2</sub>O per foot of pipe. Since each main coolant pump has a capacity for providing a pressure head of 46 psi while pumping 1000 gpm, it is seen that neither the pressure loss through the core nor the pressure loss through the 8-inch piping would prevent a 50% increase in flow velocity. However, the pressure loss through the heat exchangers is approximately 15 psi. Consequently, if one were to add an additional main coolant pump to increase flow velocity, an additional heat exchanger may be required to limit the pressure loss across the heat exchangers.



In summary, the extensive equipment modifications and additions necessary to obtain a 50% increase in flow velocity would be a high price to pay for a factor of 1.38 increase in heat transfer coefficient.

### 5.2.3 Modifications to Fuel Plates

The various methods currently available to augment convective heat transfer have been summarized in a paper by Dr. A.E. Bergles (27). Dr. Bergles has grouped the augmentive techniques available into the categories of surface promoters, displaced promoters, vortex flow, heated surface vibration, fluid vibration, electrostatic fields, and additives. Of these categories, all except surface promoters and vortex flow can be immediately discarded as not being feasible due to the nature of the MITR core heat transfer problem. The idea of using some type of twisted tape insert in order to generate swirl flow (vortex flow) in the coolant channel was seriously considered. However, the concept was finally discarded due to serious doubt as to the effectiveness of a swirl generator in a narrow rectangular channel of high aspect ratio, and due to the possible danger of a tape breaking loose and blocking the coolant flow through a channel. The only applicable method by which the product "hA" can be increased is, therefore, by modification of the fuel plate surface.



Unfortunately, reference (1) compares the various means of augmenting heat transfer as found in the literature with the corresponding unaugmented case based on maintaining constant pumping power. For the case of coolant flowing through the MITR core, pressure loss through the core appears to be of minor concern. Consequently, a comparison of heat transfer data based on constant mass flow rate is desired. The results of a literature search for data reporting the effect of various types of surface promoters is presented in the following section.

### 5.3 Literature Search

#### 5.3.1 General

Table 5.3.1.1 was taken primarily from reference (1) and lists the various experimental investigations of artificial roughness. One fact stands out clearly; there is no data for water cooled thin rectangular plates. Results of investigations which most nearly approximate the situation in the MITR core are presented below. No attempt at completeness is made here. The original papers should be consulted if detailed information is desired.

#### 5.3.2 Brouillette, Mifflin, and Myers

The authors' purpose was to determine the effect of a type of internal fin on the heat transmission and pressure drop characteristics of water flowing through copper tubing. The fins were produced by cutting 60-degree,







Table 5.3.1.1

EXPERIMENTAL INVESTIGATIONS OF ARTIFICIAL ROUGHNESS -  
NONBOILING HEAT TRANSFER AND FRICTION

<u>Investigators</u>	<u>Description</u>
Cope	Cooling of water; internally knurled tubes
Sams	Heating of air at high $\Delta T$ ; square threads inside tubes
Kolar	Heating of water and air; internally threaded tubes
Lancet	Heating of air; rectangular channel with machined roughness
Dipprey and Sabersky	Heating of water; sand-grain type roughness in tubes
Nunner	Heating of air; rings of various cross section inserted inside tubes
Koch	Heating of air; axially supported rings inserted inside tube
Nagaoka and Watanabe	Heating of water; wire coils inside tubes
Sams	Heating of air; wire coils inside tubes
Kreith and Margolis	Heating of water and air; tubes with wire-coil inserts
Boelter et al.	Heating of air; rectangular duct, one surface heated, with transverse strips
Edwards and Sheriff	Heating of air; rectangular channel, one surface heated lined with wire
Kemeny and Cyphers	Heating of water; annulus, inner heated surface with spiral grooves or protrusions



Table 5.3.1.1

(Continued)

<u>Investigators</u>	<u>Description</u>
Brauer	Heating of water; annulus; inner heated surface with grooves
Bennett and Kearsey	Heating of superheated steam; annulus, inner tube heated with grooves
Brouillette, Mifflin, and Myers	Heating of water; tubes with internal V-shaped fins
Durant et al.	Heating of water; annulus, inner heated tube with diamond knurls
Wilkie	Heating of air; annulus, inner tube with square or rectangular protrusions
Sheriff and Gumley	Heating of air; annulus, inner heated tube with coiled wires
Kjellstrom and Larsson	Heating of air; annulus, inner heated tube with various protrusions
Draycott and Lawther	Heating of air; annuli and tube bundles with threads, knurls, and coiled wires
Kattchee and Mackewicz	Heating of nitrogen (water for friction tests); wire coils outside rods in a bundle
Sutherland	Heating of air; wire coils outside rods in a bundle



Nunner correlated his data for Reynolds numbers ranging from  $10^3$  to  $10^5$  with the result:

$$\text{Nu} = \frac{f/8 \text{ RePr}}{1 + \frac{1.5}{\text{Re}^{1/8} \text{Pr}^{1/6} \left( \text{Pr} \frac{f}{f_0} - 1 \right)}} ; \quad (5.3.3.1)$$

where  $f$  is the Darcy friction factor ( $f_D = 2 \frac{\Delta P}{l} \cdot \frac{d}{\rho V^2}$ ) for the rough surface and  $f$  is the smooth tube friction factor. Equivalent diameter for all rough tube calculations is taken to be the volumetric mean diameter,  $d = \sqrt{\frac{4V}{\pi L}}$ .

Nunner's data indicated that the larger the  $\epsilon/d$  ratio the greater was the increase in heat transfer coefficient. His data also indicated that the optimum value of the ratio  $\epsilon/L$ , where  $\epsilon$  is the height of the ring insert and  $L$  is the center-to-center spacing of the insert in the tube, is approximately 10. However, since the manually installed ring inserts in Nunner's experiment may not have been perfectly seated against the tube wall, the effect of increasing the number of ring inserts per inch of tube length may have been to decrease (or at least fail to increase) the effective area available for heat transfer. Consequently, it is not possible to predict the optimum fin spacing distance based on the results of Nunner's work. Nunner's work did indicate, however, that ring inserts were capable



V-shaped notches on the inner surface of five specimens of tubing. The number of notches or fins was varied from 8 to 32 per inch of length and the ratio of fin height to tube diameter ranged from 0.009 to 0.050 inch. Data was taken for Reynolds numbers ranging from  $1.5 \times 10^4$  to  $2 \times 10^5$ . Table 5.3.2.1 below summarizes the results obtained. In addition, the authors stated that fin height has a greater effect in increasing the heat transfer coefficient than the number of fins.

Table 5.3.2.1

Tube No.	$\frac{\epsilon}{d}$	$\frac{hA(\text{fin})}{hA(\text{smooth})}$	$\frac{A(\text{fin})}{A(\text{smooth})}$	$\frac{h(\text{fin})}{h(\text{smooth})}$
1	0.009	1.18	1.33	0.89
2	0.013	1.08	1.18	0.91
3	0.017	1.55	1.48	1.04
4	0.027	1.90	1.44	1.32
5	0.050	2.48	1.48	1.68

### 5.3.3 Nunner

Nunner investigated the effect of various sizes, shapes, and densities of ring inserts on heat transfer coefficient and friction factor for air flowing through a 50 mm diameter brass tube. Both round and rectangular springy split rings were manually inserted into the tube at equal distances apart to serve as roughness elements.





of increasing the Nusselt number for air flowing in a cylindrical duct by nearly a factor of three.

#### 5.3.4 Kolar

Kolar analyzed the mechanism of heat transfer for both air and water flowing through smooth and rough tubes. Internal tube roughness was formed by machining a 60° triangular thread into the tube. The smooth tube was 26 mm in diameter and the rough tube thread depth varied from 0.5 to 1.5 mm. Kolar's smooth tube data fit the standard Dittus-Boelter correlation;

$$\text{Nu} = 0.023 \text{Re}^{0.8} \text{Pr}^{0.4}. \quad (5.3.4.1)$$

In order to correlate his rough tube data Kolar proposed a relation in the same form as the Dittus-Boelter equation for smooth surfaces:

$$\text{Nu} = 0.0517 \text{Re}_f \text{Pr}^{0.5}, \quad (5.3.4.2)$$

where  $\text{Re}_f$  is the Reynolds number defined by the friction velocity,

$$u_f = u_m \sqrt{f/8},$$

wherein  $u_m$  is the mean velocity and  $u_f$  is the friction velocity. Kolar shows that his data is in general agreement with that of Nunner and also with that of Cope (30). (Cope's data was for water flowing in circular tubes with the inside surface roughened by knurling) Reynolds number



was varied from 4500 to 145,000 and Prandtl number from 0.71 to 5.52. Unfortunately, Kolar makes no mention of the fin effect and what influence this effect might have on the rate of heat transfer.

### 5.3.5 Lancet

Lancet investigated the effect of a knurled surface on the heat transfer coefficient for air flowing through a small rectangular duct. The rough tube was 4.5 inches long and the maximum width and height were 0.145 in. and 0.045 in., respectively. The diamond-shaped protrusions were approximately 0.010 in. x 0.010 in. x 0.010 in. and were spaced approximately 0.010 in. apart leaving an open duct area of 0.025 in. x 0.125 in. For a constant Reynolds number in the range  $3110 < Re < 26900$ , Lancet found that the Nusselt number was increased by about a factor of two. Lancet's data is fit quite well by Nunner's relation for Nusselt number, Eq. 2.3.1, but even better by  $Nu = 0.042 Re^{0.8} Pr^{1/3}$ . The fin effect is not mentioned in Lancet's results.

Lancet's results for a smooth rectangular channel were found to fit the Colburn equation for smooth round ducts:

$$Nu = 0.023 Re^{0.8} Pr^{1/3} \quad (5.3.5.1)$$

### 5.3.6 Conclusions

From the literature survey, it is apparent that the increase in heat transfer from a surface roughened duct is



proportional to the increase in the duct roughness ratio,  $\epsilon/d$ . When correlating cylindrical tube data, the equivalent diameter,  $d$ , is taken to be a volumetric mean diameter defined as  $d = \sqrt{\frac{4V}{\pi L}}$ . When attempting to apply the results of experiments performed on cylindrical tubes in order to predict the effect of roughness on rectangular ducts of high aspect ratio, it is not clear how equivalent diameter should be defined. (Aspect ratio is the ratio of width to height of a rectangular channel.) When applying smooth tube correlations such as those of McAdams or Colburn to rectangular ducts equivalent diameter is taken to be  $d = \frac{4 \times \text{cross sectional area}}{\text{wetted perimeter}} (\frac{4A}{P})$ . Synan, however, has shown that the rough rectangular channel data of Lancet is best correlated with the data of other investigators by using the volumetric mean diameter,  $d = \sqrt{\frac{4V}{\pi L}}$ , as the equivalent diameter (35). It should be noted, though, that the aspect ratio for Lancet's rectangular ducts was only 5 : 1. For a MITR coolant channel, the aspect ratio is approximately 28 : 1, a considerable difference.

For the proposed MITR coolant channel shown in Figure 5.4.2.1,

$$d_1 = \frac{4A}{P} = 0.174 \text{ in.} \quad ; \quad \frac{\epsilon}{d} = 0.115$$

$$d_2 = \frac{4V}{\pi L} = 0.496 \text{ in.} \quad ; \quad \frac{\epsilon}{d} = 0.04$$



Since it has been concluded that the increase in heat transfer is proportional to the roughness ratio,  $\epsilon/d$ , utilization of the correct value of  $d$  is imperative if one is to predict rectangular duct heat transfer coefficients based on cylindrical tube experiments. From reference (35) one would be tempted to make the rectangular-cylindrical comparison based on  $d = \sqrt{4V/\pi L}$ . However, using the volumetric equivalent diameter implies that the increase in heat transfer due to roughness will vary with the width of the rectangular channel. For example, for a given roughness,  $\epsilon$ , a 3-inch wide thin rectangular channel would have a smaller  $\epsilon/d$  ratio than a 2 1/2 inch wide rectangular channel, and thus a lower Nusselt number. This is obviously not correct. It would appear, therefore, that for an artificially roughened thin rectangular channel with high aspect ratio, the correct equivalent diameter lies somewhere between  $4A/P$  and  $\sqrt{4V/\pi L}$ . Using the pessimistic,  $\sqrt{4V/\pi L}$ , equivalent diameter, the heat transfer coefficient for the channel of Figure 5.4.2.1 can be estimated (using the same velocity and temperature conditions as in Section 4.5.3):

$d$ (in.)	$\frac{\epsilon}{d}$	$h_{DB}$ (Dittus-Boelter)	$h_K$ (Kolar)	$h_N$ (Nunner)	Area Increase Due to Fins	$\frac{h_K}{h_{DB}}$
0.496	0.04	1360	2520	2270	1.67	1.83





On the basis of these estimated values it can be concluded that the finned channel of Figure 5.4.2.1 will provide at least a factor of 1.5 increase in heat transfer over an equivalent smooth channel. The heat transfer augmentation may, however, be greater than a factor of 1.5, possibly as much as a factor of 3 or 4.

## 5.4 Experimental Program

### 5.4.1 General

Based on the literature survey of the previous section, it was apparent that heat transfer from artificially roughened cylindrical tubes is at least partially understood by correlation of roughness ratios,  $\epsilon/d$ . However, it was not clear how one should apply the results of rough tube experiments to predict rough rectangular channel heat transfer. An experiment which would duplicate as nearly as possible the conditions which will exist in the High Flux MITR core was clearly desirable.

### 5.4.2 Coolant Channels

After making a brief survey of the methods available to heat the walls of a test section coolant channel, it was decided to heat the coolant channel by passing an electrical current through the channel walls. As described in Section 5.4.3.2 the heat transfer laboratory power supply is capable of supplying 3000 amperes at 24 volts. Consequently, if the test section is to take full advantage of the power supply available, it should provide a resistance



of  $8 \times 10^{-3}$  ohms. Since,

$$R = \frac{\rho L}{A} \quad (5.4.2.1)$$

where  $R$  = resistance (ohms)

$L$  = channel length (cm), and

$A$  = cross sectional area for current flow ( $\text{cm}^2$ ),

$\rho$  = resistivity (ohm-cm)

there are three parameters which can be adjusted in order to obtain a correct resistance value. A stainless steel channel wall 2.5 inches wide by 0.020 inches thick was decided upon. For stainless steel of these dimensions, a coolant channel wall electrical resistance of  $6.8 \times 10^{-3}$  ohms was calculated. Maximum power input into the coolant channel was therefore estimated to be 61,200 watts, which will provide a maximum heat flux into the coolant flowing through the channel of  $2.5 \times 10^5 \frac{\text{BTU}}{\text{hr-ft}^2}$ .

In order to provide a basis for future comparison, the first channel to be constructed and tested was a smooth surface rectangular duct. A flat piece of 0.020 inch thick stainless steel was folded three times to form a rectangular channel with inside dimensions of 2.5" x 0.090". The channel was closed by a single weld which ran the entire length of the coolant channel. It was expected that test results obtained from this channel would agree fairly well with existing smooth tube correlations,



such as those of Colburn or McAdams.

The second channel constructed was designed to provide a "proof of principle" for internally roughened rectangular ducts. It was decided to mill fins into the stainless steel channel wall in preference to other means of wall roughening (such as knurling) for the rough wall run because, (1) the increase in heat transfer due to heat transfer surface area versus that due to increased turbulence could be accurately separated, and (2) the process was one which was within the immediate capability of shop equipment and personnel.

Fin height was chosen to be 0.020 inches based on the philosophy that in the High Flux MITR no point of two fuel plates should be closer than the smallest existing separation of reactor fuel plates, the 0.050 inch separation of the Oak Ridge High Flux Isotope Reactor fuel plates. The projection of opposing 0.020 inch fins into a coolant channel whose unfinned width was 0.090 inches results in a minimum spacing of 0.050 inches. Fin width was taken to be 0.020 inches in order to provide the fins with structural stability and to prevent the machining problems which would accompany the milling of very narrow fins. Fin spacing was a compromise, and in fact, somewhat arbitrary. From Nunner's work (Section 5.3.3) the optimum fin spacing to fin height ratio appears to be 10 : 1, which



would require a fin spacing of 0.200 inches for a 0.020 inch fin. However, from the work of Brouillette, Mifflin, and Myers it appears as though the optimum arrangement is to have fins spaced as close together as possible. It is this author's opinion that the manually inserted rings of Nunner's experiment are not capable of providing data on which to base conclusions concerning optimum fin spacing. It is felt that heat transfer will be increased by spacing fins close together due to the greater heat transfer area increase over widely spaced fins. However, there must exist some minimum spacing beyond which fluid circulation between fins will be hindered and boiling in the inter-fin spaces will be caused to occur. With the above information in mind, a fin spacing of 0.040 inches was chosen. The optimization of fin spacing might well be the object of future experiments.

Rectangular grooves 0.040 inches wide, 0.020 inches deep, and spaced 0.020 inches apart were milled cross-wise three at a time into a flat piece of stainless steel. Two grooves 0.100 inch wide were then milled lengthwise into the stainless steel plate at positions which were to become the channel edges. The stainless steel plate was next folded into a rectangular channel and welded as with the smooth channel.







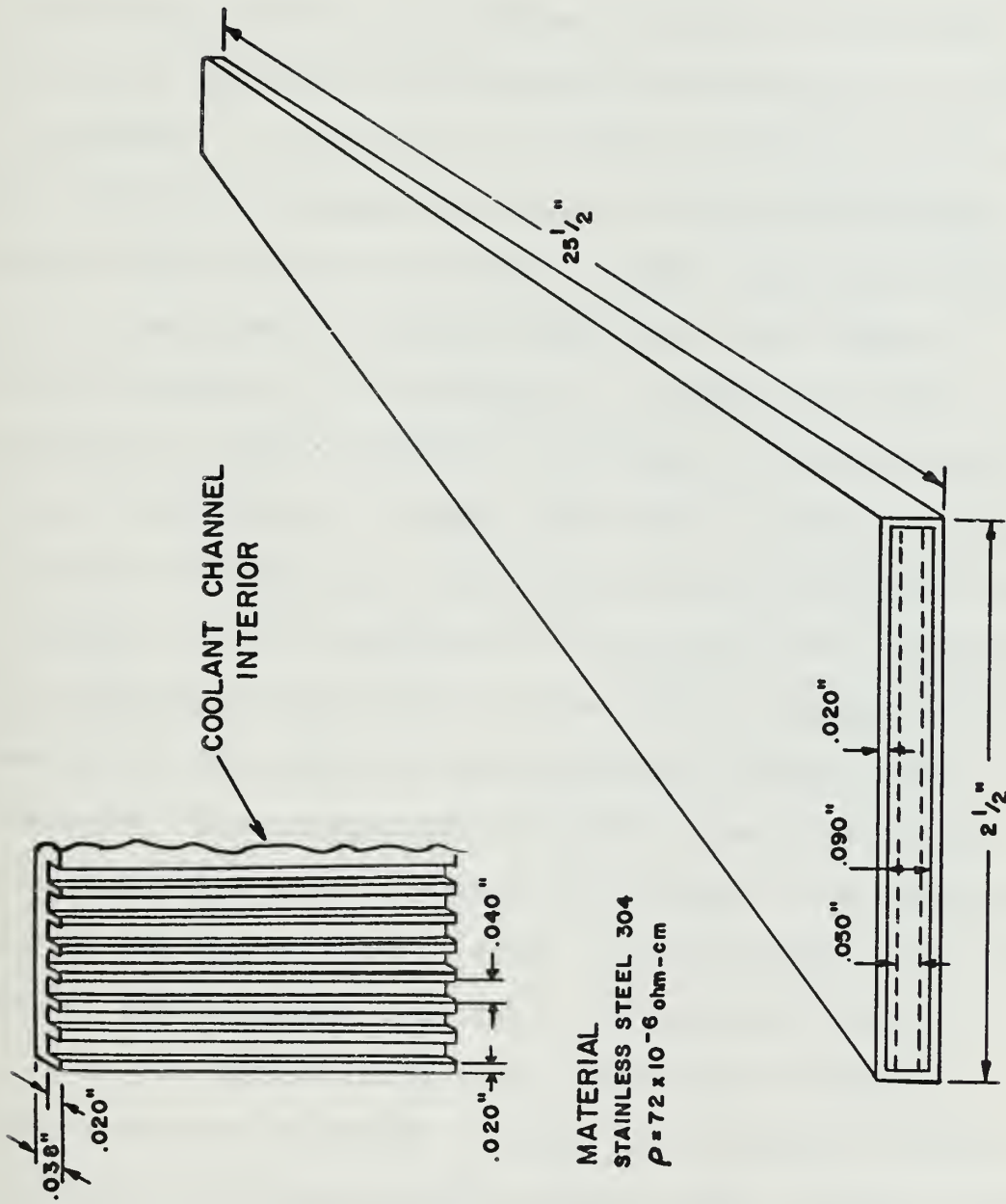


FIG. 5.4.2.1 FINNED CHANNEL



### 5.4.3 Description of Apparatus

#### 5.4.3.1 Hydraulic System

The experimental facility used was the low-pressure test loop located in the MIT heat transfer laboratory. The basic apparatus was designed and constructed in 1961. A schematic of the loop is presented in Figure 5.4.3.1.1. The pipes and fittings are made of brass and stainless steel for corrosion resistance. Rayon reinforced rubber hose is used where flexible connections are required. Distilled water is circulated by a bronze, two-stage, regenerative pump capable of providing a discharge pressure of 260 psig at 3.6 gpm. The pump is driven through a flexible coupling by a 3-hp Allis-Chalmers induction motor. A Fulflo filter is installed at the pump inlet. Pressure fluctuations at the outlet of the pump are damped out by means of a 2.5 gallon Greer accumulator charged with nitrogen. The accumulator contains a flexible bladder-type separator which prevents the nitrogen from being absorbed by the system water. After the accumulator, the flow splits into a bypass line and a test-section line.

In the test-section line, fluid flows through a Fischer-Porter flowrator followed by a preheater, thence through a Hoke metering valve and the test section, after which it merges with fluid from the bypass line. The flow then goes through the heat exchanger and returns to the pump. The preheater consists of four Chromalox heaters of



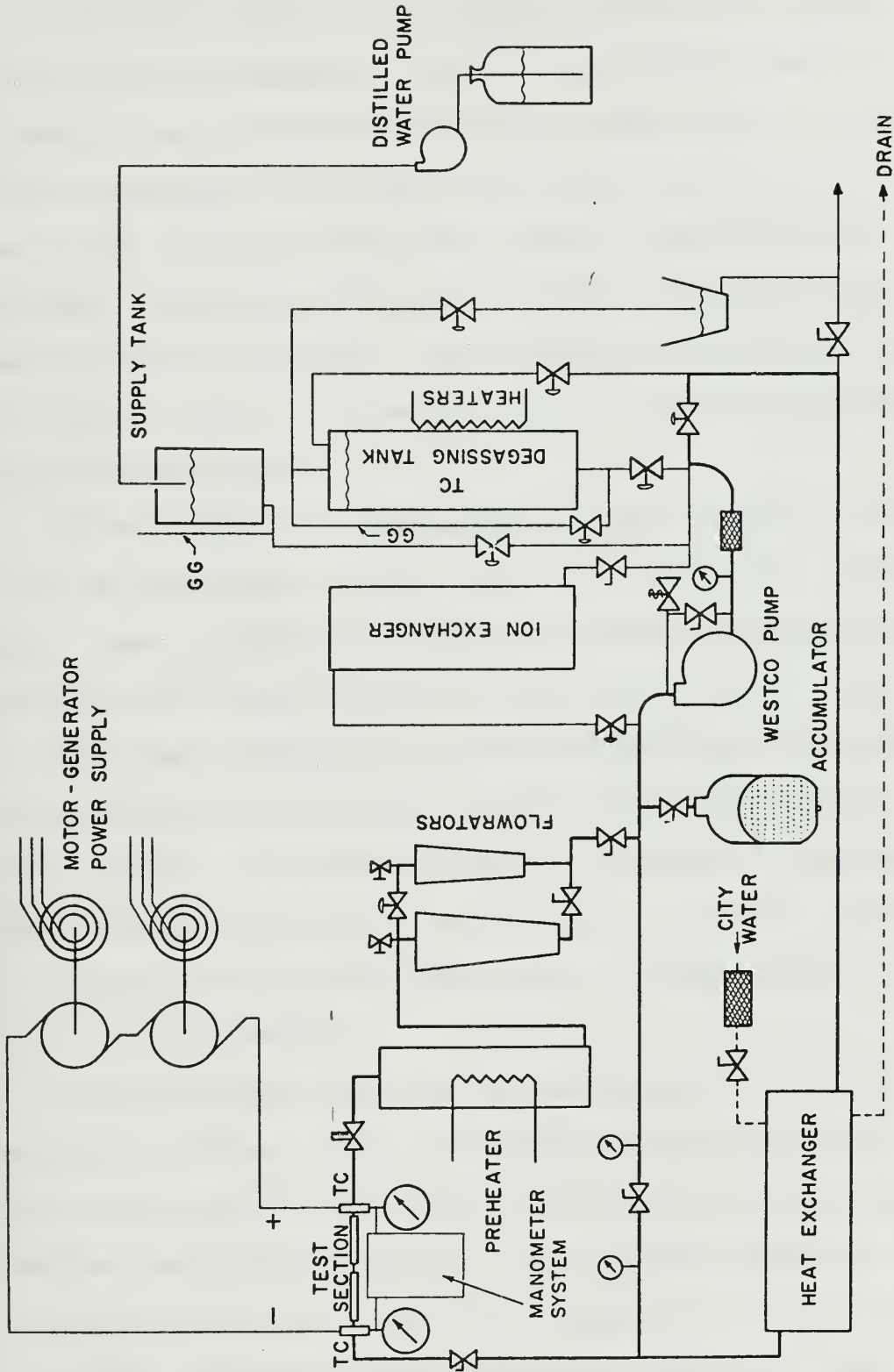


FIGURE 5.4.3.1.1.1  
SCHEMATIC LAYOUT OF EXPERIMENTAL FACILITY



approximately 6 Kw each. Three of the heaters are controlled simply with "on-off" switches while the fourth can provide a continuous range of 0 to 6 Kw by means of a bank of two variacs mounted on the test bench. Quick-action Jamesbury ball valves are installed before the inlet to the flowrator and after the exit from the test section. The ball valves permit quick isolation of the test section to minimize fluid loss when conducting burn-out tests. The exit valve can also be used to adjust the test section pressure.

Flow through the bypass line is controlled by a ball valve on each side of which there is a 300 psig pressure gage. Pump operating pressure, and hence the pressure upstream of the test section, is controlled by this valve.

The heat exchanger is a counterflow type with system water flowing in the inner tube and city water in the outer annulus. The heat exchanger is capable of maintaining a constant pump inlet temperature. A Fulflo filter is installed on the city water line to reduce scale formation in the exchanger.

The distilled water was de-ionized continuously by passing a portion of the flow through four mixed-bed resin demineralizer cartridges installed in a Barnstead-"Bantam" demineralixer unit. A 4.7 gallon degassing tank is provided with five electrical heaters (3-200 Vac and 2-110 Vac). The degassing tank also serves as a surge tank.





A 15-gallon stainless steel storage tank for filling the system is mounted directly above the degassing tank and can be filled with distilled water from standard 5-gallon bottles with a small Hypro pump.

#### 5.4.3.2 Power Supply

Test section electrical power is provided by two 36-KW dc generators connected in series. Each generator is rated at 12 volts and 3,000 amperes. The power control console permits coarse or fine control from 0 to 24 volts. A water-cooled shunt installed in parallel with the test section protects the generators against the shock of the sudden open circuit which would occur at burnout. Power is transmitted from the main bus to the test section by water-cooled power leads. In the present tests, the downstream or exit power lead was at ground potential. Rubber hose connected both inlet and exit chamber plenums to the main loop in order to electrically isolate the test section.

#### 5.4.3.3 Instrumentation

All temperatures were measured by copper-constantan thermocouples made from 30-gage Leeds and Northrup duplex wire. The test section inlet and outlet temperatures were measured by thermocouples directly in the fluid stream. The thermocouples were introduced into the piping



immediately before and after the test section through Conax fittings.

Coolant channel inlet and exit pressures were measured with Helicoid 8-1/2 inch gages with full scale readings of 200 psig and 100 psig, respectively. Both are specified to an accuracy of  $\pm 0.25\%$  of full scale. Pressure loss across the test section was also measured by a manometer located adjacent to the test stand.

A float tube calibrated for flows of 0 to 8 gallons per minute was installed in the basic Fischer-Porter flowmeter housing and provided measurement of the test section flow.

The voltage drop across the test section was read directly on a Digatec multiple range dc voltmeter with a specified accuracy of  $\pm 1/2$  percent. The current flow was determined by using a Wilson-Maeulen multi-volt meter (having 0-30 and 0-60 millivolt scales) to measure the voltage drop across a calibrated shunt (60.17 amp/mV) in series with the test section. Thermocouple voltages were read from a Honeywell-Brown continuous reading chart recorder.

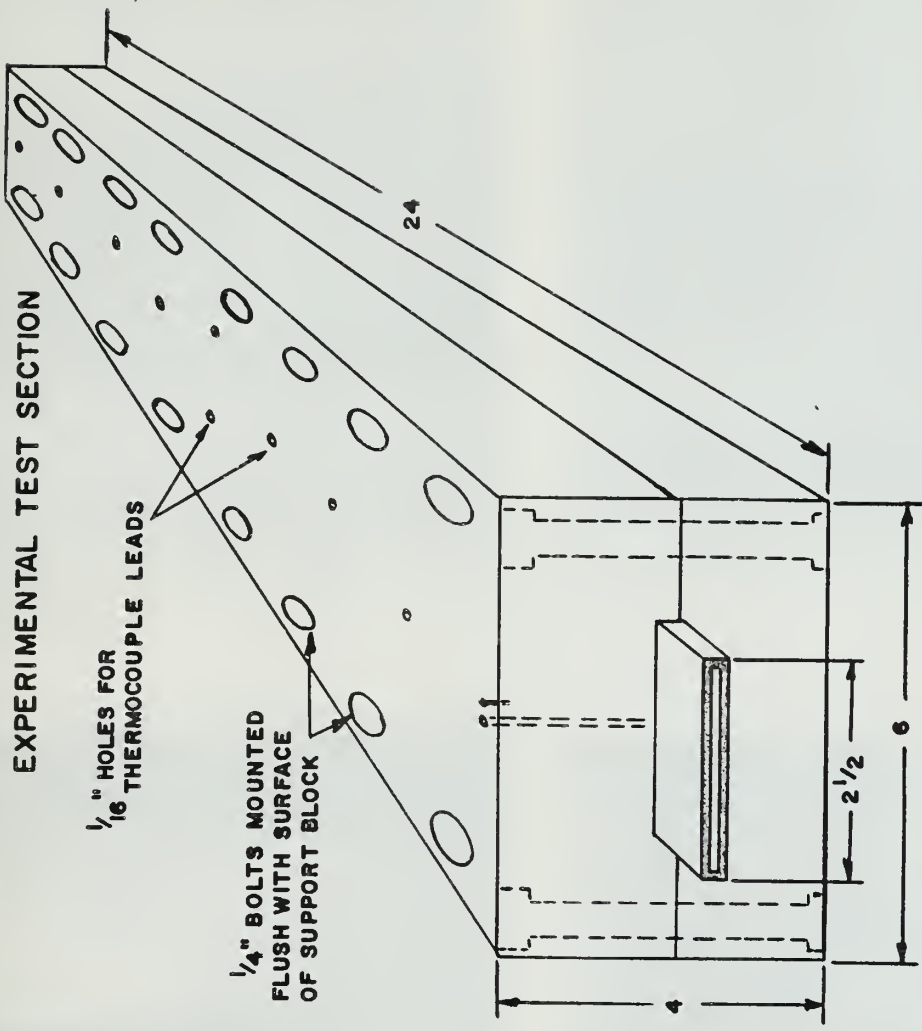
#### 5.4.3.4 Test Section

The test section consisted of a stainless steel coolant channel (described in Section 5.4.2) which protruded into two stainless steel end blocks. The end blocks



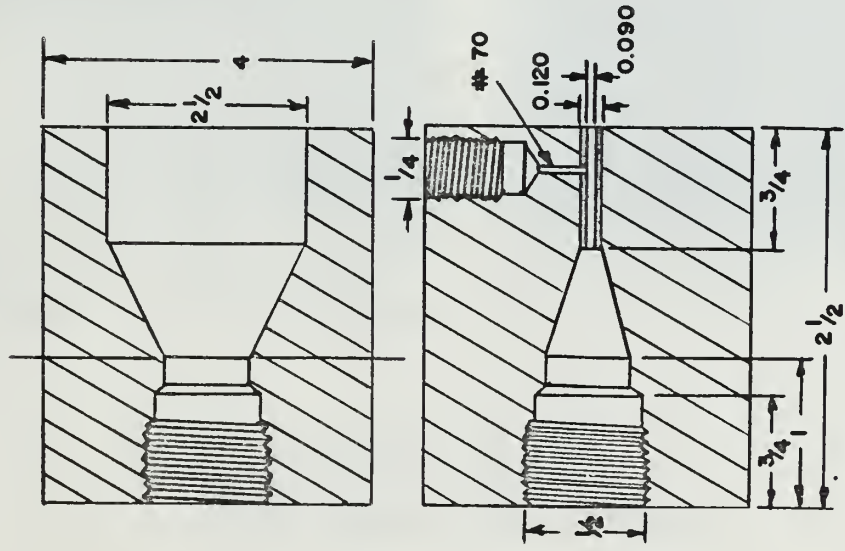
served, to act as an entrance plenum for the coolant water, to provide a point of attachment for the electrodes of the power supply, and to serve as a point of attachment for the pressure taps. Each end block was fabricated in three pieces; a base piece into which a 1/2 inch NPT was machined in order to provide a point of attachment for the coolant hose, and two entrance plenum sections which were machined so as to taper the water channel from a 1/2 inch diameter cylinder to a 0.130 inch by 2.5 inch rectangle. Figure 5.4.3.4.1 shows both a horizontal and a vertical cross section through an end block. Figures 5.4.3.4.2 and 5.4.3.4.3 show the test section in various stages of construction and assembly. The rectangular coolant channels protruded into a tight-fitting slot in the end blocks to a distance of 3/4 inch. Once inserted, the coolant channel and end blocks were bonded together with a stainless steel solder, and pressure taps were drilled into the coolant channel at the positions indicated in Figure 5.4.3.4.1. During the finned channel experimental runs, it was discovered that water was seeping around behind the coolant channel inside the end blocks. Consequently, the pressure taps, which protruded into the end blocks, were reading the pressures of the inlet and exit plenums rather than the pressures inside the inlet and exit of the coolant channel itself, as intended. In order to eliminate the inlet and exit





INSULATING / SUPPORT BLOCK MATERIAL : NEMA GRADE G-5 .

END BLOCKS



MATERIAL : STAINLESS STEEL

\* ALL DIMENSIONS ARE IN INCHES

FIG. 5.4.3.4.1 EXPERIMENTAL TEST SECTION









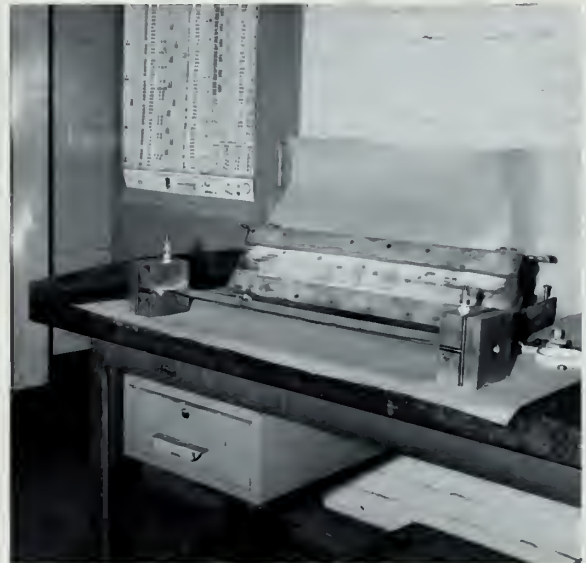
A. Three-piece end block before assembly. Coolant channel in foreground.



B. Channel end block showing coolant channel slot.



C. Finned coolant channel interior shown before bending and welding plate into rectangular channel.



D. Assembled coolant channel and end blocks.

FIGURE 5.4.3.4.2

EXPERIMENTAL TEST SECTION

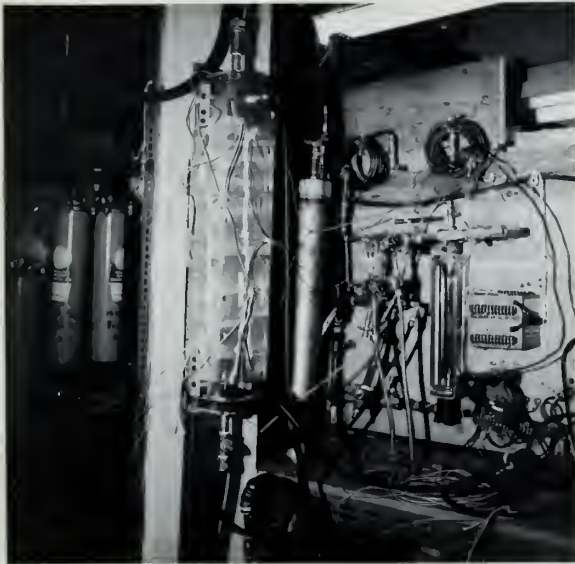




A. Coolant channel inserted into support block.



B. Test section assembled.



C. Test section in place in test facility.



D. Instrumentation stand.

FIGURE 5.4.3.4.3  
EXPERIMENTAL TEST SECTION



effects, and thus to measure only the pressure drop across the coolant channel, pressure sensing tubes were inserted through the endmost thermocouple holes in the front fiberglass block and through the coolant channel wall at those points. The existing pressure tap holes in the end blocks were plugged.

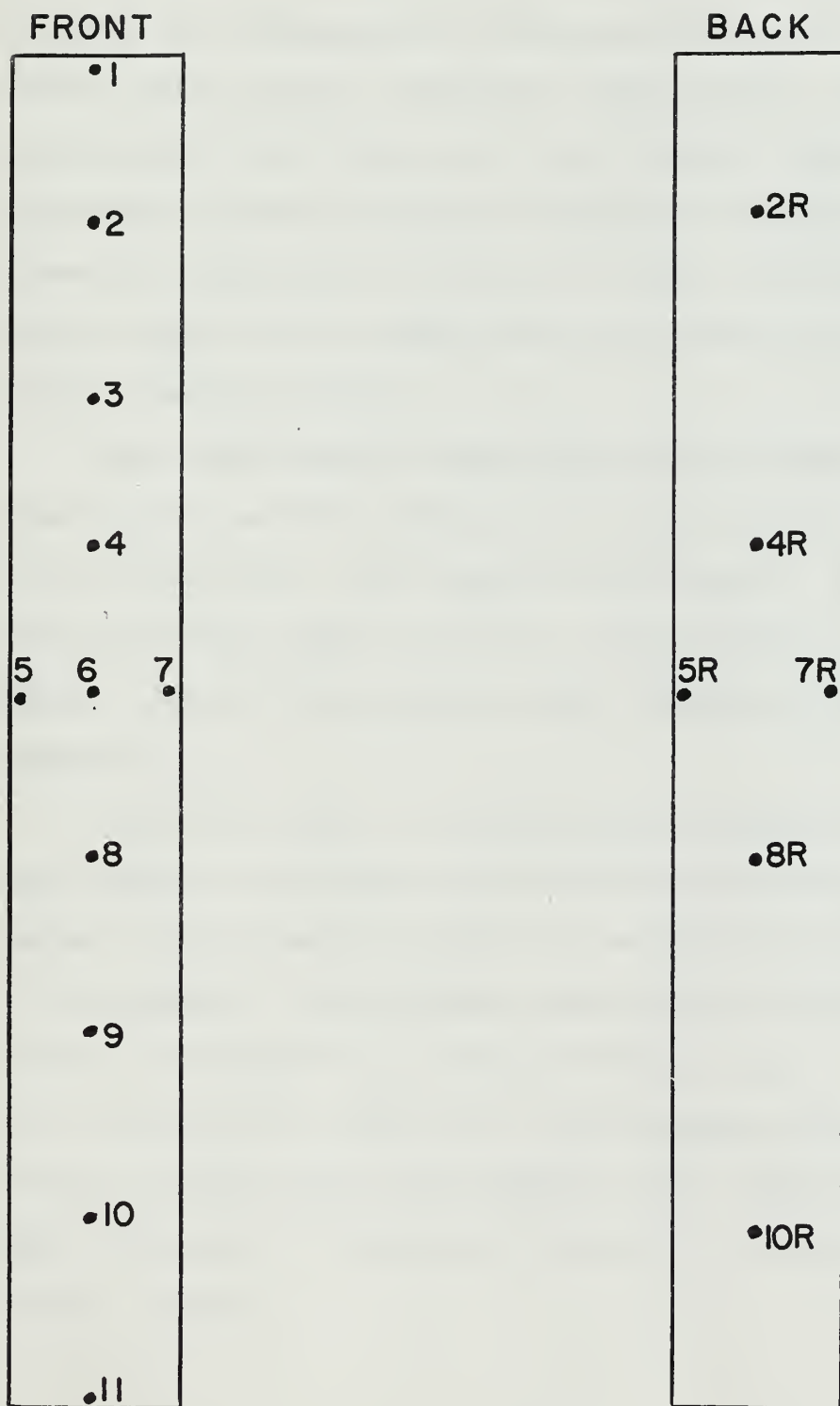
The coolant channel was physically supported by, and was electrically and thermally insulated by two 2" x 6" Nema grade G-5 fiberglass blocks. A rectangular channel 2 1/2" x 0.125" was milled into one of the fiberglass blocks in order to accept the coolant channel. The two fiberglass blocks were held together by 16 1/8" bolts spaced along either side of the coolant channel. Holes were drilled in the fiberglass blocks as shown in Figure 5.4.3.4.1 in order to provide access for the thermocouples to the coolant channel.

Teflon tape was used to electrically insulate the coolant channel from the thermocouples. A total of seventeen thermocouples were mounted on the coolant channel (see Figure 5.4.3.4.4 for arrangement). The thermocouples were pressed into place and held onto the coolant channel by the fiberglass support blocks. Four thermocouples were mounted near the surface of the fiberglass blocks in order to monitor the temperature gradient across these insulating/support blocks. In order to maintain a near zero temperature





THERMOCOUPLE ARRANGEMENT ON THE SURFACE OF THE COOLANT CHANNELS







gradient, three separate flexible tape heaters were wrapped around the fiberglass blocks. Heat output from these three heaters was adjusted using three variacs to maintain a nearly zero temperature difference between the outside channel wall and the fiberglass block surface, thus creating an adiabatic wall condition at the channel outer wall. The fiberglass blocks and heater strips were blanketed with fiberglass insulation in order to reduce the required heater output and to cause the strip heaters to give a more uniform heating effect.

Four steel support arms were bolted between the fiberglass blocks and the stainless steel end blocks in order to join the entire test section more firmly. By so doing, the probability that the solder joints between the coolant channel and end blocks would crack during handling was reduced.

The method used to change coolant channels in the test section was to heat the end blocks (not the coolant channel) sufficiently to melt the solder permitting removal of the channel. Once removed and allowed to cool, the end blocks were immersed in a crock of nitric acid. The nitric acid successfully removed all the remaining solder from the end blocks without any damage to the stainless steel, thus providing a clean smooth surface for installation of the new channel.



#### 5.4.4 Operating Procedure

With all system components installed and ready for operation, and with both the test section inlet and exit valves closed, the coolant pump was started and the bypass valve adjusted to provide 20 psig backpressure to the test section. Next the test section exit valve followed by the test section inlet valves were opened and adjusted to provide the desired flow through the test section. All high point bleeder valves were opened and trapped gasses allowed to escape. At this point, the guard heaters were turned on and adjusted to provide a insulating block surface temperature equivalent to the expected coolant channel wall temperature. The bus bar cooling water was turned on as well as the city water to the heat exchanger. The final stage in the startup process was accomplished by synchronizing and starting the generators. After allowing the generators to warm up, they were brought up to power and allowed to stabilize. The flow of city water to the heat exchanger was adjusted until a constant inlet coolant water temperature to the test section was obtained. With all conditions stable, data was taken. This data included coolant channel inlet and exit pressure, voltage drop across and amperage flowing through the test section, and all thermocouple readings.



#### 5.4.4 Operating Procedure

With all system components installed and ready for operation, and with both the test section inlet and exit valves closed, the coolant pump was started and the bypass valve adjusted to provide 20 psig backpressure to the test section. Next the test section exit valve followed by the test section inlet valves were opened and adjusted to provide the desired flow through the test section. All high point bleeder valves were opened and trapped gasses allowed to escape. At this point, the guard heaters were turned on and adjusted to provide a insulating block surface temperature equivalent to the expected coolant channel wall temperature. The bus bar cooling water was turned on as well as the city water to the heat exchanger. The final stage in the startup process was accomplished by synchronizing and starting the generators. After allowing the generators to warm up, they were brought up to power and allowed to stabilize. The flow of city water to the heat exchanger was adjusted until a constant inlet coolant water temperature to the test section was obtained. With all conditions stable, data was taken. This data included coolant channel inlet and exit pressure, voltage drop across and amperage flowing through the test section, and all thermocouple readings.



#### 5.4.5 Assumptions for Data Analysis

In analyzing coolant channel heat transfer data, the Colburn correlation  $Nu_f = 0.023 Re_f^{0.8} Pr_f^{0.3}$  was used as the basis for comparison. From the basic equation for heat conduction  $Q = hA(T_w - T_b)$ ,  $Q$ ,  $T_w$ , and  $T_b$  are experimentally measured, and  $A$  is the constructed internal surface area of the coolant channel. The heat transfer coefficient can thereby be calculated directly. For purposes of comparing smooth channel experimental data with the Colburn correlation, equivalent diameter was calculated using the relation,  $D_e = \frac{4A}{P}$ .

In order to compare heat transfer from a smooth channel with that from a finned channel, it is necessary to establish certain constants for comparison. For the purposes of reactor design, it is both desirable and reasonable that both the center-to-center spacing of the fuel meat in the core, and the mass flow rate through an individual coolant channel remain constant. Consequently, in comparing the smooth channel with the finned channel, it was assumed that the two channels had both the same equivalent diameter and the same cross sectional area for coolant flow. Thus, for a given mass flow rate Reynolds number (smooth) equals Reynolds number (finned). As a result, a relative comparison of heat transfer ability was obtained.

The only temperature correction incorporated into the experimental data analysis was the correction for temperature







drop across the coolant channel wall. Coolant channel outside wall temperature is measured whereas inner wall temperature is desired. The correction was made using the relation,

$$T_{wi} = T_{wo} - \frac{Qt}{2KA},$$

where  $Q/A$  = heat flux

$K$  = thermal conductivity of the channel wall, and

$t$  = channel wall thickness.

Although to a first approximation the heat flux along the coolant channel was uniform, a small correction was required to the heat flux as a function of position along the coolant channel due to the temperature dependence of resistivity. Since resistivity increases with increasing temperature according to the relation  $\rho = \rho_0(1 + \alpha T)$ , more heat would be generated near the exit of the electrically heated coolant channel than near the entrance. The temperature coefficient of resistivity for a piece of the stainless steel used in the fabrication of the coolant channels was measured over a range of temperature between that of liquid nitrogen and 100°F water and found to be 0.002/°F. Wall temperature rise between channel inlet and exit was typically on the order of 50°F. Therefore, the actual input heat flux to the channel varied typically from -5% at the entrance to +5% at the exit from the channel average. Since for a given



measured temperature drop between the channel wall and bulk fluid heat transfer coefficient is directly proportional to input heat flux, a corresponding correction was made to the experimentally measured heat transfer coefficients.

#### 5.4.6 Experimental Results

Smooth channel data is presented in Figure 5.4.6.1 and is shown to be about 12% above the Colburn correlation. Such increased heat transfer was expected because the smooth channel tested was not perfectly smooth. When the thermocouples were pressed onto the channel outside wall small indentations were formed which protruded through the wall and into the coolant flow path. These thermocouple "nipples" acted as roughness elements in promoting heat transfer. The smooth channel data taken is best fit by the correlation  $Nu_f = 0.027 Re_f^{0.8} Pr_f^{0.3}$ . (It should be noted that a leak developed at the entrance solder joint between the test section end block and coolant channel. It is felt that this leak did not affect experimental results, however.)

Finned channel data is presented in Figures 5.4.6.2, 5.4.6.3, 5.4.6.4 and 5.4.6.5. The upper curve of Figure 5.4.6.2 was drawn through points representing the average value of calculations from 10 centerline thermocouple readings for each experimental run. The curve is fit by



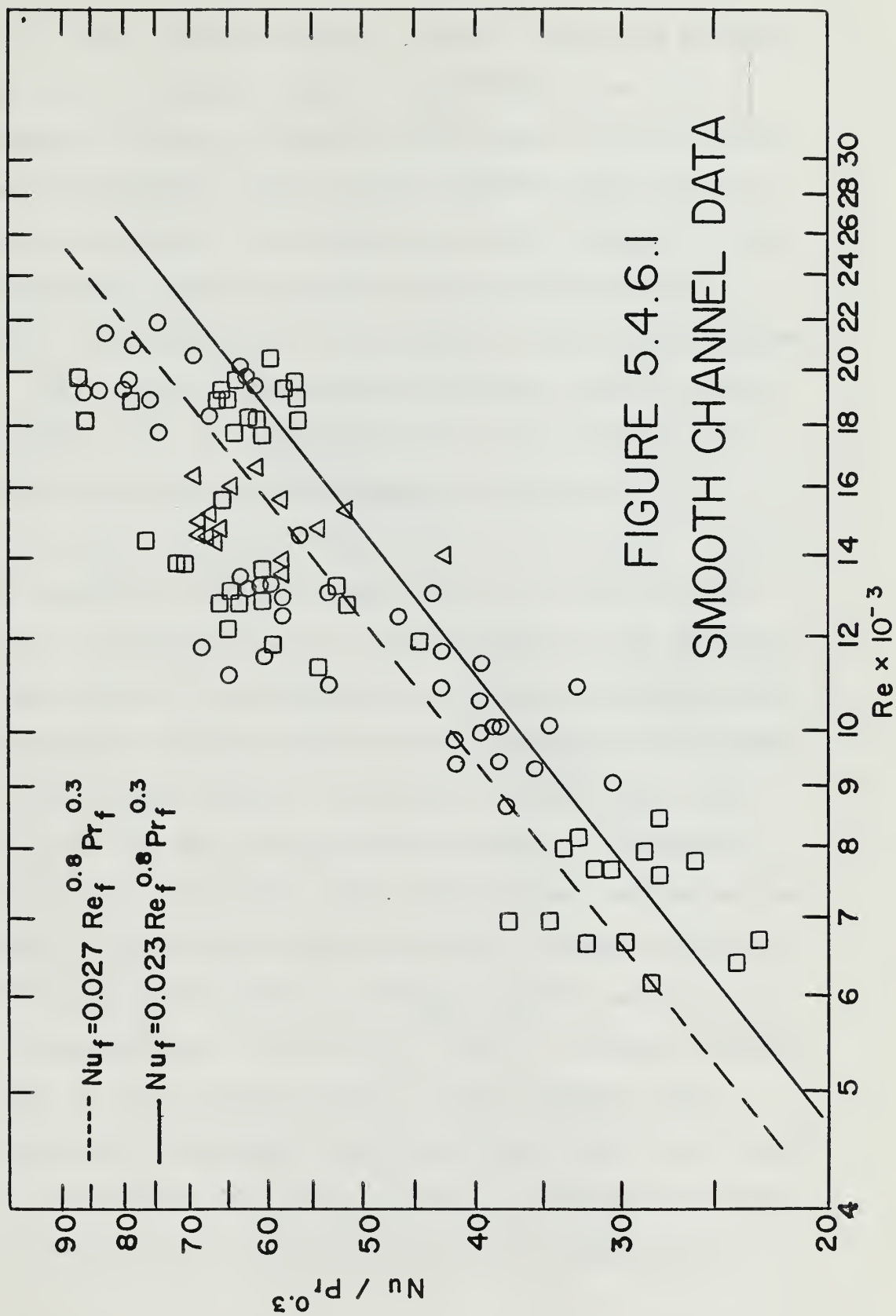


FIGURE 5.4.6.1  
SMOOTH CHANNEL DATA



the relation  $Nu_f = 0.052 Re_f^{0.8} Pr_f^{0.3}$ . The points along the lower curve of Figure 5.4.6.2 represent average values for each smooth channel experimental run. In calculating the heat transfer coefficients for the finned channel experimental runs, it was observed that the heat transfer coefficient was highest near the entrance of the coolant channel and decreased toward the exit of the channel. This effect did not show up in the smooth channel runs. Heat transfer coefficient averaged over the seven experimental runs is shown plotted versus thermocouple position along the coolant channel in Figure 5.4.6.3. Since one would normally expect the heat transfer coefficient to increase slightly toward the exit of the coolant channel, the validity of the finned channel heat transfer data was subject to investigation. It was suspected that some asymmetry existed either in the thermocouple readings or in the channel itself. In order to investigate this possibility the test section was inverted. Everything remained as it was except, now, upside-down, and an entire new set of experimental runs was made. Average values of  $Nu/Pr^{0.3}$  are shown plotted in Figure 5.4.6.4 and are fit by the relation  $Nu_f = 0.050 Re_f^{0.8} Pr_f^{0.3}$ , almost exactly the same as the relation which fit the original data. Heat transfer coefficient versus position along the coolant channel is plotted in Figure 5.4.6.5. Although the slope of this curve is not as great as that of Figure 5.4.6.3,





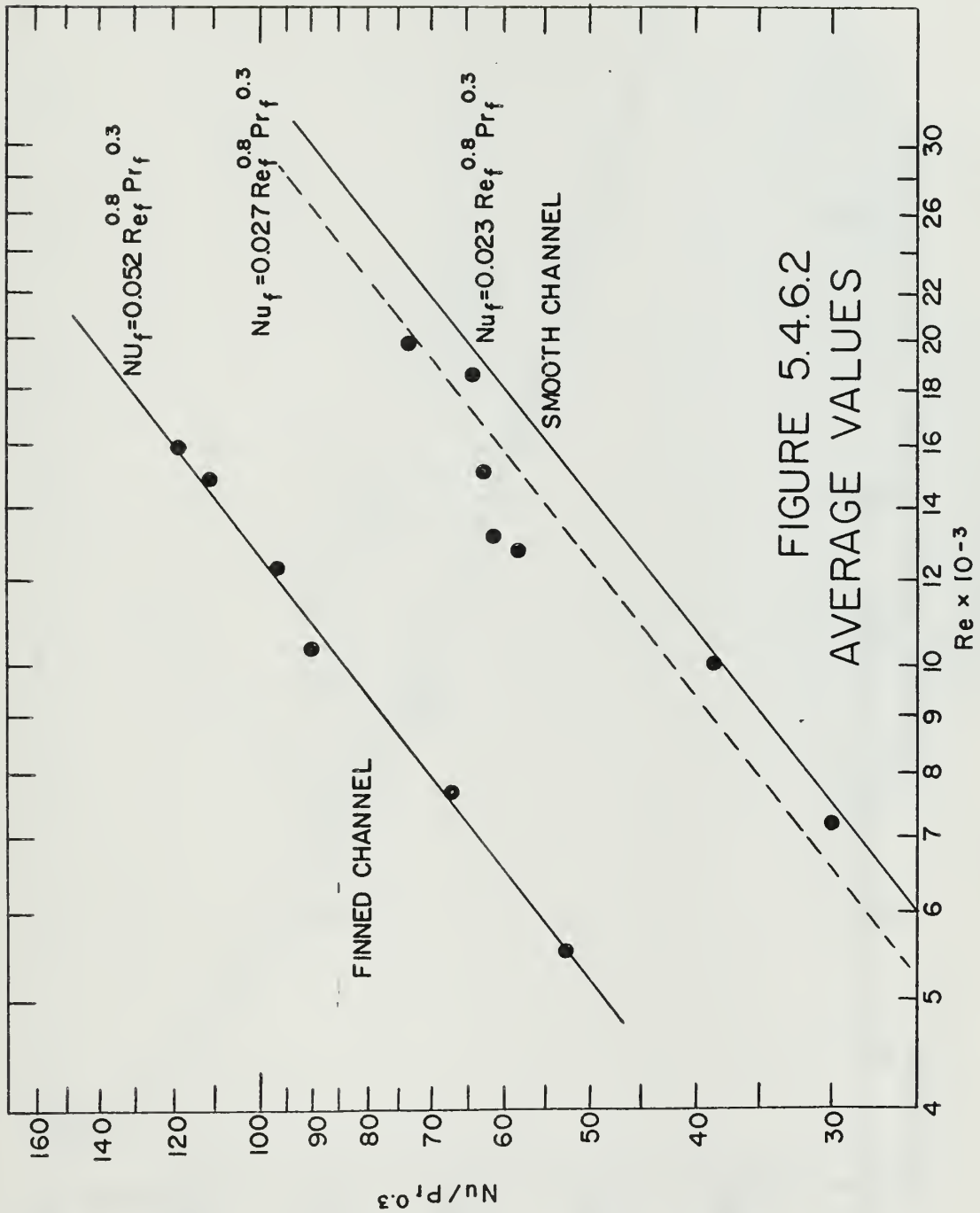


FIGURE 5.4.6.2  
AVERAGE VALUES



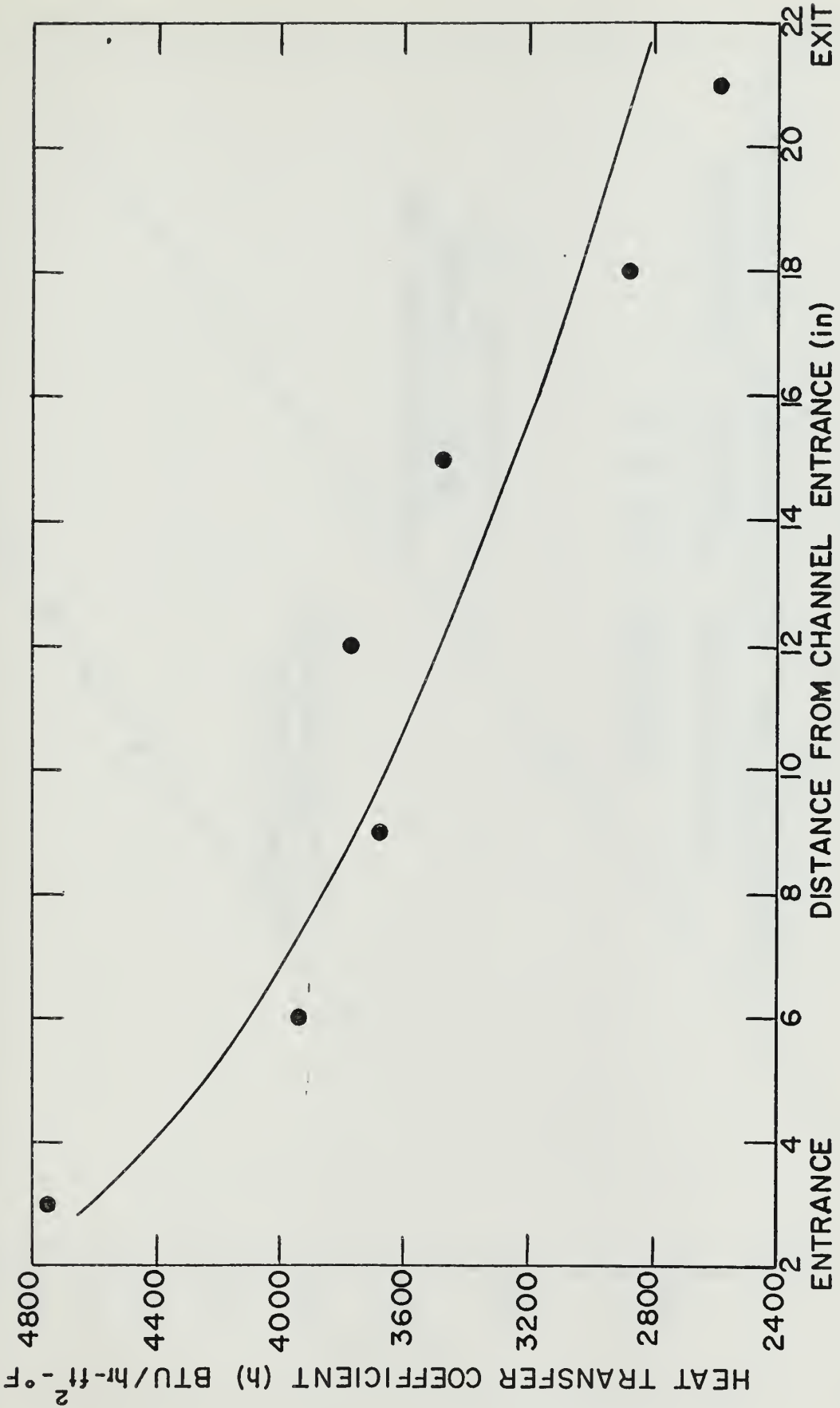


FIGURE 5.4.6.3  
HEAT TRANSFER COEFFICIENT vs. POSITION IN THE  
COOLANT CHANNEL



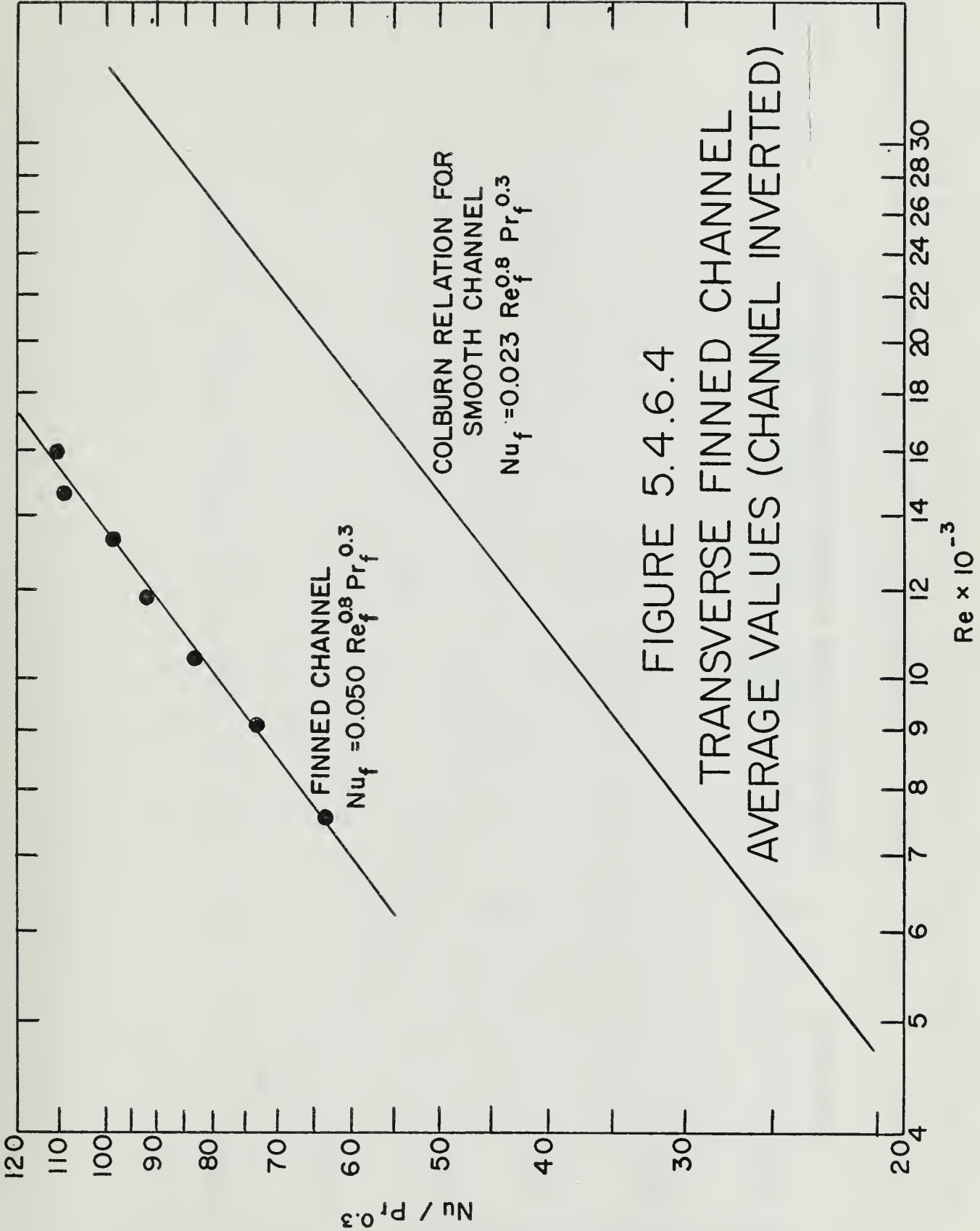


FIGURE 5.4.6.4  
TRANSVERSE FINNED CHANNEL  
AVERAGE VALUES (CHANNEL INVERTED)

FINNED CHANNEL  
 $Nu_f = 0.050 Re_f^{0.8} Pr_f^{0.3}$

COLBURN RELATION FOR  
SMOOTH CHANNEL  
 $Nu_f = 0.023 Re_f^{0.8} Pr_f^{0.3}$



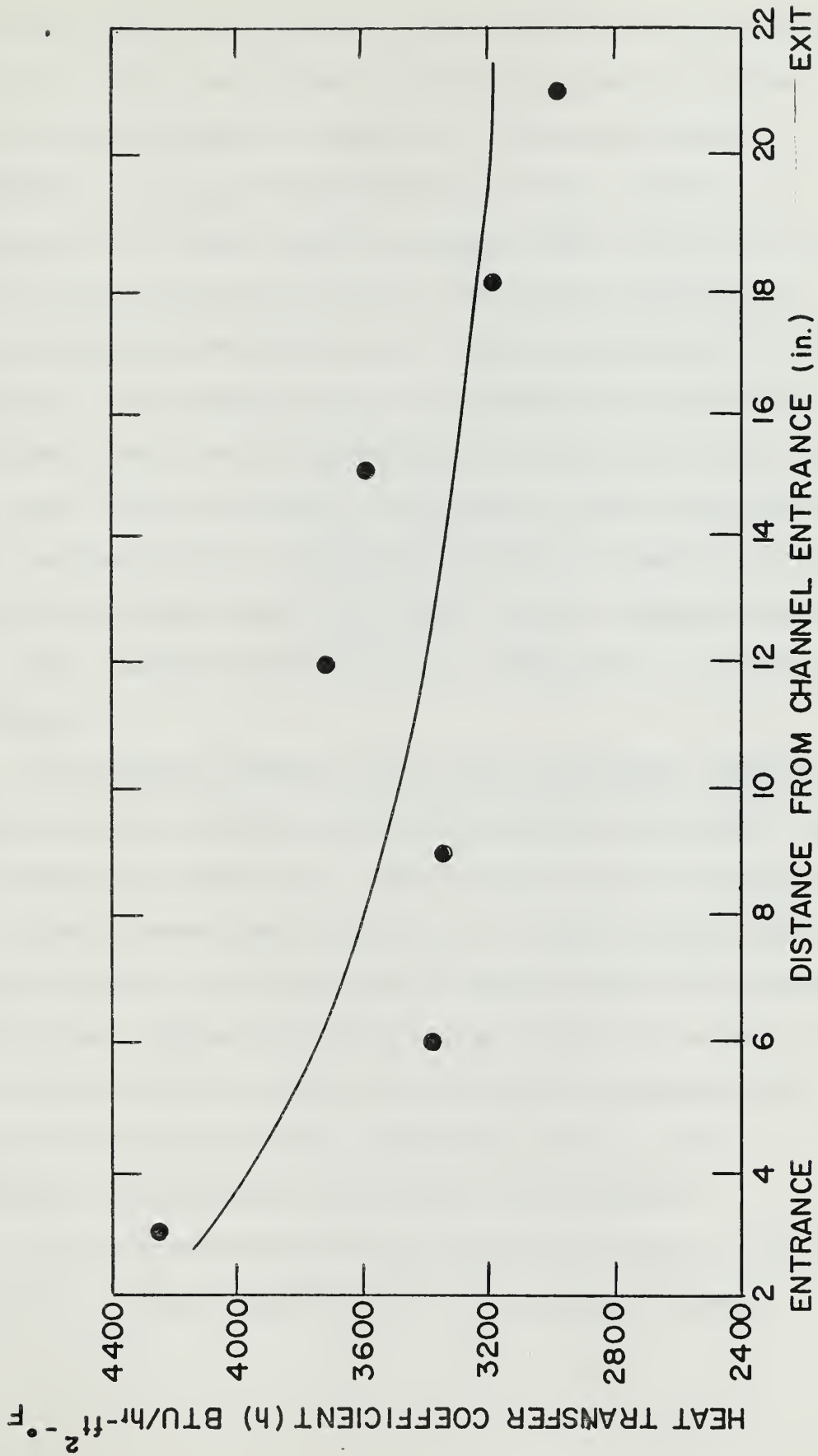


FIGURE 54.6.5 HEAT TRANSFER COEFFICIENT vs. POSITION IN THE COOLANT CHANNEL (CHANNEL INVERTED)





the same trend of decreasing heat transfer coefficient with distance along the coolant channel is present, and the shape of the curves is identical. At present there appears to be no good explanation for this effect. However, it is felt that the average value curves of Figures 5.4.6.2 and 5.4.6.4 can be used with confidence in heat transfer calculations for the proposed High Flux MIT Reactor. The average values are conservative when one considers that due to control rod insertion into the reactor core, only the lower 12-16 inches of the fuel plates will be generating a significant amount of power, and it is in this region near the coolant channel entrance that the heat transfer coefficient was measured to be above average.

In computing average values for the finned channel data, only the readings from thermocouples along the channel centerline were used. Heat transfer near the edge of the finned channel was observed to be much greater (by about a factor of 2) than heat transfer along the channel centerline. The most probable reason for this effect is that there existed a small gap between the channel side walls and the ends of the transverse fins in which secondary (additional) turbulence was generated.

It is recommended that the modified Colburn correlation,  $Nu_f = 0.023 Re_f^{0.8} Pr_f^{0.3}$ , be used for smooth



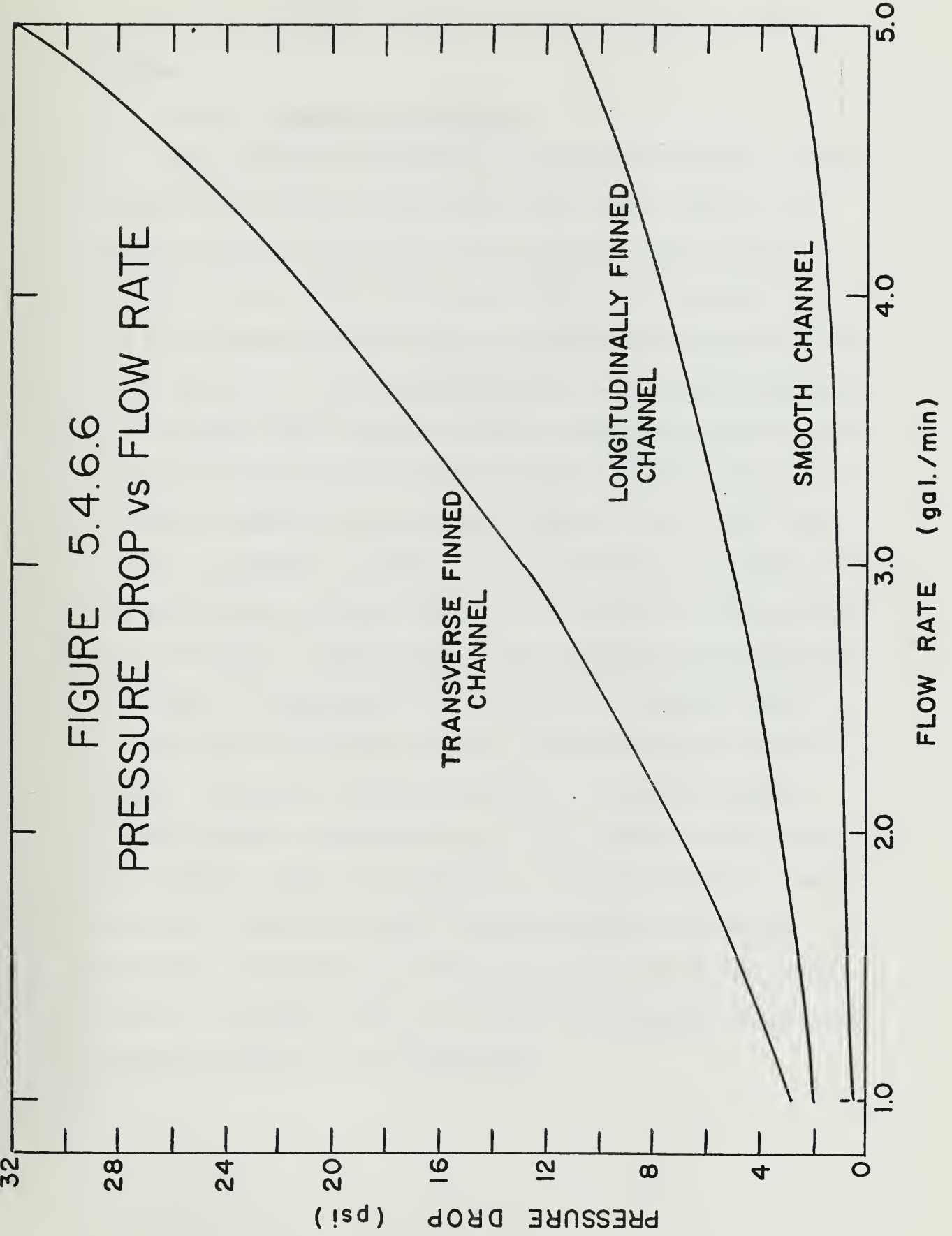
channel calculations and that the correlation  $Nu_f = 0.050 Re_f^{0.8} Pr_f^{0.3}$  be used for calculations for finned channels similar to that of this experiment. Heat transfer from the finned channel is thus a factor of 2.2 greater than heat transfer from a smooth channel. The heat transfer surface area of the finned channel was a factor of 1.67 greater than that of the smooth channel. Since fin efficiency in this case was nearly 100%, the factor of 2.2 increase in heat transfer can be taken as the product of a factor of 1.67 increase in heat transfer area multiplied by a factor of 1.3 due to increased turbulence caused by the fins. To be more precise, the product "hA" was increased by a factor of 2.2, while "h" alone was increased by a factor of 1.3.

Pressure drop data for both the smooth and finned channels is presented in Figure 5.4.6.6. The smooth channel pressure drop was much larger than that normally associated with a smooth channel, but, like smooth channel heat transfer, this can be attributed to channel roughness caused by thermocouple indentations. Channel entrance and exit pressure losses are included in the plotted value of smooth channel pressure drop.

Finned channel pressure drop was very large, with  $\Delta P$  varying roughly proportional to  $V^{1.6}$ . This large pressure loss is a limiting factor on the coolant mass flow rate



FIGURE 5.4.6.6  
PRESSURE DROP vs FLOW RATE





which can be pumped through the core using the existing pumps.

#### 5.4.7 Analysis of Results

D<sub>2</sub>O pressure measurements around the primary coolant loop of the existing MITR show that there exists a 23 psig pressure drop between the primary heat exchanger exits and the core inlet piping (36). The pressure loss in the piping between these two points should be no more than 1-2 psi. The 23 psig pressure drop can be explained by the fact that between the heat exchanger exits and the core inlet are valves which are kept partly closed in order to regulate the primary coolant flow. Were these valves completely opened, it is reasonable to assume that an additional pressure head on the order of 21 psig would be available. Consequently, core pressure drop could be increased by approximately 21 psig while maintaining a flow rate of 2000 gpm with the existing primary coolant pumps. However, a pressure drop of 21 psig through a finned channel corresponds to a flow rate of only 4 gallons per minute. Were 10.95 gpm to be pumped through a smooth channel, equivalent heat transfer would be realized. Implicit in the above information is the fact that there exists a certain cutoff core size, assuming no additional pumping power is to be installed.





Smooth coolant channels will give better heat in cores of smaller size, whereas it is advantageous to use the finned coolant channels in cores of larger size. Table 5.4.7.1 below gives a brief analysis of two coolant channel sizes of possible interest.

Table 5.4.7.1

	2.5"x0.090" channel	2.1"x0.090" channel
Max. finned channel flow rate*	4 gpm	3.36 gpm
Equivalent smooth channel flow rate	10.95 gpm	9.20 gpm
Break even point	183 channels, or 11-17 channel elements	218 channels, or 15-15 channel elements
Actual heat transfer Increase $\frac{hA(\text{finned})}{hA(\text{smooth})}$	1.2 for a 12 element core	1.84 for a 26 element core

\*Core  $\Delta P_{\max} = 21$  psi

Thus, for purposes of the MITR redesign, the benefit to be derived from fuel plate finning varies with the size of the core under consideration.

One core configuration considered for the phase II High Flux MITR contains 26 fuel elements, with each element containing 15-2.1" x 0.090" coolant channels. Comparing smooth channels to finned channels for this core configuration shows that the pressure drop limited finned channel



will provide a factor of 1.84 better heat transfer than a smooth channel. However, since the heat transfer area of the finned channel is a factor of 1.67 greater than the smooth channel, the heat transfer coefficient is in fact increased by only a factor of 1.1. More important, though, is the fact that the factor increase of 1.84 is greater than the factor of 1.8 required for the light water core. While the optimum plate roughness condition for heat transfer augmentation has not yet been achieved, it has been demonstrated that the currently installed process system is capable of removing the heat from the hottest fuel element of the proposed High Flux MITR core.

For a flow of 2000 gpm through a 26 element core, 5.15 gpm would flow through each coolant channel. From Figure 5.4.6.6 this flow rate would cause a pressure drop across the core on the order of 33 psi, or 12 psi above the existing system capability. However, if one were to either install new main coolant pumps or install booster pumps downstream of the heat exchangers capable of providing an additional 12 psi of pressure head, the finned channel pressure drop limitation could be eliminated, thus allowing one to fully realize the 2.2 factor increase in heat transfer for a finned channel over a corresponding smooth channel. In addition, if new coolant pumps were to be purchased, pumps of not only higher head capacity but



also greater flow rate capacity could be installed, thus adding even a little more to the degree of heat transfer augmentation possible.

#### 5.4.8 Further Investigations

At the suggestion and with the assistance of this author, the heat transfer and pressure drop characteristics of a longitudinally finned coolant channel have been investigated by Mr. Donald Uhl. A longitudinally finned (fins running parallel to the coolant flow path) fuel plate enjoys three advantages over a transverse finned (fins perpendicular to the coolant flow path) fuel plate such as investigated in the previous sections: (1) the longitudinal fins provide little additional turbulence and thereby create less pressure drop across the core, (2) fabrication of the fins is less time consuming because fewer milling cuts are required, and (3) fuel plate buckling cannot completely block a coolant channel because flow can always occur in the grooves between fins.

It was originally intended that the coolant channel plate be milled so as to produce fins 20 mils wide, 20 mils in height, and spaced 20 mils apart, thus increasing surface area over that for a smooth plate by a factor of 2. However, due to difficulties experienced in milling the fins into the stainless steel plate (difficulties which should not be encountered when milling fins into



the actual aluminum fuel plates), the spacing between fins was increased from 20 mils to 40 mils, thus providing an area increase of 1.67.

Pressure drop data versus flow rate for the longitudinally finned coolant channel is shown on Figure 5.4.6.6. Although larger than that for a smooth channel, pressure drop is shown to be considerably less than that for a transverse finned channel and will not impose a limiting condition on primary coolant flow rate.

Experimental heat transfer data is presented in Figure 5.4.8.1. Each point shown is an average of the data from each of the 10 thermocouple readings recorded for each run. The experimental data is fit by the relation  $Nu_f = 0.037 Re_f^{0.8} Pr_f^{0.3}$ . Thus the longitudinally finned channel augments heat transfer by a factor of 1.6 over that from a smooth plate. Since the area ratio, finned to smooth, was 1.67, it is seen that the increase in heat transfer was 0.958 times the increase in surface area. Thus, it is reasonable to expect that if the longitudinal fins were to be spaced 20 mils apart, thereby doubling the heat transfer area, one could expect heat transfer to be increased by a factor of 1.92.





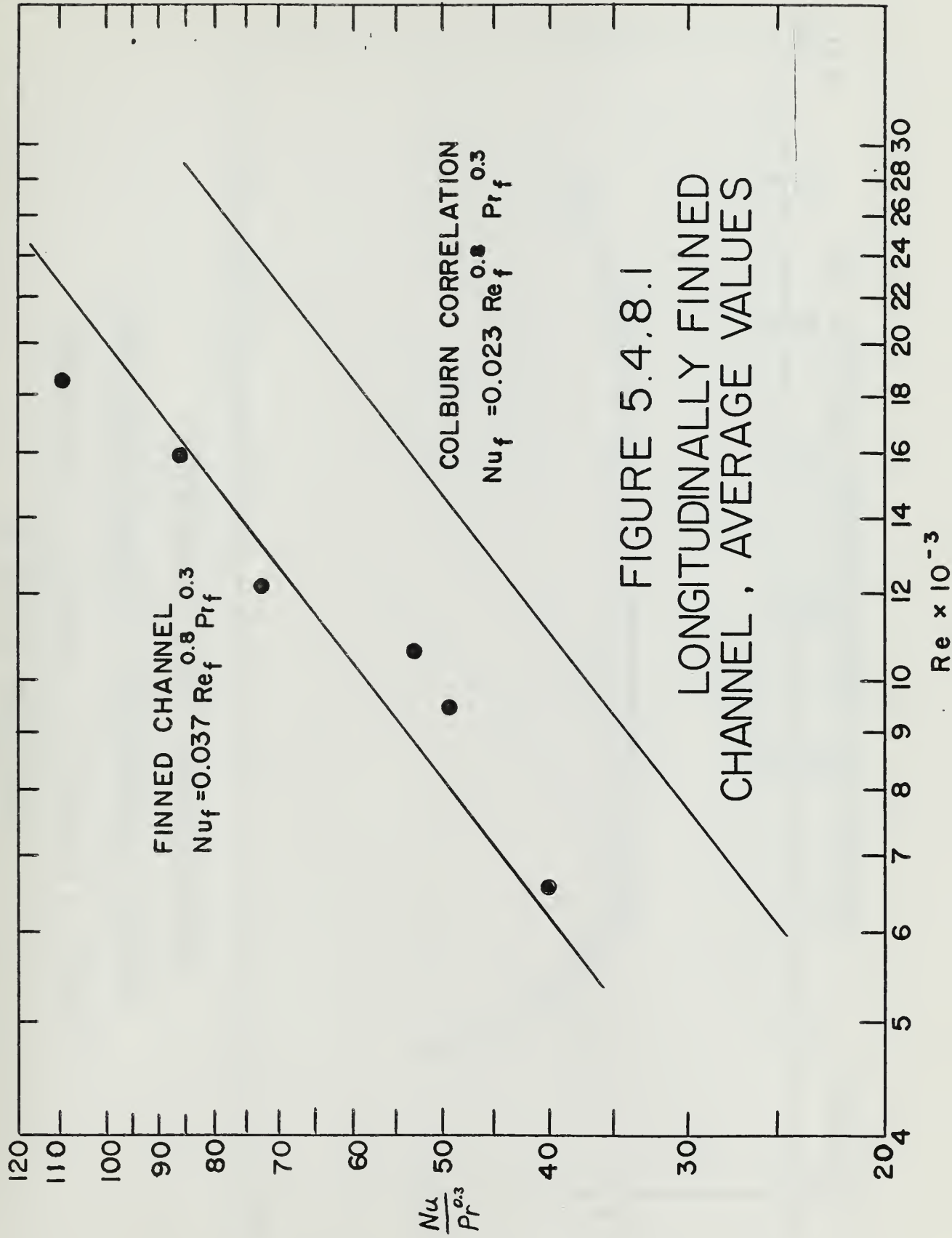


FIGURE 5.4.8.1  
LONGITUDINALLY FINNED  
CHANNEL, AVERAGE VALUES



FIGURE 5.4.8.2  
LONGITUDINALLY FINNED CHANNEL  
HEAT TRANSFER COEFFICIENT VS.  
POSITION IN THE CHANNEL

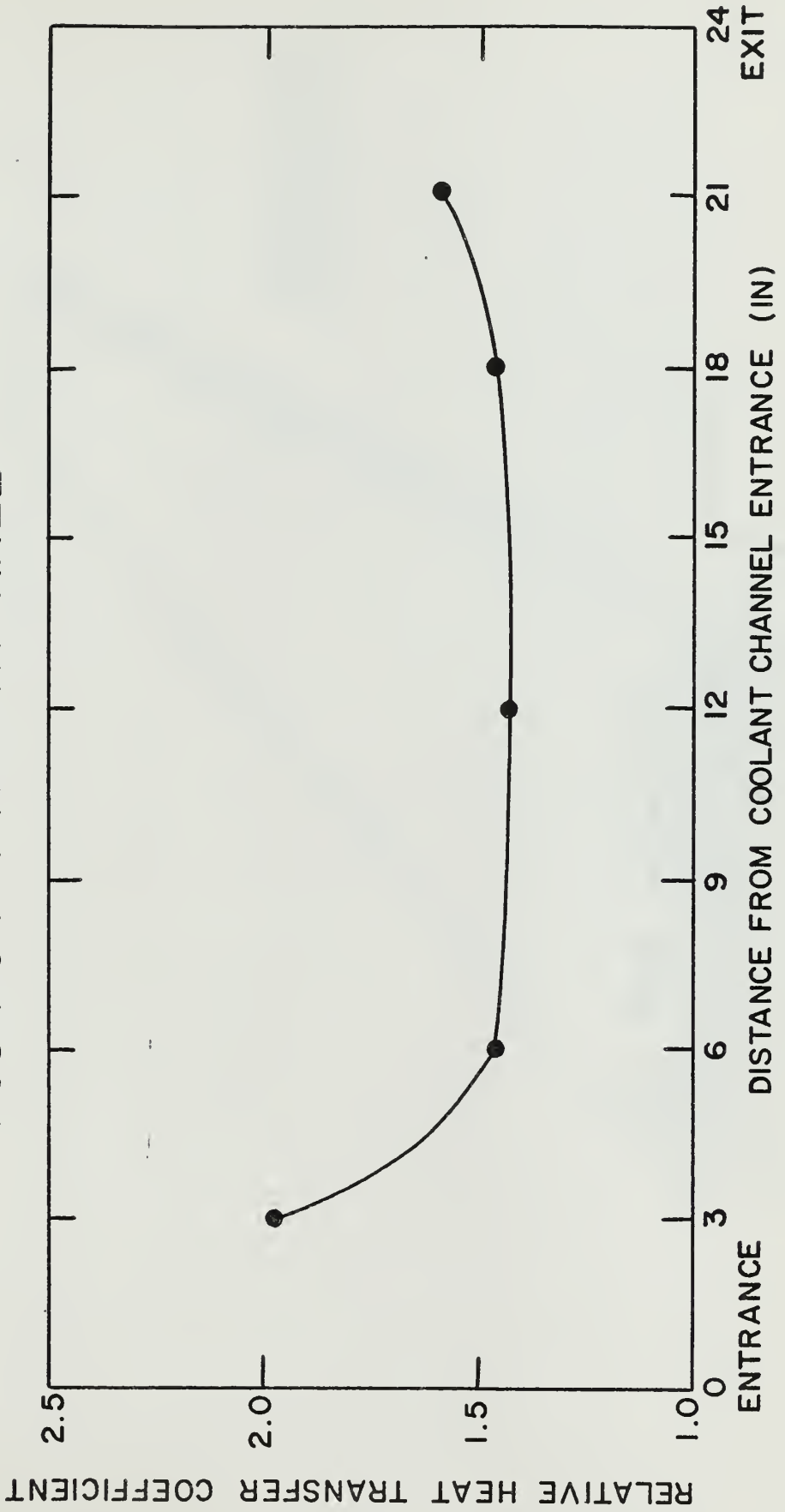
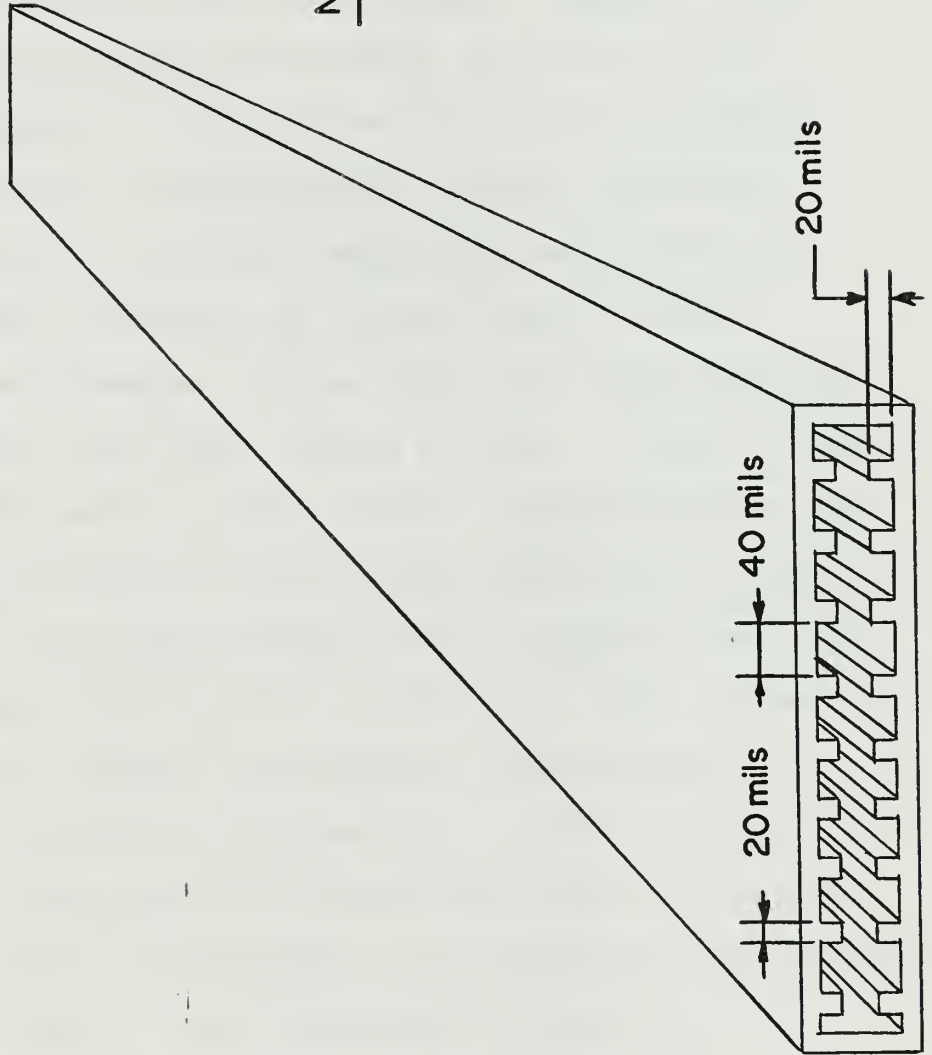




FIGURE 5.4.8.3

LONGITUDINALLY FINNED CHANNEL



NOT TO SCALE



## Chapter 6

## CONCLUSIONS

It is not intended that the work which has been presented represent a final design or a final design analysis, but rather that the preceeding work make some contribution toward that final design. Chapter 2 has shown that while much work remains to be done in the area of mechanical design, there seem to be no prohibitively difficult or unsurmountable design problems. While the shield design and supporting calculations of Chapter 3 must certainly be refined based on final shielding requirements, it has been shown that shielding will not pose a difficult design problem. Chapter 4 has indicated the need to find a means of augmenting the convective heat transfer from the High Flux MITR fuel plates. In response, the experimental work of Chapter 5 has demonstrated that by modification of the fuel plate surface the required heat transfer augmentation can be achieved.

In surveying the work pertinent to the contents of this thesis which must be accomplished prior to setting a final High Flux MITR design, it is apparent that mechanical design work is being thoroughly covered by Mr. E. Barnett. Final shield design can be obtained by simple extrapolation of the work of Chapter 3. It is in the area of core heat removal that the most intriguing area





for future work lies, that of optimizing the means by which fuel plate heat transfer is to be augmented. In order to make a tentative decision based on information available at this time, the following summary analysis based on heat transfer coefficient,  $h$ , is presented for the phase II core design.

For a maximum homogeneous power density of  $1.3 \times 10^{13}$  fissions/cm<sup>3</sup>-sec along the base of the core (equivalent to that assumed in previous analyses), the maximum heat flux through fuel plates spaced 0.090" apart will be  $2.12 \times 10^5$  BTU/hr-ft<sup>2</sup>. At the coolant entrance, the saturation temperature of H<sub>2</sub>O is 228.5°F. Assuming the reactor were just about to scram due to high coolant outlet temperature, bulk inlet coolant temperature would be 114.5°F. Thus, since fuel plate wall temperature is the sum of bulk coolant temperature plus the film temperature rise from the bulk fluid to the fuel plate wall ( $T_w = T_b + Q/hA$ ), in order to prevent boiling the quantity  $Q/hA$  must be less than 114°F. Employing hot channel factors and solving for heat transfer coefficient yields a maximum required value of  $h = 3750$  BTU/hr-ft<sup>2</sup>-°F. Were hot channel factors not employed, the required value of "h" would have been 1870 BTU/hr-ft<sup>2</sup>-°F. From the experimental results of Chapter 5 at a flow rate of 2000 gpm, "h" is



calculated to be 2430 BTU/hr-ft<sup>2</sup>-°F for a smooth channel, 3880 BTU/hr-ft<sup>2</sup>-°F for a longitudinally finned channel (fins 40 mils apart), and 5300 BTU/hr-ft<sup>2</sup>-°F for a transverse finned channel. Repeating in tabular form:

$h_{\text{required}}$ (with hot channel factors)	3750
$h_{\text{required}}$ (without hot channel factors)	1870
$h_{\text{smooth channel}}$	2430
$h_{\text{longitudinal fins}}$ (spaced 40 mils apart)	3880
$h_{\text{longitudinal fins}}$ (spaced 20 mils apart)	4660
$h_{\text{transverse fins}}$ (requires booster pump)	5300

It is apparent that if hot channel factors are not employed even the smooth channel is capable of providing adequate heat removal. The ratio

$$\frac{h_{\text{smooth channel}}}{h_{\text{required without H.C.F.}}} = 1.3.$$

However, a safety factor of 1.3 is not considered adequate due to the uncertainties involved in this "first-of-a-kind" design.

On the basis of the above analysis, it is recommended that longitudinal fins be milled into the fuel plates of the High Flux MITR. The fins should be 20 mils in height, 40 mils in width, and should be spaced 20 mils apart. Should milling difficulty require that the fin spacing be increased, the spacing may be increased up to but not beyond 40 mils.



## REFERENCES

1. Papay, L., "Coolant Void Reactivity Effects in Heavy Water Moderated, Low Enriched Uranium Rod Clusters", MIT Department of Nuclear Engineering, PhD Thesis, October 1968.
2. MITR Staff, "Operating Manual for the MIT Reactor", 1965.
3. Goebel, D.M., "Design of a High Flux Core for the MITR", MIT Course 22.90 Report, August 1965.
4. Thompson, T.J., Private Communication.
5. Kennedy, D.J., Private Communication.
6. Atomic Energy Commission, Regulation 10 CFR Part 20, January 1961.
7. Gage, A.M., "Design of the Shield for the Omega West Reactor", LASL Group P-2 Report, February 1, 1957.
8. Thompson, T.J., et al, "Final Hazards Summary Report to the Advisory Committee on Reactor Safeguards on a Research Reactor for the Massachusetts Institute of Technology", MIT-5007, January 1956.
9. Etherington, H., ed., Nuclear Engineering Handbook, McGraw-Hill Book Co., 1958.
10. Mittelman, P.S. and R.A. Liedtke, "Gamma Rays from Thermal Neutron Capture", Nucleonics, Vol. 13, p. 50, May 1955.
11. Goldstein, H., Fundamental Aspects of Reactor Shielding, Addison-Wesley Publishing Co., Inc., Reading, Mass., 1959.
12. Rockwell, T., ed., Reactor Shielding Design Manual, D. VanNostrand Company, Inc., Princeton, New Jersey, 1956.
13. Moteff, J., "Energy Spectrum of Gammas from Gross Fission Products", Nucleonics, Vol. 13, p. 28, May 1955.
14. Burrus, W.R., "How Channeling Between Chunks Raises Neutron Transmission Through Boral", Nucleonics, Vol. 16, p. 91, January 1958.



15. Glasstone, S. and M.C. Edlund, The Elements of Nuclear Reactor Theory, D. VanNostrand Company, Inc., Princeton, New Jersey, 1952.
16. Barnett, E., Private Communication.
17. Addae, A., Private Communication.
18. MITR Staff, "Technical Specifications for the MIT Research Reactor", MITNE-62, August 1965.
19. Wolak, F.A., "Heat Dissipation in the MIT Reactor", MIT Department of Nuclear Engineering, SM Thesis, June 1958.
20. DeVoto, W.R., "Process System Requirements of the MIT Reactor at Five Megawatts", MIT Department of Nuclear Engineering, Nuclear Engineers Thesis, MITNE-23, August 1962.
21. Hendrie, J.M., "Final Safety Analysis Report on the Brookhaven High Flux Beam Research Reactor", Brookhaven National Laboratory, Upton, New York, April 1964.
22. Gamble, W.E. and R.D. Bundy, "HFIR Heat Transfer Studies of Turbulent Water Flow in Thin Rectangular Channels", ORNL-3079, June 1961.
23. Marto, P.J., "Measurement of Surface Temperatures of an Irradiated MITR Fuel Element During Steady State and Transient Operating Conditions", MIT Course 22.42 Project Report, June 1962.
24. Rohsenow, W.M. and H. Choi, Heat, Mass and Momentum Transfer, Prentice-Hall, Inc., Englewood Cliffs, New Jersey, 1961.
25. Tong, L.S., Boiling Heat Transfer and Two-Phase Flow, John Wiley and Sons, Inc., New York, June 1967.
26. ANL-5800, Reactor Physics Constants, Argonne National Laboratory, July 1963.
27. Bergles, A.E., "Survey and Evaluation of Techniques to Augment Convective Heat and Mass Transfer", Department of Mechanical Engineering, MIT.







28. Brouillette, E.C., T.R. Mifflin and J.E. Myers, "Heat Transfer and Pressure-Drop Characteristics of Internal Finned Tubes", ASME Paper Number 57-A-47, December 1957.
29. Nunner, W., "Heat Transfer and Pressure Drop in Rough Tubes", AERE Lib/Trans 786, 1958.
30. Cope, W.F., "The Friction and Heat Transmission Coefficients of Rough Pipes", Proc. Instn. Mech. Engrs. 145, 99-105, 1941.
31. Sams, E.W., "Experimental Investigation of Average Heat-Transfer and Friction Coefficients for Air Flowing in Circular Tubes Having Square-Thread-Type Roughness", NACA RME52D17, 1952.
32. Kolar, V., "Heat Transfer in Turbulent Flow of Fluids Through Smooth and Rough Tubes", Int. J. Heat Mass Transfer 8, 639-653, 1965.
33. Lancet, R.T., "The Effects of Surface Roughness on the Convection Heat-Transfer Coefficient for Fully Developed Turbulent Flow in Ducts with Uniform Heat Flux", J. Heat Transfer, 168-174, 1959.
34. Boelter, L.M.K., G. Young, M.L. Greenfield, V.D. Sanders and M. Morgan, "An Investigation of Aircraft Heaters XXXVI-Experimental Determination of Thermal and Hydrodynamical Behavior of Air Flowing Along a Flat Plate Containing Turbulence Promoters", NACA-TN-2517, 1951.
35. Synan, J.W., Course 2.55 Term Paper Report, January 1969.
36. Frech, D., Private Communication.



## Appendix A

## EXPERIMENTAL DATA

In the experimental data which follows, the run numbers beginning with "A" are the smooth channel runs, run numbers beginning with "B" are the initial transverse finned channel runs, and run numbers beginning with "C" are the transverse finned channel runs after the channel was inverted. Average  $Re$  and average  $Nu/Pr^{0.3}$  values are an average of calculations based on centerline thermocouple readings only for the finned channel runs.



## Data Sheet 1

Run no. A-1

Flow Rate = 1.66 gpm

Electrical Power = 43,900 BTU/hr

 $Q/A = 52,800 \text{ BTU/hr-ft}^2$ 

Inlet Pressure = 6.1 psi

 $\Delta P = 1.5 \text{ psi}$ 

Exit Pressure = 4.6 psi

Inlet Temperature =  $98^\circ\text{F}$ Exit Temperature =  $151.5^\circ\text{F}$ 

Thermo-couple	$T_{wo}$	$T_{wi}$	$T_b$	$T_f$	h	Re	$Nu/Pr^{0.3}$
2	201	197	145	172	1010	8430	27.9
2R	193	189	145	167	1200	8150	32.6
3	192	188	138	163	1050	7920	28.5
4	190	186	131	159	960	7760	25.8
4R	186	182	131	157	1030	7590	27.6
5	173	169	125	147	1200	7642	31.5
5R	166	162	125	144	1420	6920	37.3
6	170	166	125	146	1285	6950	33.6
7	174	170	125	148	1170	7760	30.6
7R	169	165	125	145	1320	6930	34.5
8	165	161	118	139	1240	6650	32.1
8R	168	164	118	141	1145	6660	29.8
9	177	173	111	142	860	6680	22.3
10	157	152	105	129	1120	6145	28.5
10R	166	162	105	134	920	6390	23.7

Average Re = 7230

Average  $Nu/Pr^{0.3} = 29.7$



## Data Sheet 2

Run no. A-2

Flow Rate = 2.5 gpm

Electrical Power = 60,460 BTU/hr

 $Q/A = 72,550 \text{ BTU/hr-ft}^2$ 

Inlet Pressure = 9.0 psi

 $\Delta P = 2 \text{ psi}$ 

Exit Pressure = 7.0 psi

Inlet Temperature =  $91^\circ\text{F}$ Exit Temperature =  $139.5^\circ\text{F}$ 

Thermo-couple	$T_{wo}$	$T_{wi}$	$T_b$	$T_f$	h	Re	$Nu/Pr^{0.3}$
2	189	183	134	158	1475	11400	39.4
2R	176	170	134	152	2010	11000	53.2
3	179	173	128	150	1620	10900	42.8
4	186	180	122	150	1240	10900	32.8
4R	176	170	122	146	1510	10600	39.4
5	171	165	115	140	1470	10050	37.9
5R	166	160	115	138	1630	9820	41.9
6	171	165	115	140	1480	10050	38.2
7	169	163	115	140	1520	10000	39.4
7R	175	169	115	142	1345	10200	34.7
8	160	154	109	132	1640	9400	41.8
8R	164	158	109	134	1490	9400	38.1
9	161	155	103	129	1400	9300	35.4
10	153	147	97	122	1465	8650	37.8
10R	163	157	97	127	1210	9050	30.6

Average Re = 10,050

Average  $Nu/Pr^{0.3} = 38.9$





## Data Sheet 3

Run no. A-3

Flow Rate = 3.4 gpm

Electrical Power = 53,860 BTU/hr

 $Q/A = 64,630 \text{ BTU/hr-ft}^2$ 

Inlet Pressure = 15.2 psi

 $\Delta P = 1.7 \text{ psi}$ 

Exit Pressure = 13.5 psi

Inlet Temperature =  $101^\circ\text{F}$ Exit Temperature =  $133^\circ\text{F}$ 

Thermo- couple	$T_{wo}$	$T_{wi}$	$T_b$	$T_f$	h	Re	$Nu/Pr^{0.3}$
2	165	159	129	144	2170	14700	56.3
2R	161	156	129	143	2460	13650	64.0
3	157	152	125	139	2430	13200	62.5
4	158	153	121	137	2060	13200	53.1
4R	156	151	121	136	2200	13000	58.4
5	149	144	117	130	2450	13200	62.2
5R	151	145	117	131	2300	12540	58.8
6	150	144	117	131	2400	13200	61.0
7	145	140	117	128	2940	12500	74.7
7R	161	156	117	137	1670	13200	43.1
8	142	137	113	125	2740	11800	69.0
8R	154	148	113	131	1840	12500	46.6
9	141	136	109	123	2410	11670	60.5
10	135	130	105	117	2620	11100	65.1
10R	148	143	105	124	1705	11760	43.0

Average Re = 12,740

Average  $Nu/Pr^{0.3} = 58.6$



Run no. A-4

Flow Rate = 3.5 gpm

Electrical Power = 73,090 BTU/hr

 $Q/A = 87,770 \text{ BTU/hr-ft}^2$ 

Inlet Pressure = 14 psi

 $\Delta P = 2.4 \text{ psi}$ 

Exit Pressure = 11.6 psi

Inlet Temperature = 91°F

Exit Temperature = 133.5°F

Thermo-couple	$T_{wo}$	$T_{wi}$	$T_b$	$T_f$	h	Re	$Nu/Pr^{0.3}$
2	170	163	128	146	2510	15700	65.5
2R	165	158	128	143	2920	14400	76.0
3	162	155	123	139	2740	14000	71.4
4	163	156	118	137	2320	13600	60.6
4R	159	151	118	139	2700	13970	70.3
5	153	146	112	129	2580	12850	65.5
5R	154	147	112	130	2510	12900	63.6
6	154	147	112	130	2510	12900	63.6
7	156	149	112	131	2370	12900	60.6
7R	162	155	112	134	2040	13250	52.3
8	148	141	107	124	2580	12300	65.0
8R	157	150	107	129	2040	12850	51.8
9	146	139	102	121	2370	11800	59.2
10	143	136	96	116	2190	11340	54.4
10R	152	145	96	121	1790	11800	44.7

Average Re = 13,100

Average  $Nu/Pr^{0.3} = 61.6$



## Data Sheet 5

Run no, A-5

Flow Rate = 4.0 gpm

Electrical Power = 62,530 BTU/hr

 $Q/A = 75,040 \text{ BTU/hr-ft}^2$ 

Inlet Pressure = 16.7 psi

 $\Delta P = 3.0 \text{ psi}$ 

Exit Pressure = 13.7 psi

Inlet Temperature =  $100^\circ\text{F}$ Exit Temperature =  $131.5^\circ\text{F}$ 

Thermo-couple	$T_{wo}$	$T_{wi}$	$T_b$	$T_f$	h	Re	$Nu/Pr^{0.3}$
2	166	160	128	144	2345	16640	61.3
2R	162	156	128	142	2680	16360	69.7
3	160	154	124	139	2500	16080	64.7
4	159	153	120	137	2270	15700	58.6
4R	155	149	120	135	2590	15460	66.3
5	150	144	116	130	2680	14870	68.1
5R	151	145	116	131	2590	14870	65.7
6	150	144	116	130	2730	14870	69.3
7	150	144	116	130	2730	14870	69.3
7R	159	153	116	135	2030	15460	52.0
8	146	140	112	126	2680	14530	67.4
8R	153	147	112	130	2140	14870	54.5
9	146	140	108	124	2345	14020	58.7
10	142	136	104	120	2340	13620	58.5
10R	150	144	104	124	1900	14020	47.9

Average Re = 15,080

Average  $Nu/Pr^{0.3} = 62.1$



## Data Sheet 6

Run no: A-6

Flow Rate = 4.2 gpm

Electrical Power = 55,500 BTU/hr

 $Q/A = 66,590 \text{ BTU/hr-ft}^2$ 

Inlet Pressure = 15.8 psi

 $\Delta P = 1.8 \text{ psi}$ 

Exit Pressure = 14 psi

Inlet Temperature = 119°F

Exit Temperature = 146°F

Thermo-couple	$T_{wo}$	$T_{wi}$	$T_b$	$T_f$	h	Re	$Nu/Pr^{0.3}$
2	177	172	143	157	2230	20500	59.8
2R	168	163	143	152	3300	19700	87.1
3	172	167	139	153	2390	19750	63.1
4	172	167	136	151	2130	19600	56.4
4R	163	158	136	147	3010	19000	78.8
5	165	160	133	146	2480	19200	64.8
5R	157	153	133	142	3310	18300	86.2
6	165	160	133	146	2480	19200	64.8
7	165	160	133	146	2480	19200	64.8
7R	169	164	133	148	2160	19000	56.3
8	165	160	129	144	2210	19400	57.7
8R	163	158	129	143	2360	18300	61.4
9	162	157	126	141	2180	18200	56.3
10	156	151	123	136	2350	17600	60.5
10R	154	149	123	136	2490	17850	63.9

Average Re = 18,990

Average  $Nu/Pr^{0.3} = 65.5$





## Data Sheet 7

Run no. A-7

Flow Rate = 4.95 gpm

Electrical Power = 86,460 BTU/hr

 $Q/A = 103,750 \text{ BTU/hr-ft}^2$ 

Inlet Pressure = 23.2 psi

 $\Delta P = 3.7 \text{ psi}$ 

Exit Pressure = 19.5 psi

Inlet Temperature =  $103^\circ\text{F}$ Exit Temperature =  $138.5^\circ\text{F}$ 

Thermo- couple	$T_{wo}$	$T_{wi}$	$T_b$	$T_f$	h	Re	$Nu/Pr^{0.3}$
2	180	171	134	153	2780	22050	74.0
2R	176	168	134	151	3110	21600	82.2
3	173	164	130	147	2990	21050	78.7
4	173	164	125	145	2650	20700	69.2
4R	168	160	125	142	3030	19900	78.7
5	161	152	121	136	3340	19300	86.0
5R	173	164	121	142	2410	19900	62.6
6	163	155	121	138	3060	19450	79.4
7	162	153	121	138	3230	19400	83.2
7R	173	164	121	142	2410	19900	62.6
8	160	152	116	134	3000	19000	75.9
8R	169	160	116	138	2390	19500	61.8
9	160	152	112	132	2630	18400	67.1
10	151	143	108	125	2960	17800	74.9
10R	159	150	108	129	2420	18350	62.1

Average Re = 19,750

Average  $Nu/Pr^{0.3} = 73.2$



## Data Sheet 8

Run no, B-1

Flow Rate = 1.38 gpm

Electrical Power = 34,800 BTU/hr

 $Q/A = 41,800 \text{ BTU/hr-ft}^2$ 

Inlet Pressure = 9.5 psi

 $\Delta P = 5 \text{ psi}$ 

Exit Pressure = 4.5 psi

Inlet Temperature =  $101^{\circ}\text{F}$ Exit Temperature =  $152^{\circ}\text{F}$ 

Thermo-couple	$T_{wo}$	$T_{wi}$	$T_b$	$T_f$	$h$	Re	$Nu/Pr^{0.3}$
2	181	178	146	162	1300	6650	35.1
2R	175	172	146	159	1595	6500	42.8
3	169	166	139	153	1570	6190	41.7
4	158	155	133	144	1940	5760	50.8
4R	157	154	133	143	2020	5710	52.6
5	139	135	127	131	4920	5170	125.4
5R	137	134	127	130	5970	5140	152.0
6	148	145	127	136	2300	5400	59.1
7	142	139	127	133	3480	5290	89.2
7R	138	134	127	130	5430	5140	138.2
8	143	139	120	130	2200	5140	56.0
9	136	133	114	123	2235	4820	56.1
10	126	123	107	115	2770	4490	68.5
10R	127	124	107	116	2560	4530	63.6

Average Re = 5,520

Average  $Nu/Pr^{0.3} = 52.6$



## Data Sheet 9

Run no. B-2

Flow Rate = 2.0 gpm

Electrical Power = 48,400 BTU/hr

 $Q/A = 58,100 \text{ BTU/hr-ft}^2$ 

Inlet Pressure = 13.8 psi

 $\Delta P = 7.3 \text{ psi}$ 

Exit Pressure = 6.5 psi

Inlet Temperature =  $94.5^\circ\text{F}$ Exit Temperature =  $143^\circ\text{F}$ 

Thermo-couple	$T_{wo}$	$T_{wi}$	$T_b$	$T_f$	h	Re	$Nu/Pr^{0.3}$
2	176	171	137	154	1720	9140	45.6
2R	173	168	137	152	1900	8980	50.3
3	165	160	131	145	2040	8520	53.4
4	152	147	125	136	2620	7900	67.3
4R	153	148	125	137	2470	8000	63.8
5	133	128	119	123	6455	7050	162
5R	133	128	119	123	6455	7050	162
6	146	141	119	134	2665	7800	68.4
7	137	132	119	125	4305	7200	108
7R	134	129	119	124	5480	7140	138
8	138	133	113	123	2890	7060	72.5
9	130	125	107	116	3160	6630	78.3
10	120	115	101	108	4010	6100	97.5
10R	124	119	101	110	3230	6250	79.2

Average Re = 7,640

Average  $Nu/Pr^{0.3} = 67.6$



Run no: B-3

Flow Rate = 2.6 gpm

Electrical Power = 80,000 BTU/hr

 $Q/A = 96,100 \text{ BTU/hr-ft}^2$ 

Inlet Pressure = 19.5 psi

 $\Delta P = 10.5 \text{ psi}$ 

Exit Pressure = 9 psi

Inlet Temperature =  $95^\circ\text{F}$ Exit Temperature =  $157^\circ\text{F}$ 

Thermo-couple	$T_{wo}$	$T_{wi}$	$T_b$	$T_f$	h	Re	$Nu/Pr^{0.3}$
2	197	189	149	169	2440	12900	66.6
2R	194	186	149	163	2590	12350	70.7
3	185	177	142	159	2690	12000	72.3
4	171	163	134	149	3260	11100	85.8
4R	171	163	134	149	3260	11100	85.8
5	146	138	126	132	7810	9650	200
5R	148	140	126	133	7120	9780	182
6	158	150	126	138	4055	10150	105
7	152	144	126	135	5340	9930	137
7R	148	140	126	133	6720	9780	172
8	153	145	118	132	3560	9650	90.9
9	143	135	111	123	3990	8900	100
10	130	122	103	112	5005	8050	123
10R	135	127	103	115	4020	8280	99.5

Average Re = 10,440

Average  $Nu/Pr^{0.3} = 90.0$





## Data Sheet 11

Flow no. B-4

Flow Rate = 3.0 gpm

Electrical Power = 79,500 BTU/hr

 $Q/A = 95,400 \text{ BTU/hr-ft}^2$ 

Inlet Pressure = 25 psi

 $\Delta P = 13.2 \text{ psi}$ 

Exit Pressure = 11.8 psi

Inlet Temperature =  $99^{\circ}\text{F}$ Exit Temperature =  $152^{\circ}\text{F}$ 

Thermo- couple	$T_{wo}$	$T_{wi}$	$T_b$	$T_f$	h	Re	$Nu/Pr^{0.3}$
2	191	183	145	169	2540	15300	69.2
2R	185	177	145	161	3020	14350	81.3
3	179	171	139	155	2940	13800	78.4
4	167	159	132	146	3530	12850	93.7
4R	165	157	132	145	3820	12700	99.8
5	146	138	126	132	7630	11450	195
5R	144	136	126	131	9090	11300	232
6	157	149	126	137	4150	11950	107
7	150	142	126	134	5780	11650	148
7R	147	139	126	132	7070	11450	181
8	151	143	119	131	3980	11300	101
9	143	135	112	123	4260	10550	107
10	133	125	106	115	5000	9800	124
10R	134	126	106	116	4680	9900	116

Average Re = 12,250

Average  $Nu/Pr^{0.3} = 97.7$



Run no. B-5

Flow Rate = 3.5 gpm

Electrical Power = 80,000 BTU/hr

$Q/A = 96,100 \text{ BTU/hr-ft}^2$

Inlet Pressure = 32 psi

$\Delta P = 17.2 \text{ psi}$

Exit Pressure = 14.8 psi

Inlet Temperature =  $94.5^\circ\text{F}$

Exit Temperature =  $140.5^\circ\text{F}$

Thermo-couple	$T_{wo}$	$T_{wi}$	$T_b$	$T_f$	h	Re	$\text{Nu}/\text{Pr}^{0.3}$
2	177	169	135	152	2870	15650	75.9
2R	173	165	135	150	3200	15400	84.6
3	167	159	129	144	3170	14700	83.0
4	156	149	123	136	3770	13750	97.1
4R	157	149	123	136	3700	13750	95.2
5	139	131	118	124	7120	12450	179
5R	140	132	118	125	6720	12500	169
6	150	142	118	130	3920	13100	99.9
7	142	134	118	126	5820	12600	147
7R	140	132	118	125	6630	12500	167
8	143	135	112	124	4110	12450	103
9	135	127	106	117	4580	11650	114
10	126	118	100	109	5490	10800	134
10R	130	122	100	111	4410	10950	118

Average Re = 13,220

Average  $\text{Nu}/\text{Pr}^{0.3} = 100.4$



## Data Sheet 13

Run no, B-6

Flow Rate = 3.9 gpm

Electrical Power = 79,400 BTU/hr

 $Q/A = 95,300 \text{ BTU/hr-ft}^2$ 

Inlet Pressure = 38.5 psi

 $\Delta P = 21 \text{ psi}$ 

Exit Pressure = 17.5 psi

Inlet Temperature = 101°F

Exit Temperature = 141°F

Thermo-couple	$T_{wo}$	$T_{wi}$	$T_b$	$T_f$	$h$	$Re$	$Nu/Pr^{0.3}$
2	179	171	136	153	2760	17350	73.3
2R	171	163	136	149	3600	16900	94.7
3	168	160	131	145	3310	16350	86.6
4	156	148	126	137	4330	15350	112
4R	156	148	126	137	4410	15350	114
5	140	132	121	127	8360	14100	212
5R	140	132	121	126	8910	13900	223
6	150	142	121	132	4540	14700	116
7	132	135	121	128	6810	14200	173
7R	141	133	121	127	8080	14100	204
8	145	137	116	127	4540	14100	115
9	139	131	111	121	4890	13300	122
10	129	121	106	114	6230	12500	154
10R	133	125	106	116	5020	12700	124

Average  $Re = 14,860$ Average  $Nu/Pr^{0.3} = 111.1$



Run no. B-7

Flow Rate = 4.3 gpm

Electrical Power = 80,000 BTU/hr

$Q/A = 96,200 \text{ BTU/hr-ft}^2$

Inlet Pressure = 44 psi

$\Delta P = 24 \text{ psi}$

Exit Pressure = 20 psi

Inlet Temperature =  $97.5^\circ\text{F}$

Exit Temperature =  $135^\circ\text{F}$

Thermo-couple	$T_{wo}$	$T_{wi}$	$T_b$	$T_f$	$h$	Re	$Nu/Pr^{0.3}$
2	163	155	130	142	3850	17600	100
2R	160	152	130	141	4370	17500	114
3	159	151	126	138	3850	17100	99.4
4	150	142	121	131	4510	16100	115
4R	149	141	121	131	4810	16100	123
5	137	129	116	122	7580	14850	190
5R	137	129	116	123	7400	15000	185
6	145	137	116	126	4740	15400	120
7	139	131	116	123	6420	14950	161
7R	137	129	114	123	7570	14950	190
8	140	132	112	122	4690	14850	118
9	134	126	107	116	5200	14100	129
10	126	118	102	110	6000	13250	147

Average Re = 15,780

Average  $Nu/Pr^{0.3} = 118.2$





Run no. C-1

Flow Rate = 1.5 gpm

Electrical Power = 77,500 BTU/hr

 $Q/A = 93,100 \text{ BTU/hr-ft}^2$ 

Inlet Pressure = 9.7 psi

 $\Delta P = 5.2 \text{ psi}$ 

Exit Pressure = 4.5 psi

Inlet Temperature =  $97^\circ\text{F}$ Exit Temperature =  $199^\circ\text{F}$ 

Thermo-couple	$T_{wo}$	$T_{wi}$	$T_b$	$T_f$	h	Re	$Nu/Pr^{0.3}$
2	250	242	186	214	1660	10100	44.8
2R	252	244	186	215	1605	10100	43.4
3	235	227	174	200	1760	9330	47.5
4	212	204	161	183	2160	8400	58.4
5	178	170	148	159	4230	7050	114
5R	170	162	148	155	6650	6800	179
6	190	182	148	165	2740	7400	74.0
7	170	162	148	155	6650	6800	179
7R	172	164	148	156	5800	6900	156
8	182	174	135	155	2390	6800	64.6
8R	178	170	135	153	2660	6700	71.8
9	169	161	123	142	2450	6150	66.2
10	148	140	110	125	3150	5330	85.0
10R	152	144	110	127	2780	5430	75.0

Average Re = 7570

Average  $Nu/Pr^{0.3} = 63.1$



Run no. C-2

Flow Rate = 2.0 gpm

Electrical Power = 78,900 BTU/hr

 $Q/A = 94,800 \text{ BTU/hr-ft}^2$ 

Inlet Pressure = 13.8 psi

 $\Delta P = 7.3 \text{ psi}$ 

Exit Pressure = 6.5 psi

Inlet Temperature =  $98^\circ\text{F}$ Exit Temperature =  $176^\circ\text{F}$ 

Thermo-couple	$T_{wo}$	$T_{wi}$	$T_b$	$T_f$	h	Re	$Nu/Pr^{0.3}$
2	220	212	166	189	2060	11600	54.5
2R	220	212	166	189	2060	11600	54.5
3	208	200	157	178	2180	10800	57.8
4	192	184	147	165	2600	9860	68.9
5	164	156	137	147	4990	8540	130
5R	158	150	137	144	7300	8350	193
6	176	168	137	153	3050	8950	80.8
7	158	150	137	144	7300	8350	193
7R	160	152	137	145	6300	8400	167
8	169	161	127	144	2790	8350	73.9
8R	165	157	127	142	3160	8230	83.7
9	159	151	118	134	2830	7700	75.0
10	142	134	108	121	3710	6850	98.3
10R	146	138	108	123	3160	6970	83.7

Average Re = 9090

Average  $Nu/Pr^{0.3} = 73.1$



## Data Sheet 17

Run no. C-3

Flow Rate = 2.5 gpm

Electrical Power = 78,900 BTU/hr

 $Q/A = 94,800 \text{ BTU/hr-ft}^2$ 

Inlet Pressure = 19 psi

 $\Delta P = 10 \text{ psi}$ 

Exit Pressure = 9 psi

Inlet Temperature =  $98^\circ\text{F}$ Exit Temperature =  $161^\circ\text{F}$ 

Thermo-couple	$T_{wo}$	$T_{wi}$	$T_b$	$T_f$	h	Re	$Nu/Pr^{0.3}$
2	197	189	153	171	2630	12800	68.4
2R	198	190	153	171	2560	12800	66.6
3	188	180	145	163	2710	12100	70.5
4	174	166	137	152	3270	11100	85.0
5	155	147	130	138	5410	9960	141
5R	151	143	130	136	7020	9750	183
6	166	158	130	144	3390	10400	88.1
7	151	143	130	136	7020	9750	183
7R	152	143	130	137	6530	9850	170
8	160	152	122	137	3160	9850	82.1
8R	157	149	122	136	3510	9750	91.2
9	151	143	114	129	3270	9200	85.0
10	137	129	106	118	4120	8330	107
10R	141	133	106	120	3510	8500	92.1

Average Re = 10,480

Average  $Nu/Pr^{0.3} = 83.6$



## Data Sheet 18

Fun no. C-4

Flow Rate = 3.0 gpm

Electrical Power = 78,900 BTU/hr

 $Q/A = 94,800 \text{ BTU/hr-ft}^2$ 

Inlet Pressure = 25 psi

 $\Delta P = 13.2 \text{ psi}$ 

Exit Pressure = 11.8 psi

Thermo- couple	$T_{wo}$	$T_{wi}$	$T_b$	$T_f$	h	Re	$Nu/Pr^{0.3}$
2	183	175	143	159	2960	14100	75.5
2R	183	175	143	159	2960	14100	75.5
3	173	165	137	151	3380	13200	86.2
4	165	157	130	144	3510	12500	89.5
5	147	139	124	131	6110	11200	156
5R	144	136	124	130	7580	11100	193
6	156	148	124	136	3870	11700	98.6
7	144	136	124	130	7580	11100	193
7R	144	136	124	130	7580	11100	193
8	152	144	117	131	3510	11200	89.5
8R	149	141	117	129	3950	11050	101
9	145	137	110	124	3510	10600	89.5
10	133	125	104	115	4510	9700	115
10R	136	128	104	116	3950	9800	101

Average Re = 11,800

Average  $Nu/Pr^{0.3} = 92.1$





## Data Sheet 19

Run no. C-5

Flow Rate = 3.5 gpm

Electrical Power = 78,900 BTU/hr

 $Q/A = 94,800 \text{ BTU/hr-ft}^2$ 

Inlet Pressure = 32 psi

 $\Delta P = 17.2 \text{ psi}$ 

Exit Pressure = 14.8 psi

Inlet Temperature = 98°F

Exit Temperature = 142°F

Thermo-couple	$T_{wo}$	$T_{wi}$	$T_b$	$T_f$	$h$	Re	$Nu/Pr^{0.3}$
2	174	166	137	151	3260	15400	83.1
2R	174	166	137	151	3260	15400	83.1
3	166	158	131	145	3505	14700	89.4
4	157	149	126	137	4030	13850	103
5	145	137	120	129	5560	12900	142
5R	142	134	120	127	6760	12700	172
6	152	144	120	132	3950	13250	101
7	142	134	120	127	6760	12900	172
7R	141	133	120	127	7280	12900	185
8	148	140	114	127	3640	12900	92.8
8R	145	137	114	125	4120	12450	105
9	142	134	109	122	3790	12100	96.6
10	131	123	104	113	4850	11100	124
10R	134	126	104	115	4210	11350	107

Average Re = 13,250

Average  $Nu/Pr^{0.3} = 98.4$



## Data Sheet 20

Run no. C-6

Flow Rate = 3.5 gpm

Electrical Power = 137,300 BTU/hr

 $Q/A = 165,000 \text{ BTU/hr-ft}^2$ 

Inlet Pressure = 32 psi

 $\Delta P = 17.2 \text{ psi}$ 

Exit Pressure = 14.8 psi

Inlet Temperature = 93°F

Exit Temperature = 170°F

Thermo-couple	$T_{wo}$	$T_{wi}$	$T_b$	$T_f$	h	Re	$Nu/Pr^{0.3}$
2	219	205	160	183	3670	19600	96.5
2R	218	204	160	182	3750	19500	98.5
3	205	191	151	171	4130	17950	109
4	195	181	141	161	4130	16700	109
5	168	154	132	143	7340	14450	193
5R	163	149	132	140	9430	14150	248
6	179	165	132	148	4920	13750	130
7	164	150	132	141	8930	14250	235
7R	163	149	132	140	9440	14150	248
8	174	160	122	141	4350	14250	115
8R	170	156	122	139	4860	14000	128
9	164	150	112	131	4350	13100	115
10	148	134	103	119	5330	11750	140
10R	151	137	103	120	4860	11900	128

Average Re = 15,250

Average  $Nu/Pr^{0.3} = 116.7$



## Data Sheet 21

Run no. C-7

Flow Rate = 3.5 gpm

Electrical Power = 35,450 BTU/hr

 $Q/A = 42,550 \text{ BTU/hr-ft}^2$ 

Inlet Pressure = 32 psi

 $\Delta P = 17.2 \text{ psi}$ 

Exit Pressure = 14.8 psi

Inlet Temperature =  $95^\circ\text{F}$ Exit Temperature =  $115.5^\circ\text{F}$ 

Thermo-couple	$T_{wo}$	$T_{wi}$	$T_b$	$T_f$	h	Re	$Nu/Pr^{0.3}$
2	134	131	113	122	2430	12100	59.5
2R	134	131	113	122	2430	12100	59.5
3	130	127	110	118	2640	11600	64.8
4	125	122	108	114	3110	11250	76.1
5	121	118	105	111	3490	10900	85.4
5R	119	116	105	110	4170	10800	102
6	125	122	105	113	2630	11100	64.3
7	119	116	105	110	4170	10800	102
7R	118	115	105	110	4620	10800	113
8	123	120	103	111	2550	10900	62.4
8R	119	116	103	109	3350	10700	82.0
9	118	115	100	107	2955	10500	72.4
10	113	110	98	104	3580	10200	87.5
10R	115	112	98	105	3060	10300	75.0

Average Re = 11,075

Average  $Nu/Pr^{0.3} = 70.4$



Run no. C-8

Flow Rate = 4.0 gpm

Electrical Power = 78,900 BTU/hr

 $Q/A = 94,800 \text{ BTU/hr-ft}^2$ 

Inlet Pressure = 39.5 psi

 $\Delta P = 21.5 \text{ psi}$ 

Exit Pressure = 18 psi

Inlet Temperature =  $98^\circ\text{F}$ Exit Temperature =  $137^\circ\text{F}$ 

Thermo- couple	$T_{wo}$	$T_{wi}$	$T_b$	$T_f$	h	Re	$Nu/Pr^{0.3}$
2	165.5	157.5	132	145	3710	16800	93.5
2R	165.5	157.5	132	145	3710	16800	93.5
3	158	150	127	139	4120	16000	104
4	151.5	143.5	122.5	133	4500	15300	113
5	140	132	117.5	125	6530	14200	164
5R	138	130	117.5	124	7560	14100	190
6	146	138	117.5	128	4610	14550	116
7	138	130	117.5	124	7560	14100	190
7R	137	129	117.5	123	8220	13950	207
8	143.5	135.5	112.5	124	4110	14100	103.5
8R	141	133	112.5	123	4610	13950	116
9	138	130	107	119	4110	13450	103.5
10	129	121	103	112	5250	12550	132
10R	132	124	103	114	4510	12800	114

Average Re = 14,630

Average  $Nu/Pr^{0.3} = 108.9$





Run no. C-9

Flow Rate = 4.5 gpm

Electrical Power 78,900 BTU/hr

 $Q/A = 94,800 \text{ BTU/hr-ft}^2$ 

Inlet Pressure = 48.5 psi

 $\Delta P = 26.5 \text{ psi}$ 

Exit Pressure = 22 psi

Inlet Temperature = 97°F

Exit Temperature = 132°F

Thermo-couple	$T_{wo}$	$T_{wi}$	$T_b$	$T_f$	h	Re	$Nr/Pr^{0.3}$
2	161	153	128	141	3790	18300	94.7
2R	160	152	128	140	3950	18150	98.7
3	154	146	123	135	4120	17500	103
4	147	139	119	129	4730	16550	108
5	138	130	114.5	122	6110	15600	153
5R	135	127	114.5	121	7570	15400	189
6	144	136	114.5	125	4410	16000	110
7	136	128	114.5	121	7010	15400	175
7R	135	127	114.5	121	7560	15400	189
8	141	133	110	121	4120	15400	103
8R	137	129	110	120	4990	15300	125
9	136	128	106	117	4310	14800	108
10	127	119	101	110	5260	13900	131
10R	129.5	121.5	101	111	4610	14000	115

Average Re = 15,990

Average  $Nu/Pr^{0.3} = 109.6$



Table A-1

Average Heat Transfer Coefficient vs.

Thermocouple Position Along the Coolant Channel

Thermocouple position	2	2R	3	4	4R	6	8	8R	9	10	10R
h, "A" runs	2075	2524	2245	1947	2294	2276	2296	1915	2027	2148	1778
h, "B" runs	2497	2896	2796	3438	3502	3766	3708	-	4043	4928	3985
h, "C" runs	2867	2872	3111	3542	-	3717	3389	3857	3467	4407	3819



FIGURE A-1  
CONVERSION OF THERMOCOUPLE  
READINGS IN MILLIVOLTS TO °F

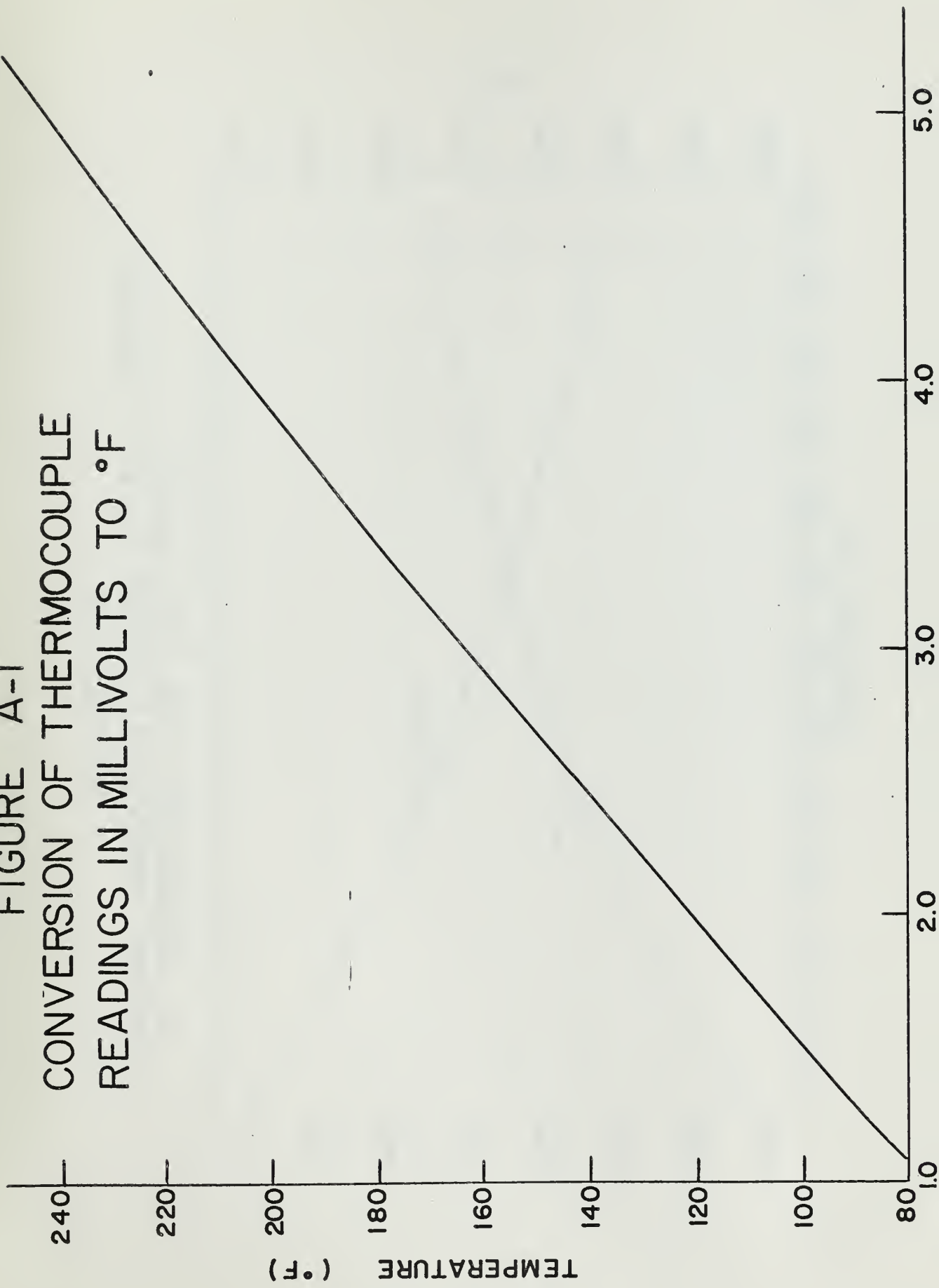
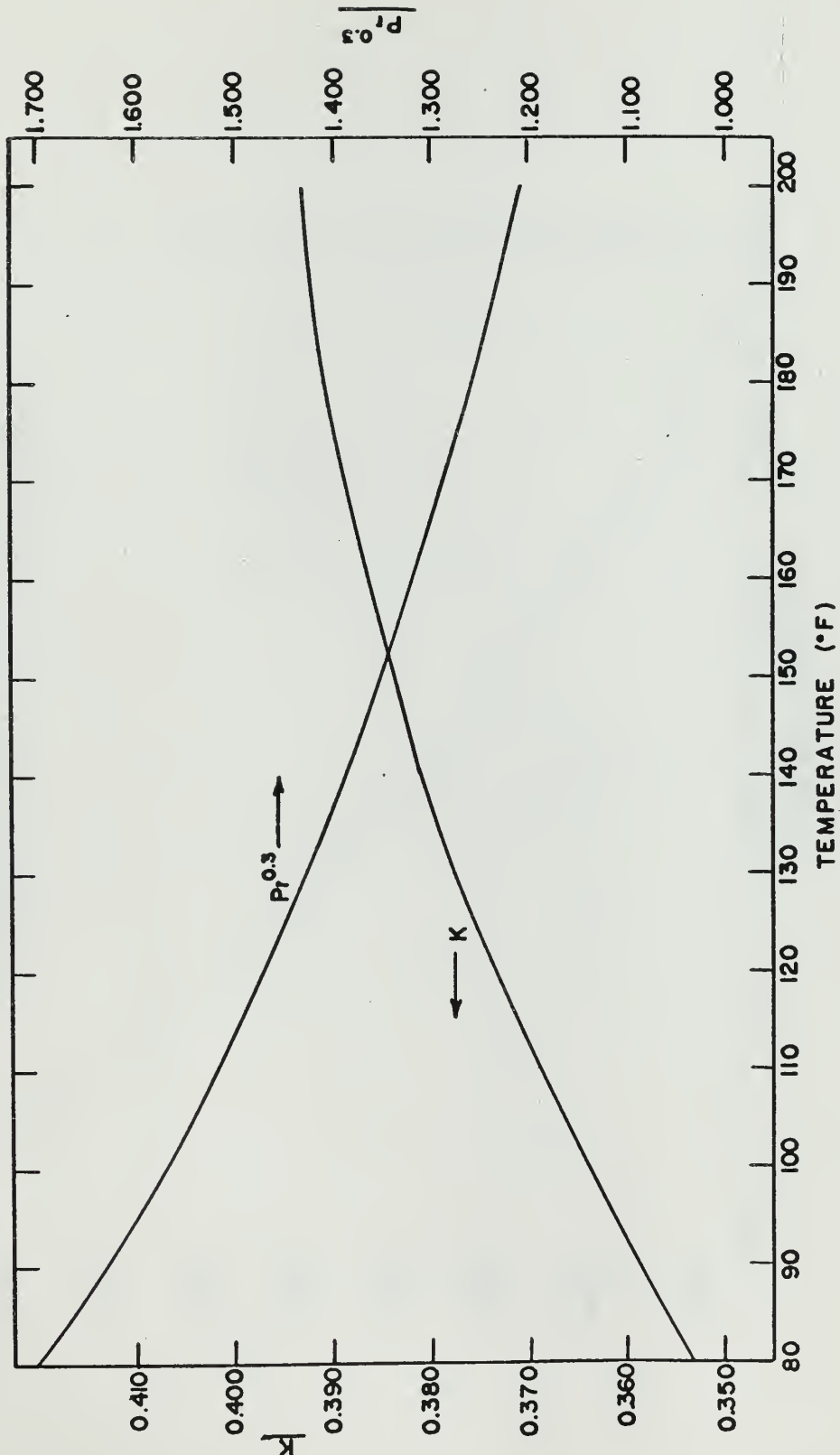


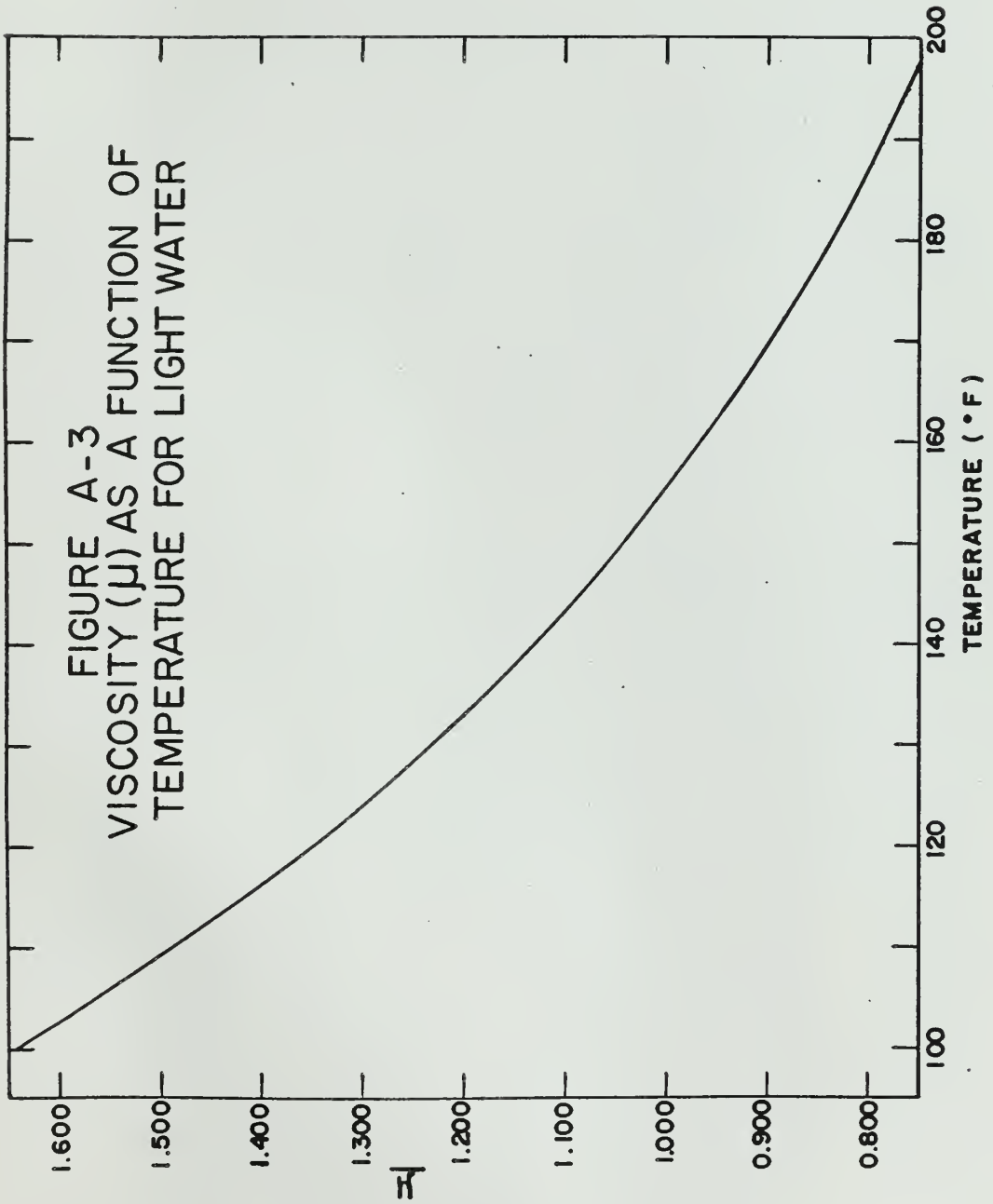


FIGURE A-2  
THERMAL CONDUCTIVITY (K) AND  $P_f^{0.3}$  AS A FUNCTION  
OF TEMPERATURE FOR LIGHT WATER







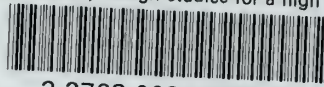






thesS6688

Preliminary design studies for a high fl



3 2768 002 01598 4

DUDLEY KNOX LIBRARY